Dissertation

Development, characterization and application of novel genetically encoded, fluorescent potassium ion indicators

submitted by

Helmut Bischof

MSc, BSc

for the Academic Degree of

Doctor of Philosophy

(PhD)

at the

Medical University of Graz

Gottfried Schatz Research Center for Cell Signaling, Metabolism and Aging

under the supervision of

Assoz. Prof. Priv.-Doz. Mag.pharm. Dr.rer.nat. Roland Malli

2019

Statutory Declaration

I hereby declare that this thesis is my own original work and that I have fully acknowledged by name all of those individuals and organizations that have contributed to the research for this thesis. Due acknowledgement has been made in the text to all other material used. Throughout this thesis and in all related publications I followed the “Standards of Good Scientific Practice and Ombuds Committee at the Medical University of Graz.

Place, Date

Sign

Disclosures

Part of this thesis has been published in Bischof, H., et al., “Novel genetically encoded fluorescent probes enable real-time detection of potassium *in vitro* and *in vivo*.” Nature Communications, 2017.

Co-authors who contributed to the thesis and the publication and agreed to the use of their data in the thesis:

From the Brigham and Women’s Hospital, Cardiovascular Division, Harvard Medical School, 75 Francis Street,Boston MA, 02115, USA

Eroglu, Emrah, PhD

From the Clinical Division of Nephrology, Medical University of Graz, Auenbruggerplatz 27, 8036, Graz, Austria

Artinger, Katharina, Dr. PhD; **Deak, Andras T., Dr. PhD**; **Eller, Kathrin, Prof. Dr.**; **Rosenkranz, Alexander R., Prof. Dr.**

From the Clinical Institute of Medical and Chemical Laboratory Diagnostics, Medical University of Graz, Auenbruggerplatz 27, 8036, Graz, Austria

Niedrist, Tobias, Dr.

From the Comprehensive Pneumology Center, Institute of Lung Biology and Disease (iLBD), Helmholtz Zentrum München, Max-Lebsche-Platz 31, 81377 Munich, Germany

Rehberg, Markus, Prof. Dr.

From the Gottfried Schatz Research Center, Chair of Biophysics, Medical University of Graz, Neue Stiftingtalstraße 6/4, 8010 Graz, Austria

Groschner, Klaus, Prof. Dr.; Lindermuth, Hanna, Mag.rer.nat.; Pelzmann Brigitte, Dr.; Prassl, Ruth, Prof. Dr.

From the Gottfried Schatz Research Center, Chair of Molecular Biology and Biochemistry, Medical University of Graz, Neue Stiftingtalstraße 6/6, 8010 Graz, Austria

Gottschalk, Benjamin, MSc; Graier, Wolfgang F., Prof. Dr.; Kratky, Dagmar, Prof. Dr.; Madl, Tobias, Prof. Dr.; Malli, Roland, Prof. Dr.; Nemanja Vujic, PhD; Sarah Stryeck, MSc; Waldeck-Weiermair, Markus, Dr.

From the Ludwig-Maximilian University (LMU), Institute for Stroke and Dementia Research (ISD), Klinikum der Universität München, Feodor-Lynen-Straße 17, 81377, Munich, Germany

Plesnila, Nikolaus, Prof. Dr.

During my PhD thesis I also contributed to the following publications

- *Burgstaller, S; Bischof, H; Gensch, T; Stryeck, S; Gottschalk, B; Ramadani-Muja, J; Eroglu, E; Rost, R; Balfanz, S; Baumann, A; Waldeck-Weiermair, M; Hay, JC; Madl, T; Graier, WF; Malli, R.* pH-Lemon, a fluorescent protein-based pH reporter for acidic compartments. ACS Sens. 2019

- *Depaoli, MR; Karsten, F; Madreiter-Sokolowski, CT; Klec, C; Gottschalk, B; Bischof, H; Eroglu, E; Waldeck-Weiermair, M; Simmen, T; Graier, WF; Malli, R*. Real-Time Imaging of Mitochondrial ATP Dynamics Reveals the Metabolic Setting of Single Cells. Cell Rep. 2018; 25(2):501-512

- *Eroglu, E; Bischof, H; Charoensin, S; Waldeck-Weiermaier, M; Graier, WF; Malli, R*. Real-Time Imaging of Nitric Oxide Signals in Individual Cells Using geNOps. Methods Mol Biol. 2018; 1747: 23-34.

- *Eroglu, E; Charoensin, S; Bischof, H; Ramadani, J; Gottschalk, B; Depaoli, MR; Waldeck-Weiermair, M; Graier, WF; Malli, R*. Genetic biosensors for imaging nitric oxide in single cells. Free Radic Biol Med. 2018.

- *Charoensin, S; Eroglu, E; Opelt, M; Bischof, H; Madreiter-Sokolowski, CT; Kirsch, A; Depaoli, MR; Frank, S; Schrammel, A; Mayer, B; Waldeck-Weiermair, M; Graier, WF; Malli, R.* Intact mitochondrial Ca^{2+} uniport is essential for agonist-induced activation of endothelial nitric oxide synthase (eNOS). Free Radic Biol Med. 2017; 102(1):248-259.

- *Eroglu, E; Hallström, S; Bischof, H; Opelt, M; Schmidt, K; Mayer, B; Waldeck-Weiermair, M; Graier, WF; Malli, R*. Real-time visualization of distinct nitric oxide generation of nitric oxide synthase isoforms in single cells. Nitric Oxide. 2017; 70(31):59-67.

- *Eroglu, E; Rost, R; Bischof, H; Blass, S; Schreilechner, A; Gottschalk, B; Depaoli, MR; Klec, C; Charoensin, S; Madreiter-Sokolowski, CT; Ramadani, J; Waldeck-Weiermair, M; Graier, WF; Malli, R*. Application of Genetically Encoded Fluorescent Nitric Oxide (NO•) Probes, the geNOps, for Real-time Imaging of NO• Signals in Single Cells. J Vis Exp. 2017; 5(121).

Foreword

The following pages of this thesis refer to the development of novel genetically encoded, fluorescent protein based potassium ion (K^+) sensors, the GEPIIs. These probes were developed on a recently identified K^+ binding protein, which was found in *E.coli and* referred to as Kbp. The role of Kbp, a protein formerly known as YgaU, was characterized and published in May 2016, some months before I started my PhD under the supervision of Prof. Dr. Roland Malli. Based on this protein, we decided to explore whether the usage of Kbp within a fluorescence resonance energy transfer (FRET-) based sensor is suitable to yield functional K^+ probes. Within this thesis we demonstrate the suitability of these GEPIIs for the visualization of K^+ alterations and dynamics *in vitro*, *in situ* and *in vivo*. Our data emphasize that the usage of GEPIIs will fundamentally contribute to a better understanding of the cellular and organismal K^+ homeostasis and the role of K^+ on the subcellular level in physiology and pathology.

Acknowledgements

PhD student Helmut Bischof received funding from the Austrian Science Fund (FWF, P28529-B27 to Roland Malli) and the Medical University of Graz through the PhD Program Molecular Medicin (MOLMED).

Danksagung

Ich möchte mich an dieser Stelle bei allen bedanken, die mir während meiner Dissertation zur Seite gestanden sind. Dieser Dank gilt vor allem meiner Familie und meinen Freunden welche mich stets ermutigt und mir Rückhalt gegeben haben.

Ein riesen Dankeschön gilt meinem Betreuer, Prof. Roland Malli, welcher stets Zeit für hilfreiche Diskussionen fand, und mir so viele Dinge im Bereich der Zellphysiologie und –pathologie, Methoden und dem Design von Experimenten sowie Interpretation von Daten beibrachte.

Ich bedanke mich bei Prof. Wolfgang Graier, Mitglied meines Dissertationskommitees, für die großartige Co-Betreuung und die vielen interessanten Diskussionen.

Ein weiterer Dank für die wissenschaftliche Begleitung während meines PhD-Studiums gilt Prof. Klaus Groschner, ebenfalls Mitglied meines Dissertationskommittees.

Ich danke all meinen weiteren Co-Autoren, Markus Rehberg, Sarah Stryeck, Katharina Artinger, Emrah Eroglu, Markus Waldeck-Weiermair, Benjamin Gottschalk, Rene Rost, Andras T. Deak, Tobias Niedrist, Nemanja Vujic, Hanna Lindermuth, Ruth Prassl, Brigitte Pelzmann, Klaus Groschner, Dagmar Kratky, Kathrin Eller, Alexander R. Rosenkranz, Tobias Madl und Nikolaus Plesnila für ihre großartige Arbeit

Vielen Dank auch an Markus, meinen früheren Betreuer der Bachelorarbeit, für die Hilfe bei etwaigen Problemen.

Vielen Dank an Rene und Anna für die besondere Unterstützung in der Zellkultur!

Ich bedanke mich bei all meinen Labor Kollegen der AG-Graier und AG-Malli für die regen Diskussionen, das tolle Arbeitsklima und die gute Zusammenarbeit.

Zu guter letzt gilt ein besonderer Dank meiner Kollegin und Freundin Sandra Burgstaller für unzählige hilfreiche Diskussionen, Inputs zu den Methoden und experimentellen Ratschlägen, sowie das Korrekturlesen der Publikation und Dissertation.

Table of Contents

Abbreviations and Definitions

$[Ca^{2+}]$	Calcium ion concentration
$[Ca^{2+}]_{cyto}$	Cytosolic calcium ion concentration
$[Ca^{2+}]_{i}$	Intracellular calcium ion concentration
[ion]	Ion concentration
$[K^{+}]$	Potassium ion concentration
$[K^{+}]_{cyto}$	Cytosolic potassium ion concentration
$[K^{+}]_{ex}$	Extracellular potassium ion concentration
$[K^{+}]_{i}$	Intracellular potassium ion concentration
$[K^{+}]_{mito}$	Mitochondrial potassium ion concentration
$[K^{+}]_{nuc}$	Nuclear potassium ion concentration
$[Na^{+}]$	Sodium ion concentration
$[Na^{+}]_{i}$	Intracellular sodium ion concentration
2-DG	2-deoxy-D-glucose
ADP	Adenosine-5‘-diphosphate
ATP	Adenosine-5‘-triphosphate
BFP	Blue fluorescent protein
BK channel	“Big” potassium ion channel
BON	bacterial OsmY and nodulation
Ca^{2+}	Calcium ion
CaM	Calmodulin
CCT	Cortical collecting duct
CD	Cluster of differentiation
CFP	Cyan fluorescent protein
Cl^{-}	Chloride ion
CNS	Central nervous system
cpFP	Circularly permuted fluorescent protein
Cs^{+}	Cesium ion
DCT	Distal convoluted tubule
EC_{50}	Half-maximal effective concentration
FP	Fluorescent protein
FRET	Förster resonance energy transfer
fRFP	Far-red fluorescent protein

GECO	Genetically encoded Ca^{2+} indicator for optical imaging
geNOp	Genetically encoded nitric oxide probe
GEP	Genetically encoded probe
GEPII	Genetically encoded potassium ion indicator
GFP	Green fluorescent protein
GIRK channel	G-protein coupled inwardly rectifying potassium channel
GPCR	G-protein coupled receptor
H^+	Proton
HD-P	Hemodialysis patient
ICT	Initial collecting duct
IFNγ	Interferon gamma
IL-2	Interleukin-2
IP_3	1,4,5-inositol triphosphate
IP_3R	1,4,5-inositol triphosphate receptor
IRI	Ischemia reperfusion injury
ISE	Ion-selective electrode
K^+	Potassium ion
K^+/H^+ ATPase	Potassium ion/proton Adenosine-5‘-triphosphatase
K2P channels	Two-pore domain K^+ channel
Kbp	Potassium binding protein
K_D	Dissociation rate constant
Kir channels	Inwardly rectifying potassium ion channels
Kv channels	Voltage gated potassium ion channels
Lc-BON	Low-charge BON
Lc-LysM	Low-charge LysM
LDL	Low density lipoprotein
LysM	Lysine motif
MCD	Medullary collecting duct
Mg^{2+}	Magnesium ion
MHC	Major histocompatibility complex
Mn^{2+}	Manganese ion
Na^+	Sodium ion
Na^+/K^+ ATPase	Sodium ion/potassium ion adenosine-5‘-triphosphatase
NH_4^+	Ammonium ion

NKCC2	Sodium ion/potassium ion/2 chloride ion cotransporter
OFP	Orange fluorescent protein
PCT	Proximal convoluted tubule
Pi	Inorganic phosphate
PI_3K	Phosphoinositide 3-kinase
QUEEN	Quantitative evaluators of cellular energy
Rb^+	Rubidium ion
RFP	Red fluorescent protein
R-GEPII	Red-shifted genetically encoded potassium ion indicator
RpoS	RNA polymerase sigma S
SKCa channels	Small conductance calcium ion activated potassium ion channel
SLO channels	Slowpoke potassium ion channel
TAL	Thick ascending limb
TCR	T-cell receptor
UVFP	Ultraviolet fluorescent protein
YFP	Yellow fluorescent protein

List of Figures

List of Tables

Kurzzusammenfassung

Intra- und extrazelluläre Kalium-Ionen (K^+) Konzentrationen regulieren viele essentielle zelluläre und biologische Funktionen. Nichtsdestotrotz mangelt es noch heute an verwendbaren K^+-sensitiven Sensoren. Basierend auf der Dringlichkeit solcher Messmethoden haben wir vor kurzem genetisch codierte, Förster Resonanz Energie Transfer (FRET-) basierte, K^+-sensitive Sensoren entwickelt, welche die Echtzeitmessung von intra- und extrazellulären K^+ Dynamiken erlauben. Diese neuen Sensoren, auch GEPIIs (genetisch codierte Kalium-Ionen Indikatoren) genannt, bestehen aus einem bakteriellen, K^+-bindenden Protein, welches von einem türkis- und einem gelb-fluoreszierenden Protein flankiert wird. Die Bindung von K^+ an diese Konstrukte bewirkt eine massive Zunahme des FRET-Signals, welches in einem hohen Signal zu Rausch Verhältnis resultiert. Die Anwendung von GEPIIs als rekombinantes Protein erlaubt eine schnelle und präzise Bestimmung von K^+ Konzentrationen in verschiedenen Körperflüssigkeiten. Des Weiteren erlaubte die Verwendung des rekombinanten Sensorproteins die Visualisierung von Zellwachstum und Zelltod mit hoher räumlicher und zeitlicher Auflösung. Die gereinigten Sensorproteine stellten sich auch für die Visualisierung von K^+ Dynamiken im Gewebe lebender Tiere als geeignet heraus. Die Expression von GEPIIs in lebenden Pankreaszellen erlaubte präzise Echtzeit-Messungen von subzellulären K^+ Signalen während der Zell-Depolarisation. Zusammengefasst stellen GEPIIs ein wertvolles Tool für die Durchführung verschiedener K^+ Analysen dar, und werden in Zukunft neue, bahnbrechende Möglichkeiten für subzelluläre K^+ Messungen in lebenden Zellen eröffnen.

Abstract

The maintenance of intra- and extracellular potassium ion (K^+) concentrations is important for many cellular processes and biological functions. Based on the urgent need of detection methods for K^+, due to the lack of applicable probes, we have recently developed Förster resonance energy transfer (FRET)- based K^+ sensitive probes, allowing the real-time visualization of intra- and extracellular K^+ dynamics. These probes, referred to as GEPIIs (genetically encoded potassium ion indicators), consist of a bacteria-derived K^+ binding protein, Kbp, sandwiched by a cyan and a yellow fluorescent protein variant. Upon K^+ binding to these chimeras, FRET-signals increase dramatically, yielding a high signal to noise ratio. Recombinant GEPIIs are suitable for the quantification of K^+ levels in diverse bodily fluids in a fast and convenient manner. Moreover, the recombinant protein proved suitable for monitoring cell viability and cell growth with high spatial and temporal resolution. In addition, purified GEPIIs can be applied *in vivo* for the visualization of extracellular K^+ dynamics in tissues of living animals. Expression of GEPIIs in cells allows hitherto unfeasible real-time detection of subcellular K^+ dynamics. Our data highlight organelle specific K^+ fluxes in response to cell depolarization. Altogether, our data emphasize that GEPIIs are suitable for diverse K^+ assays and will open new avenues for live-cell K^+ imaging in future.

1 Introduction

Potassium ions (K^+) represent the most abundant intracellular cation (1,2). Besides their important function in keeping cellular osmolarity (2), K^+ is associated with many processes and functions in (patho-) physiology (3–5). As an example, K^+ is fundamentally involved in cellular processes such as regulating cell volume (6), cell excitability (7) or exo- and endocytosis (8,9). Recent research even identified a participation of K^+ in the regulation of several enzymatic activities (10–13). However, many (sub-) cellular dysfunctions associated with disturbances of the K^+ homeostasis are still far from being understood due to the lack of applicable detection methods for K^+ (14–16). Hence, the development of K^+ sensitive probes, suitable for the application and quantification of K^+ in single living cells or *in vivo*, is of great interest in cell biology and (patho-) physiology research.

1.1 Maintenance of the K^+ homeostasis within organisms

One of the most important regulations of K^+ concentrations ($[K^+]$) in an organism takes place at the cellular level, as maintenance of the cellular K^+ homeostasis is important for many essential cellular processes (1,17). Thus, it is not surprising that a huge variety of K^+ channels and transporters are present within cells and their organelles (18–20).

1.1.1 Regulation of intracellular $[K^+]$ by Na^+/K^+ ATPase

The most important and prominent example of an active K^+ transporter is the sodium ion (Na^+)/K^+ pump, also referred to as Na^+/K^+ adenosine-5'-triphosphatase (ATPase) (**Figure 1**) (21). The transporter exchanges two K^+ from the extracellular space against three intracellular Na^+ (**Figure 1**) (22–24). Thus, it is fundamentally involved in the maintenance of the cellular K^+ gradient across the plasma membrane (25). However, the exchange is energy dependent, as ATP is hydrolyzed to adenosine-5'-diphosphate (ADP) and inorganic phosphate (Pi) (**Figure 1**) (26,27). It is assumed that around 50% of the energy generated within the central nervous system (CNS) are consumed by the active K^+ transporter to maintain intracellular $[K^+]$ (28,29).

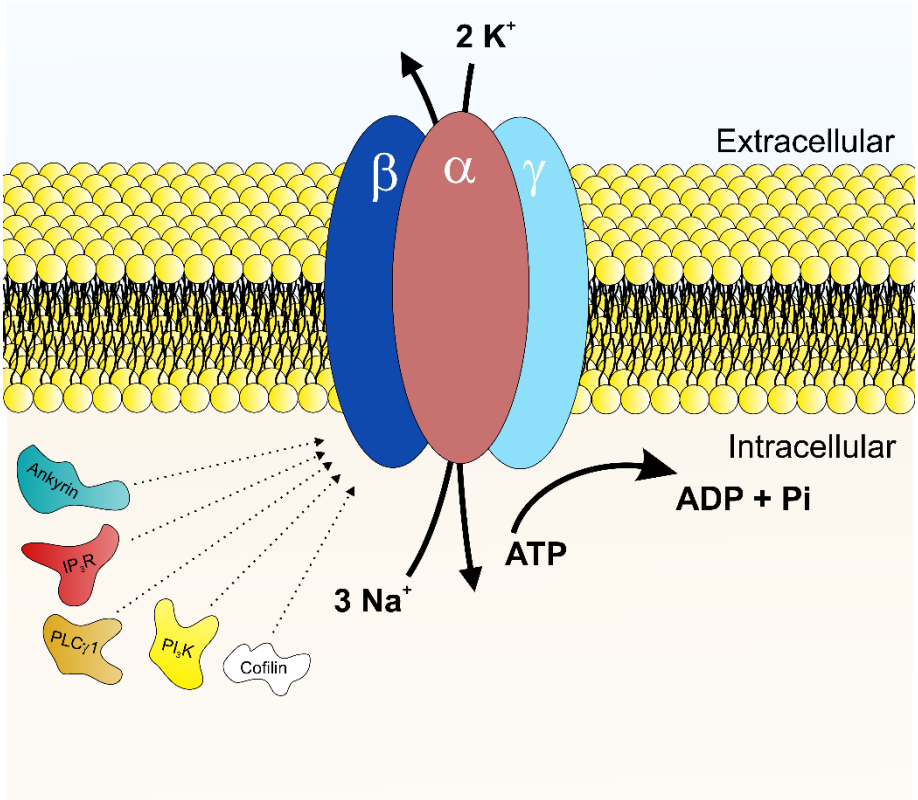

Figure 1: Schematic representation of the Na^+/K^+ ATPase located in the plasma membrane of eukaryotic cells. The Na^+/K^+ ATPase represents a multimeric protein complex composed of different subunits, including α- (brownish), β- (dark blue) and γ subunits (light blue), located in the plasma membrane of eukaryotic cells. Upon hydrolysis of ATP to ADP + Pi the multimeric protein complex exchanges three intracellular Na^+ for two extracellular K^+, thereby generating a K^+ gradient across the plasma membrane. Selected interaction partners of the Na^+/K^+ ATPase such as ankyrin (turquoise), IP_3R (red), PLCγ1 (brown), PI_3K (yellow) and cofilin (white) are shown. Figure according to Dempski et al., 2005, Cortes et al., 2006, Dempski et al., 2008, Geering, 2008 and Ogawa et al., 2009 (23,25,30–32).

From a structural point of view, the transporter consists of several subunits, including α, β and γ fragments (25,30), where the α subunit represents the catalytic core, hydrolyzing ATP and transporting the cations (31), the β subunit fulfills chaperone functions (23) and the γ subunit essentially contributes in the modulation of Na^+/K^+ ATPase activity (**Figure 1**) (32).

Interestingly, interactions of the Na^+/K^+ ATPase with ankyrin (33), attaching integral membrane proteins to elements of the cytoskeleton (34), phospholipase Cγ1 (35), a key player in the generation of 1,4,5-inositol triphosphate (IP_3) (36) or the IP_3 receptor (IP_3R) directly (37), a membrane protein complex acting as a calcium ion (Ca^{2+}) channel (38) have been described (**Figure 1**). Moreover, interactions of the Na^+/K^+ ATPase with the phosphoinositide 3-kinase (PI_3K) (39) involved in fundamental cellular function such as cell growth and differentiation (40) or cofilin, an actin disassembling protein, were described previously (**Figure 1**) (41,42).

A localization of the Na^+/K^+ ATPase was, although rarely described, not only observed at the plasma membrane, but also within the nuclear envelope of cells (43). While controversial, as nuclear pores seem to be nonrestrictive to small ions or molecules (44,45), the Na^+/K^+ ATPase within the nuclear envelope generates Na^+/K^+ gradients between the nucleo- and cytoplasm across the nuclear envelope (43). Garner determined basal nuclear [K^+] in rat hepatocytes of ~150 mM K^+ within the nucleus and ~110 mM K^+ within the cytosol, using chemical fluorescent K^+ indicators (43). This study is in line with older findings from the 1970s (46) and 1980s (47) describing elevated nuclear [K^+]. Nonetheless, until today, the physiological relevance of a Na^+/K^+ ATPase located within the nuclear envelope remains elusive.

1.1.2 Regulation of intracellular [K^+] by K^+ channels

Besides the intracellular distribution of the Na^+/K^+ ATPase, a huge variety of K^+ channels is spread within the membrane of cellular organelles and the plasma membrane (48). These K^+ channels are divided into five different subfamilies (49), including voltage gated K^+ (Kv) channels (**Figure 2a**) (50), inwardly rectifying K^+ (Kir) channels (**Figure 2b**) (51), two-pore domain K^+ (K2P) channels (**Figure 2c**) (52), small conductance Ca^{2+} activated K^+ (SKCa) channels (**Figure 2d**) (53) and the slowpoke K^+ (SLO) channel family (**Figure 2e**) (54,55).

Each of these subfamilies contains multiple members, resulting in a total of ~100 K^+ channel encoding genes in mammals (56). Typically, each K^+ channel is associated with specialized functions within cells (50–56). Thus their expression is highly regulated and cell type as well as tissue specific (48,55,56).

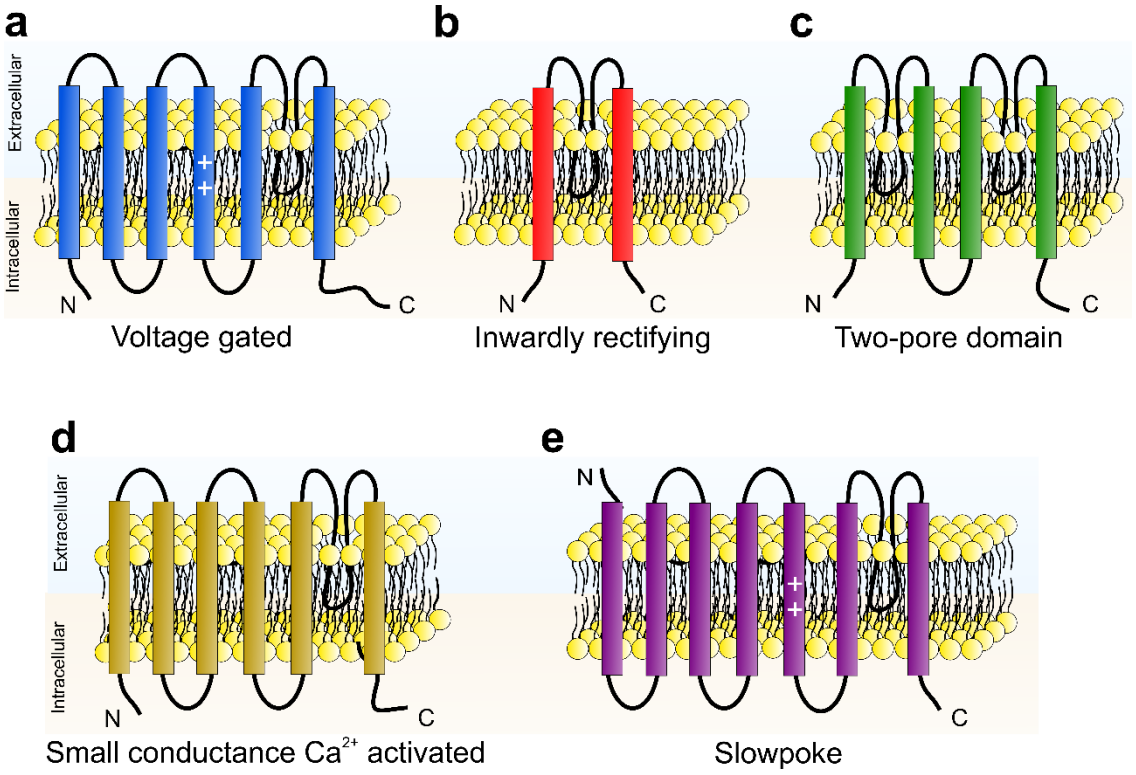

Figure 2: Schematic representation of different K^+ channel subfamilies. Extracellular face of the plasma membrane (PM) is represented in light blue, intracellular side in light yellow. Loop regions of all channels are represented in black, transmembrane helices as colored rectangles. (**a**) Schematic demonstration of the voltage gated K^+ (Kv) channel family. The channels consist of six trans-membrane helices (blue rectangles), N- and C-terminus are located within the cytosol. The voltage sensing domain of these channels is indicated with "++". The extracellular loop connecting the 5th and 6th helix of the channel is internalizing into the PM. (**b**) Schemata demonstrating the structure of inwardly rectifying K^+ (Kir) channels, consisting of two transmembrane helices (red rectangles). Of note, the inter-helical linker located at the extracellular site of the PM represents a membrane internalizing loop. N- and C- terminus are located within the cytosol. (**c**) Architecture of two-pore domain K^+ (K2P) channels, consisting of four transmembrane helices (green rectangles). N- and C- terminus are located within the cytosol, loops connecting helix 1 with helix 2 and helix 3 with helix 4 integrate into the PM at the extracellular space. (**d**) Panel demonstrates the structure of small conductance Ca^{2+} activated K^+ (SKCa) channels (brown rectangles). Notably the structure is similar to Kv channels (**a**), however, these channels are lacking the voltage sensitive domain. N- and C- terminus are located within the cytosol. (**e**) Schematic representation of slowpoke K^+ (SLO) channels consisting of seven transmembrane helices (violet rectangles). Similar to Kvs, these channels possess a voltage sensitive domain (++), involved in the gating of the channel. The N- terminus of these channels is facing the extracellular side, while the C- terminus is located intracellular. Figure according to Gonzalez et al., 2012 (49).

I) Voltage gated K^+ (Kv) channels

As already suggested by the nomenclature, Kv channels (**Figure 2a**) conduct in response to changes of the membrane potential (50,57). Within the family of K^+ channels, the Kv channel subfamily represents the most extensive one, with 40 identified, Kv encoding genes in humans (58). These channels are especially important for excitable cells in order to remain their functionality (59). However, also their involvement in apoptosis (60), cell differentiation (61) and growth (62), or the maintenance of cardiac activity (63) has been demonstrated.

II) Inwardly rectifying K^+ (Kir) channels

A second important subfamily of K^+ channels are the Kir channels (**Figure 2b**) (51). This subfamily can further be divided into four functional groups, including classical Kir channels, being constitutively active and exhibiting strong inward rectification (64), G-protein coupled inwardly rectifying K^+ (GIRK) channels, stimulated by the β/χ subunits of activated G-protein coupled receptors (GPCRs) upon their agonist binding (65), ATP-sensitive K^+ (K_{ATP}) channels (66) and K^+-transport channels (KTCs) (51).

Constitutively active Kir channels are especially expressed within glia cells of the central nervous system (CNS), where they establish the high K^+ selectivity of the glia cell membrane (67). Additionally, within these cells these channels generate a strongly negative resting membrane potential (67), providing a driving force for the spatial K^+ buffering by glia cells within the CNS (67,68).

GIRK channels are mainly found in neurons and atrial myocytes (69). In neurons, these channels represent regulators of neuronal excitability (70). Recently, these channels have even been linked to the development of addictions, as GIRK knockout mice show altered behavior in response to addictive drugs (70). In addition, exposure of mice to addictive drugs results in altered surface expression patterns of GIRK channels within neurons (70). Besides the function of GIRK channels in neurons, these channels are fundamentally involved in cardiac repolarization (71) and are, for example, activated via GPCR-binding of the cholinergic agonist carbachol (72), yielding a cellular K^+ influx and hyperpolarization of cardiac myocytes (73).

K_{ATP} channels are typically found within metabolically active tissues (74) as well as cardiac tissue in a high concentration (75). In the heart these channels are fundamentally involved in the adaption to ventricular pressure load (76), are blocked by high concentrations of ATP (77) and thus serve as metabolic sensors that crosslink cell metabolism with changes in their electrical potential (78).

KTCs are found especially in polarized or excitable cells, such as kidney cells (79) and neurons (64), where KTCs are essentially involved in setting the resting membrane potential and are important for the regulation of the intracellular K^+ concentration ($[K^+]_i$) (64).

III) Two-pore domain K^+ (K2P) channels

Third, K2P channels (**Figure 2c**) are considered as K^+ selective leak channels (80), gated by changes in pH (81), stretch (82) or temperature (83). Additionally, these channels are activated upon coupling to G-proteins (84) or after administration of anesthetics (85). Nowadays, 15 members of this K^+ channel subfamily have been identified (86), however, their precise physiological function remains elusive until today (87). Nonetheless, they significantly contribute to the maintenance of the resting membrane potential (88) and are mainly expressed in sensory and motor neurons of the autonomic nervous system (89), as well as retinal ganglion cells (88). Prominent examples of these K2P channels are, for example, TREK (90) or TASK (91) channels.

IV) Small conductance Ca^{2+} activated (SKCa) channels

Fourth, the family of SKCa channels (**Figure 2d**) belongs to K^+ channels activated by an increase in intracellular Ca^{2+} concentration ($[Ca^{2+}]_i$) (92). Their name, small conductance Ca^{2+} activated K^+ channels, refers to their small conductance generated upon channel opening (93). In principal, they are divided into three subtypes including SKCa1, SKCa2 and SKCa3 (49). Originally, these channels were discovered in red blood cells and were first cloned by Köhler et al. in 1996, who described them as calcium-activated, voltage independent K^+ channels when expressed in Xenopus oocytes (93). In principal, several members of this subfamily are considered to act as tetramers due to their similarity with Kv channels (49).

V) Slowpoke K^+ (SLO) channels

Last, K^+ channels of the SLO family (**Figure 2e**) are encoded by so called SLO genes (54). One characteristic of these channels is that they feature an unusual large conductance upon activation (94). One famous example of these channels is the “big” K^+ (BK) channel (95), which is activated by both, changes in membrane potential and an increase in $[Ca^{2+}]_i$ (96). In mammals, the SLO family is encoded by four genes, including Slo1, Slo2.1, Slo2.2 and Slo3 (49). Typically, changes of various intracellular ions, such as Ca^{2+} (96), Na^+ (97), chloride ions (Cl^-) (98), or protons (H^+) (99) activate these channels (54). All four members of the SLO family are activated by specific ions (96–99), leading to a link between the intracellular ion metabolism with the cellular membrane K^+ conductance. Their expression is typically associated with all types of excitable cells, including neurons (100), smooth- (101) and skeleton muscle cells (102), endocrine cells (103), or astrocytes (104) and microglia (54,105).

1.1.3 Maintenance of the organismal $[K^+]$

All mammalian cells and their organelles have an absolute requirement for K^+ to fulfill their physiological function (1). However, global hypo- as well as hyperkaliemia come along with severe systemic diseases, including tiredness, hypo- or hypertension, heart rate alterations or even heart failure (106,107). Thus, it is of great importance to keep the extracellular K^+ concentrations ($[K^+]_{ex}$) within a narrow physiological range of ~ 3.5 – 5.0 mM K^+ (108). Welch et al. performed a study in 2009 including 10 European countries, focusing on the uptake of selected minerals. The study pointed to huge geographical differences in the amount of K^+ intake, with cross-country differences of greater than 35% for both sexes. Nonetheless, despite these massive differences concerning the K^+ uptake of individuals, no evidences for a positive correlation of K^+ intake and serum K^+ levels are existent (109). In healthy individuals, at least, K^+ excretion is increasing upon enhanced uptake, indicating that the resorption of K^+ via the digestive tract as well as its systemic elimination is tightly regulated to maintain the physiologic $[K^+]_{ex}$ in the body (1,110).

Usually, the kidney is responsible for the maintenance of a constant total body K^+ level (111). This is achieved via the specialized structural and cellular organization of the nephron, which can be divided into several subparts (**Figure 3**) (112).

These include the glomerulus, proximal convoluted tubule (PCT), loop of Henle and the distal convoluted tubule (DCT), composed of the thick ascending limb (TAL), initial and cortical collecting duct (ICT/CCT) and the medullary collecting duct (MCD) (**Figure 3**) (113).

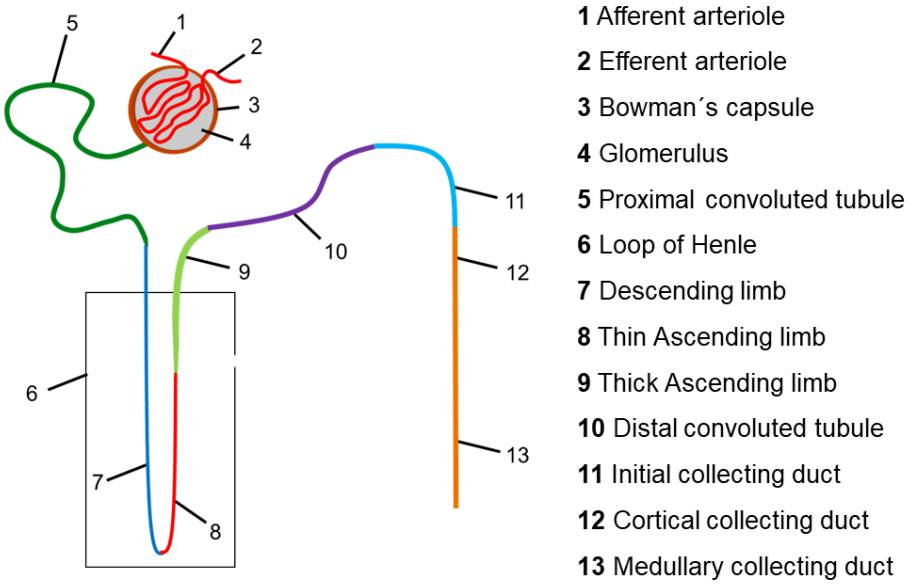

Figure 3: Schematic representation of the nephron anatomy. The anatomy of the kidney is organized in nephron structures as demonstrated in the schemata. Blood enters the bowman's capsule (3) and the glomerulus (4) via the afferent arteriole (1) and leaves via the efferent arteriole (2). Collected liquid moves from the glomerulus (4) to the proximal convoluted tubule (5) and enters the loop of Henle (6) composed of the descending (7) and the thin ascending limb (8). Further it moves via the thick ascending limb (9), the distal convoluted tubule (10), the initial collecting duct (11) and the cortical collecting duct (12) to the medullary collecting duct (13), where the urine is afterwards collected and excreted. Figure according to Thevenod and Wolff, 2016 (114).

It is estimated that ~ 75% of all K^+ is already reabsorbed in the PCT of the nephron (**Figure 3**) (1,115). In principal, two different modes of K^+ reabsorption have been identified within the PCT, including the solvent drag, being dependent on the flow of water rather than active transport, and the lumen-positive potential facilitating ion fluxes across a gradient (**Figure 4a**) (116). Further ~ 20% of K^+ is reabsorbed within the TAL, via trans- and paracellular pathways (**Figure 4b**). The transcellular pathway is achieved via the $Na^+/K^+/2Cl^-$ cotransporter (NKCC2), moving Na^+, K^+ and Cl^- from the lumen of the tubule into the cells (**Figure 4b**) (117). Further, especially the secretion of K^+ and Cl^- is essentially regulated to stimulate the paracellular K^+ reabsorption pathway via the lumen-positive potential (**Figure 4b**) (117). While passing the ICD and CCD, K^+ is reabsorbed via a transcellular pathway, via the ATP dependent K^+/H^+ exchanger (**Figure 4c**). However, in total, only ~ 2% are reabsorbed via these pumps (116,118,119).

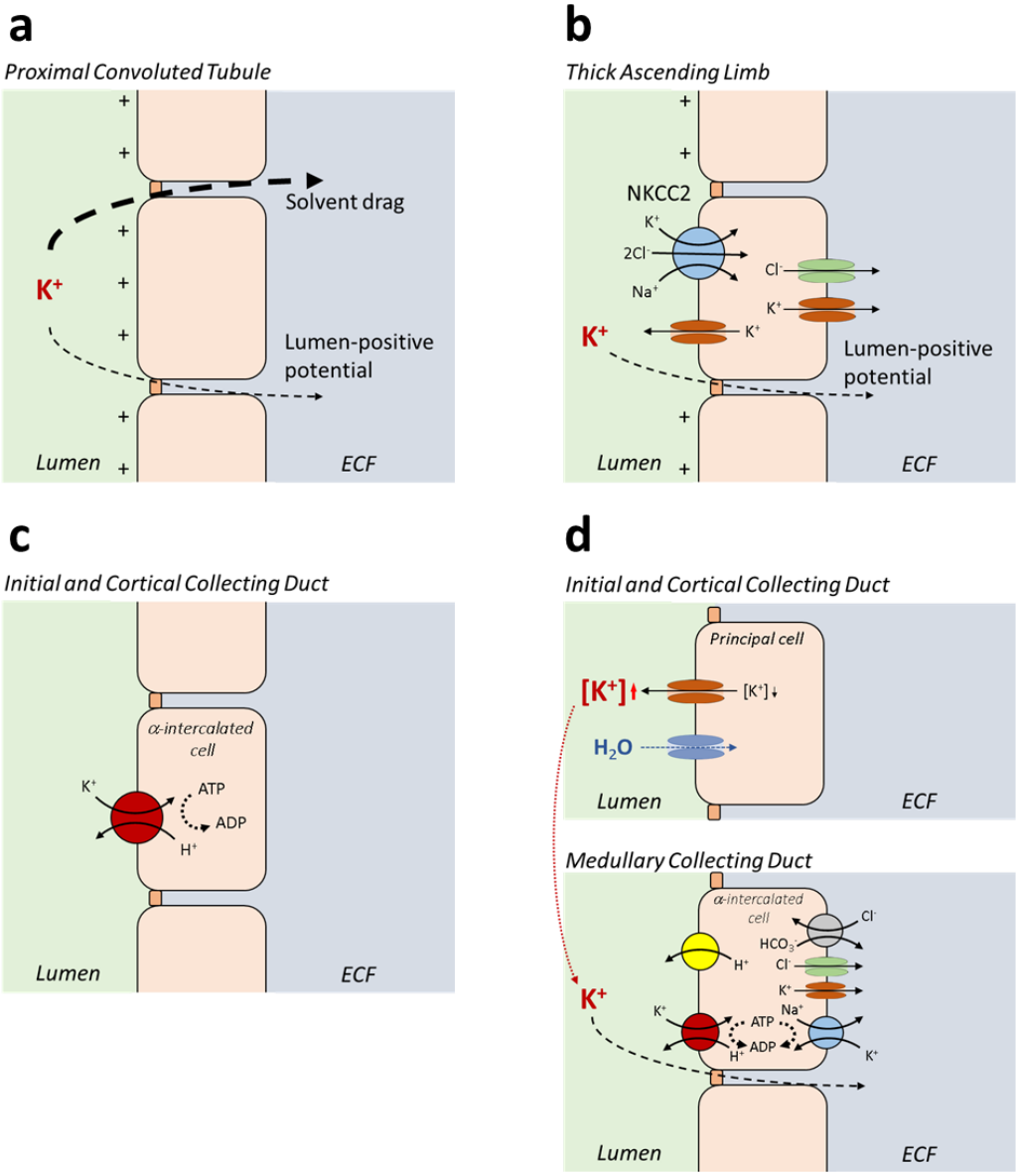

Figure 4: Pathways of ion resorption in different segments of the kidney. Schematic cross sections of cells (beige), the tubule duct lumen (green) and the extracellular fluid (ECF, blue) are represented. (**a**) Schematic illustration of K^+ reabsorption in the proximal convoluted tubule. "+" indicates a positive potential within the lumen of the duct. K^+ within the proximal convoluted tubule is mainly reabsorbed via paracellular pathways including the solvent drag, but also via the lumen-positive potential, acting as a driving force for K^+ to reenter the ECF. (**b**) Within the thick ascending limb, K^+ is reabsorbed into the ECF via both, trans- and paracellular pathways. The lumen-positive potential, generated by the positive potential within the lumen of the duct (+), as well as the transcellular pathways are involved. The transcellular pathway is stimulated via $Na^+/K^+/Cl^-$ cotransporter 2 (NKCC2, blue) located at the apical side of the cells. Intracellular K^+ is then leaking from the cells to both sides, the ECF and back to the lumen via K^+ leak channels (orange), while Cl- leak channels (green) are located at the basal side of the cells. (**c**) K^+ reabsorption within the initial and cortical collecting duct is achieved via K^+/H^+ ATPases of α-intercalated cells, exchanging intracellular H^+ for extracellular K^+ upon hydrolysis of ATP. Furthermore, principal cells within the initial and cortical collecting duct possess K^+ leak (orange)- and H_2O channels (aquaporins, light blue) on their apical side (d, upper panel), leading to K^+ extrusion from the cells, resulting in reduced $[K^+]_i$ and increased $[K^+]$ in the lumen of the duct. The increased $[K^+]_{ex}$ stimulates the paracellular K^+ reabsorption in the medullary collecting duct (d, lower panel). Additionally, α-intercalated cells support the final renal K^+ reabsorption via K^+/H^+ ATPases (red circle) within their apical membrane, while on the basal membrane Na^+/K^+ ATPases (light blue), K^+ (orange) and Cl^- leak channels (green) and HCO_3^-/Cl^- exchangers (grey) are located. Figure according to Palmer, 2015 (1).

Although seeming controversial, principal cells located in the collecting duct secrete K^+ into the lumen of the duct, while absorbing H_2O, thus concentrating luminal [K^+] (**Figure 4d,** upper panel) (120). Finally, during passing the MCD, the increased [K^+] is reabsorbed via both, passive trans- and active paracellular transport of the K^+/H^+ ATPase (**Figure 4d,** lower panel), finally leading to only ~ 2% of initially secreted K^+ being excreted via the urine (121,122).

Considering the strict K^+ homeostasis handling of the kidney, still, it is rather a long-term regulation (119). Initially, alterations of the extracellular K^+ concentration ($[K^+]_e$) are buffered by skeleton muscle cells, which incorporate additional amounts of K^+ (17). The regulation of these K^+ movements is considered to be regulated mainly by two factors including insulin (123) and catecholamines (124). First, insulin secretion from pancreatic β-cells does not only stimulate glucose, but also K^+ uptake into insulin-responsive tissues (123). However, the effect of insulin on glucose and K^+ uptake are differential, as, for example, patients with a chronic kidney disease show impaired insulin-stimulated glucose uptake, whereas their cellular K^+ absorption remains unaffected (125). Second, catecholamines such as adrenaline or noradrenaline essentially participate in the regulation of plasma [K^+] (124). Typically, administration of (nor)adrenaline causes a short transient serum hyperkalemia caused by the activation of hepatic KCa channels, followed by a second phase of serum hypokalemia due to the activation of Na^+/K^+ ATPase by β-adrenoreceptors (124).

1.2 K^+ and its implication in health and disease

1.2.1 K^+ and the regulation of the cell volume

Nowadays it is well accepted that K^+ represents the most abundant intracellular cation (1,17), fundamentally involved in the regulation of the cell volume (6). However, until around the 1920s, scientists believed that animal cells, especially red blood cells, maintained a constant cell volume as the plasma membrane was thought to be impermeable for extracellular cations such as K^+, and especially Na^+ (126). However, already some years later Jacobs et al. recognized that an impermeability of the cell membrane for cations would lead to colloid-osmotic swelling of red blood cells and finally, their hemolysis (127). The first evidence for cation permeable cell membranes was achieved using isotopic tracers (128). From this time on, scientists recognized the importance of a cation permeable cell membrane to prevent cells from swelling and finally their death. Based on this ability of cells to dynamically regulate their ion homeostasis across the cell membrane, Tosteson et al. established a mathematical model estimating cell volume changes in response to high or low extracellular ion concentrations ([ion]) (129). Experiments performed to proof their model pointed to the ability of red blood cells to regulate their K^+ uptake or K^+ excretion depending on $[K^+]_{ex}$ (130).

Almost 20 years later, in the middle of the 1980s, Tivey et. al depicted that also other cells such as HeLa, show an increase in their cell volume upon exposure to hypo-osmolar solutions (131). However, the increase was not as great as one would predict using a theoretical model (131). Their experiments demonstrated that cells fight their swelling and volume uptake by excreting K^+ from the cytoplasm, probably to prevent membrane disruption. Vice versa, if cells were exposed to hyperosmolar solutions, HeLa cells incorporated additional K^+ to keep their osmolarity. Already these early and rather simple experiments pointed to the important role of K^+ in the regulation of the cell volume (131).

It was recently identified, that such cellular volume alterations are fundamentally involved in the progression of the cell cycle of many cell types (132–134). Thus, for example BSC1 cells, a monkey kidney cell line, exhibit a volume loss of 20-50% during the transition from prophase to metaphase (132). These results demonstrate the importance of an adjustable cell volume not only for the adaption to changes in

the extracellular milieu (130), but also for cell division (132). Although data demonstrating a change in the K^+ channel expression patterns during these progressions of the cell cycle are available (135), a direct evidence whether or not $[K^+]_i$ changes are involved and occur during these volume alterations remains elusive until today.

1.2.2 K^+ and the membrane potential

In principal, the term “membrane potential” describes the difference of an electric potential between the inside and outside of a cell (136). This difference is generated by ion- and charge gradients towards the plasma membrane (137), especially including Ca^{2+} (138), chloride ions (Cl^-) (139), magnesium ions (Mg^{2+}) (140), K^+, Na^+ (141) and organic anions (**Figure 5**) (142).

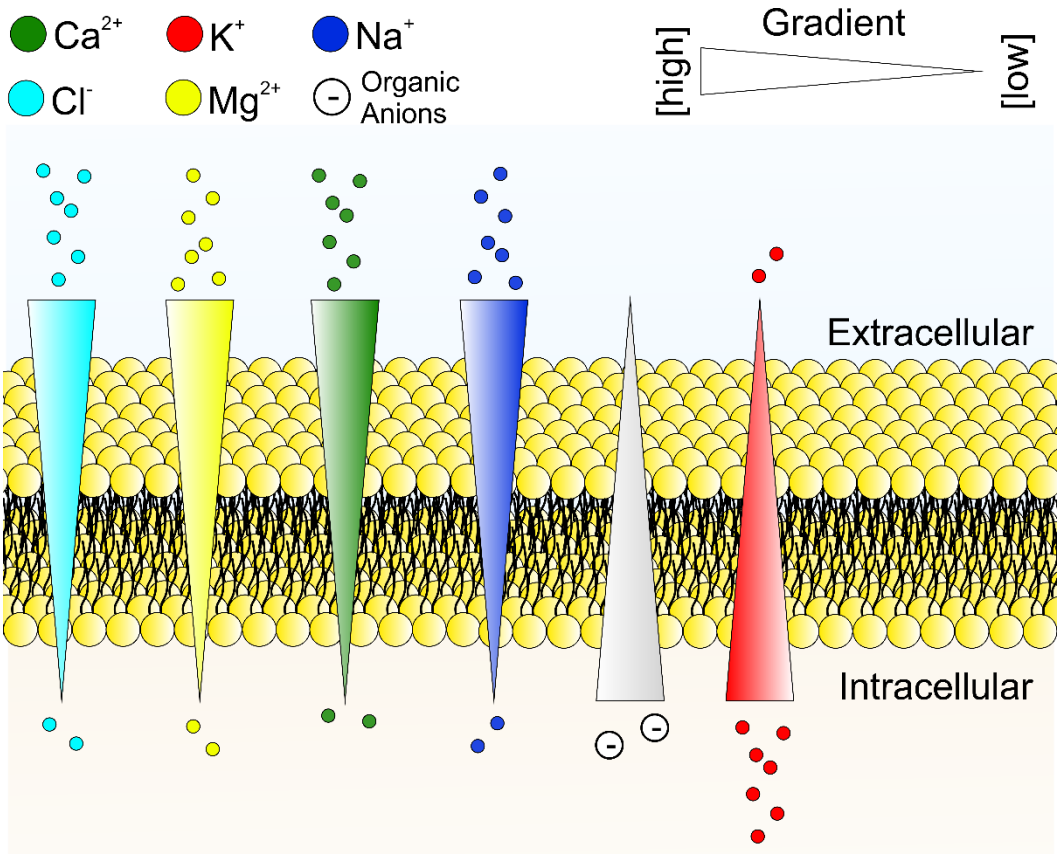

Figure 5: Schematic illustration of ion distributions across the cell membrane. Schematic cross section across the cell plasma membrane (phospholipid bilayer, yellow head groups, black tails). Extracellular- (upper, light blue) and intracellular side (lower, light orange) of the plasma membrane is represented. Distribution of Ca^{2+} (green), Cl^- (turquoise), K^+ (red), Mg^{2+} (yellow), Na^+ (blue) and organic anions (grey) is represented via a triangle gradient scale, where the broad side represents high concentration ([high]) and thin side low ([low], white triangle, upper right) ion concentrations. Cell membrane potential is generated by tightly regulating and maintaining different [ion] distributions across the plasma membrane. Figure according to Wilbrandt, 1937, Dulhunty 1978, Sheu et al., 1983, Miao et al., 1993, Bara et al., 1997, Ma et al., 2017 and Roux 2008 (136–142).

In the early 19th century, Hober et al. reported an influence of ion concentrations ([ion]) on the cellular trans-plasma membrane current in muscle tissue (143). At the beginning, these relationships were studied in frog sartorius muscles using internal microelectrodes to investigate, how predicted models correlated with experimental relations (143). Several years later scientists investigated the role of various $[K^+]_{ex}$ on the membrane potential, as under physiologic conditions very high concentrations of K^+ are present within the cell (~ 140 mM), but only very low concentrations in the extracellular space (~ 5 mM) (144). Thus, small changes in $[K^+]_{ex}$ strongly affect the membrane potential of a cell, which is typically ranging from -40 mV to -80 mV under basal conditions (145).

The fact that also intracellular organelles such as mitochondria can possess a membrane potential was first described in the 1930s (146). Peter Mitchell, one of the pioneers in mitochondria research, recognized that energy synthesis via complex I-V of the mitochondrial respiratory chain is strictly coupled to the membrane of the organelle (147). Membrane disruption of respirating mitochondria thereby drastically decreased ATP synthesis, indicating that the intact mitochondrial membrane represents an important feature for energy production (147).

In principal, the membrane potential of a cell fulfills two functions: firstly, it allows the cell to store energy in form of an electrochemical gradient, which, for example, mitochondria use for the generation of energy (148). Secondly, the electrochemical gradient is essential for excitable cells such as muscle cells and neurons, in order to allow signal transmission and progression (149). However, the fact that K^+ is not only important for the cell in order to keep osmolarity, but also to remain excitable is well known today.

1.2.3 Regulation of exo- and endocytosis by K^+

K^+ is fundamentally involved in the regulation of the vesicular transport within cells (8,9,150). Several studies performed already in the 1980s describe an effect of increases in the $[K^+]_{ex}$ to trigger especially exocytosis, i.e. neurotransmitter and hormone release, in a concentration and time dependent manner (**Figure 6**) (8,150). The involvement of Kv channels in exocytosis was identified quite recently (151). Thus, Kv 2.1 for example, abundantly expressed in neurons and neuroendocrine cells, interacts with syntaxin and SNAP25 in several cell types as well as *in vitro*, enhancing neurotransmitter and hormone release (**Figure 6**) (151).

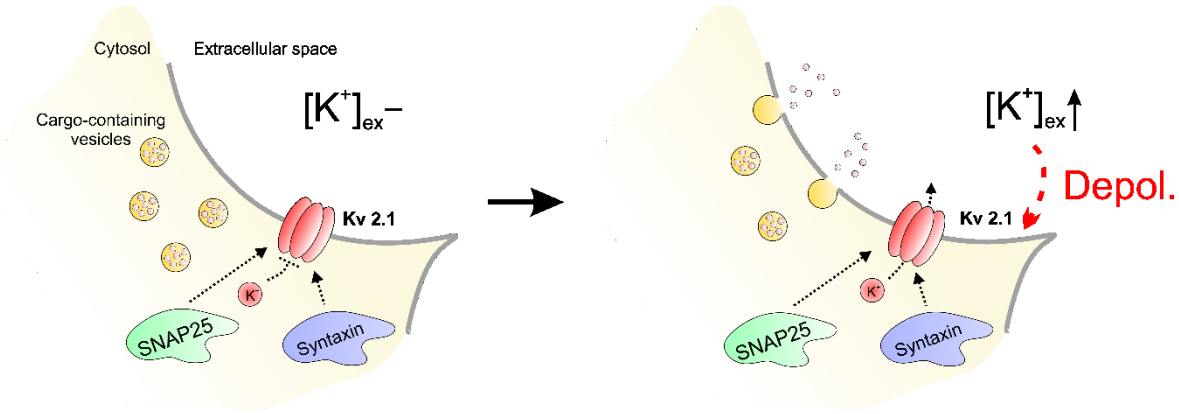

Figure 6: Stimulatory effect of $[K^+]_{ex}$ on neurotransmitter and hormone release of neuroendocrine cells. Schematic representation of a neuroendocrine cell with its plasma membrane (grey line) and cargo-containing vesicles (yellow circles with cargo shown as light pink granules). Extracellular space and cytosol are indicated (left panel). Kv 2.1 (red channel, both panels) is expressed in these cells and frequent interaction partners of Kv 2.1 such as SNAP25 (light green) and syntaxin (light blue) are demonstrated. At low $[K^+]_{ex}$, Kv 2.1 remains closed due to the negative membrane potential, thus Kv 2.1 is impermeable for K^+ (red circle, left panel). Increases of $[K^+]_{ex}$ depolarizes the cell, Kv 2.1 opens, leading to K^+ fluxes across the plasma membrane, further causing exocytosis and secretion of cargo-containing vesicles (right panel). Figure according to Ceccarelli et al., 1988, Grohovaz et al., 1989 and Singer-Lahat et al., 2007 (8,150,151).

Vice versa, the uptake of metabolites or macromolecules, a process referred to as endocytosis, is known to be directly affected by K^+ (9). This fact becomes evident, as K^+ depletion of fibroblasts results in a drastically reduced receptor mediated internalization of low density lipoprotein (LDL) and decreased coated pit formation within the cells (9). Interestingly, the exposure of cells to hypotonic solutions, causing a K^+ efflux from cells, results in similar effects of minimized internalization (152).

1.2.4 Enzymatic activities and K^+

Many intracellular enzymes use di- or polyvalent metal ions as a cofactor to fulfill their function (153,154). However, the fact that there are also enzymes depending on monovalent cations such as K^+ was first described in 1953 by Kachmar and Boyer, who identified the presence of K^+ as an essential requirement for the activity of the pyruvate kinase (155). Today, many other studies demonstrating the importance of monovalent cations such as Na^+ and K^+ as cofactors for enzymes are available (12,156–158).

Typically, enzymes requiring monovalent cations as cofactors are separated into two groups, type I and type II enzymes (**Figure 7**) (159). Type I enzymes are proteins requiring K^+ as a cofactor for reaction catalysis, as K^+ is directly involved in the binding of the substrate (**Figure 7a**) (159). Simple examples of such type I enzymes depending on K^+ are the pyruvate kinase (11,155) as well as the diol- (160) and glycerol dehydratase (161). Very often, enzymes involved in phosphoryl transfer reactions are associated with their dependency on the magnesium (Mg^{2+}) or manganese (Mn^{2+}) cation (159). However, usually a full activation of these enzymes requires also the presence of K^+ (159). Mg^{2+} and K^+ can act cooperatively to allow an optimal binding of the phosphate component of a molecule into the catalytic site of a protein (159).

In comparison to type I enzymes, type II enzymes do not directly need K^+ for binding their substrate. K^+ rather changes the conformation of the active site to be accessible for the substrate (**Figure 7b**) (159). A typical example is the ribokinase, an enzyme catalyzing the phosphorylation of ribose using Mg^{2+} and ATP with the absolute need for K^+ (162). Interestingly, the enzyme can also use cesium (Cs^+) as cofactor, having a similar size and charge as K^+, but not at all Na^+, highlighting the ion specificity and importance of K^+ for the enzyme (159,162). Some of many examples of such type II enzymes are the amino-imidazole riboside kinase (12), pyruvate dehydrogenase kinase (13) or the serine dehydratase (159,163). Altogether, these data demonstrate the important role of K^+ for the maintenance of a physiological cellular metabolism, as K^+ is directly involved in the regulation of enzymatic activities. This important attribute of K^+ becomes even more evident considering its involvement in tumor progression.

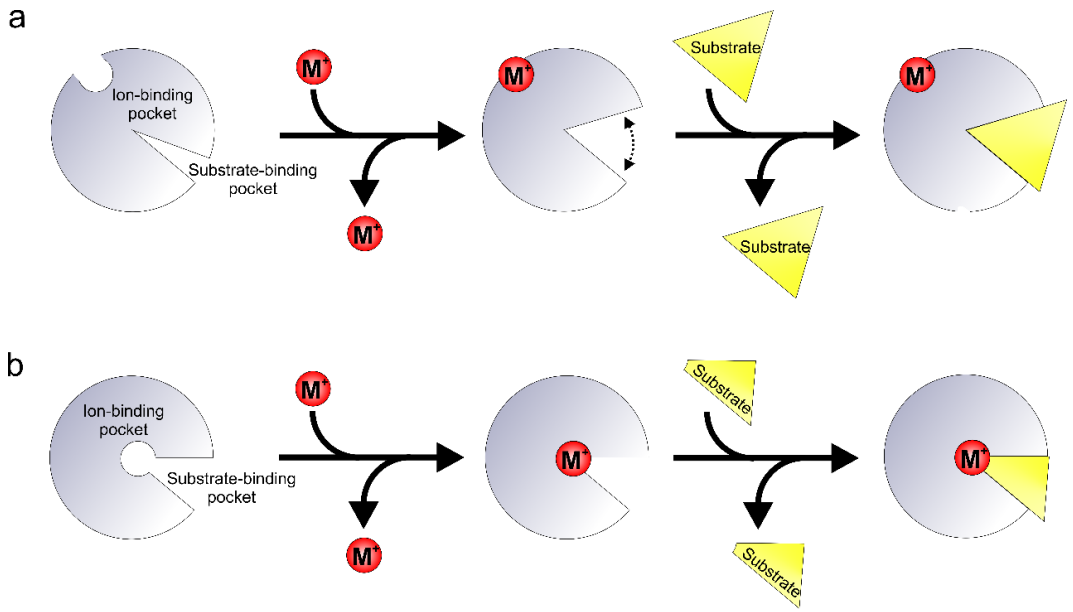

Figure 7: Schematic demonstration of monovalent cation (M^+) dependent enzymes and the role of M^+ for substrate binding in type I and type II enzymes. M^+ dependent enzymes are represented in grey (**a** and **b**) with a schematic demonstration of the enzymes ion- and substrate binding pocket. (**a**) Schematic representation of a M^+ dependent type I enzyme. Upon binding of M^+ (red circles) the enzyme undergoes a conformational change (middle panel) making the substrate-binding pocket of the enzyme accessible for the substrate (yellow triangle, right panel). (**b**) In comparison to M^+ dependent type I enzymes (**a**), M^+ in type II enzymes (**b**) is not altering the enzymes conformation (middle panel), but is directly involved in substrate binding (right panel). Figure according to Gohara et al., 2016 (159).

A recent study demonstrated that within the tumor microenvironment, an area of increased necrotic cell death, $[K^+]_{ex}$ are significantly elevated (**Figure 8a**) (15). This increased $[K^+]$ leads to facilitated K^+ uptake of cells, for example of tumor infiltrating effector T-cells (**Figure 8a**) (15), which are supposed to eliminate cells showing cancerous alterations (164). Usually these cells activate their T-cell receptor (TCR), a transmembrane heterodimer important for the recognition of a foreign antigen, which is bound to the major histocompatibility complex (MHC) I or II (**Figure 8**) (165). The activation of the TCR requires a highly regulated signal transduction process, involving cluster of differentiation (CD) 4 and CD8 (166), where CD8 is stabilizing the interaction between MHC II or MHC I and TCR (166). However, it has been demonstrated that within the tumor microenvironment, T-cells suffer an impaired activation of the Akt-mTOR signaling (**Figure 8a**) (15). This suppression was directly linked to increased $[K^+]_i$, as the normalization of $[K^+]_i$ via gramicidin, a K^+ specific pore, or expression of the potassium channel Kv 1.3 reconstituted Akt-mTOR activation (**Figure 8b**). The suppression of the Akt-mTOR signaling within T-cells was linked to enhanced activity of phosphatases (15), however, a direct evidence for the regulation of intracellular phosphatases by K^+ is, although conceivable, missing (**Figure 8a**).

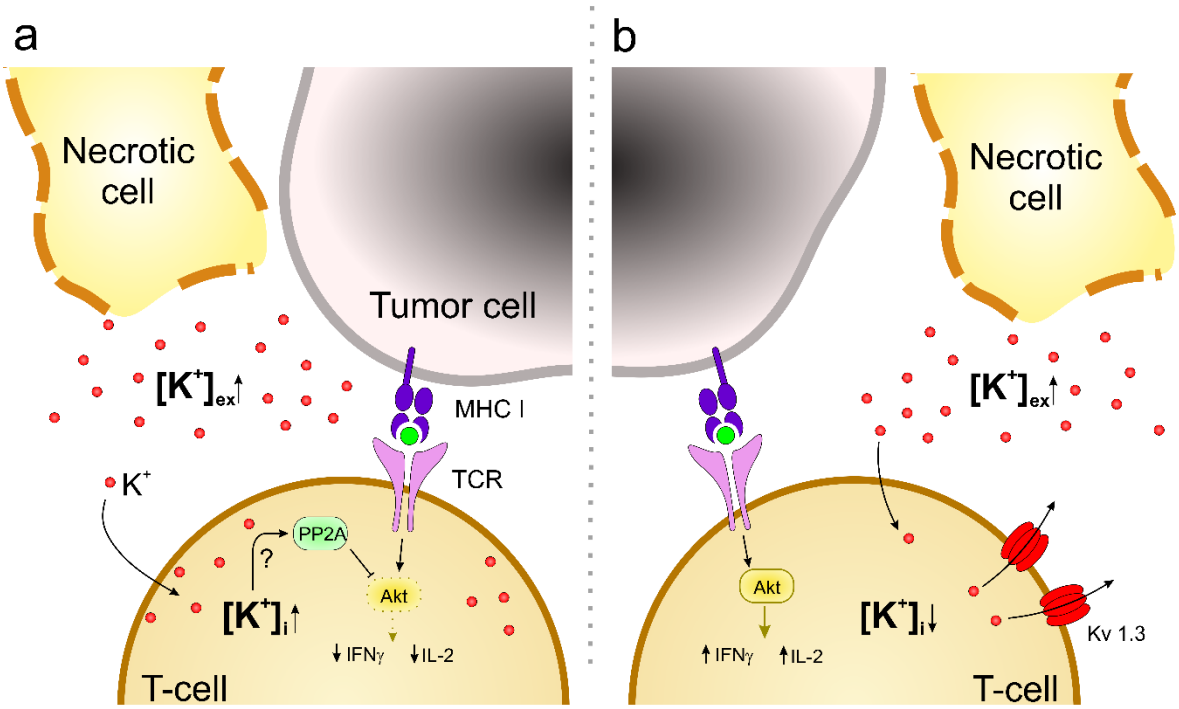

Figure 8: Schematic representation of K^+ mediated T-cell immunosuppression and effects of Kv 1.3 expression on T-cell function. Within the tumor microenvironment necrotic tumor cells release high [K^+] into the extracellular space, leading to increased $[K^+]_{ex}$. Tumor-infiltrating T-cells thereby migrate into the environment with elevated $[K^+]_{ex}$, leading to increases in $[K^+]_i$ within these T-cells. While tumor cells represent antigen (green circle) bound to MHC I (violet) to the T-cell receptor (TCR, pink), the intracellular signaling cascade in these T-cells is altered. (**a**) The effect might directly be caused by increased $[K^+]_i$, affecting protein phosphatase 2A (PP2A), leading to decreased phosphorylation of Akt (yellow) and furthermore reduced production of interferon γ (IFNγ) and interleukin-2 (IL-2). (**b**) Expression of Kv 1.3 (red channels) in these cells leads to decreased $[K^+]_i$, restores the phosphorylation of Akt and increases INFγ and IL2 production. Figure according to Eil et al., 2016 (15) and reproduced from Gurusamy et al., 2017 with permissions from publisher American Association for Cancer Research (167).

1.2.5 K^+ and apoptosis

The term apoptosis describes a controlled mechanism leading to the programmed death of a cell (168). Already studies in the 1950s observed a distinctly different mode of cellular death than necrosis, showing ultrastructural features suggesting a controlled mode of death (169). However, until then, mainly necrosis, the cell death caused by noxious stimuli leading to irreversible damage of the cell, was described (170). In 1972, Kerr, Wyllie and Currie perceived the importance of a programmed cell death and referred to it as apoptosis (171), a controlled cell death being important in physiology as well as pathology (172).

As the maintenance of the electrochemical K^+ gradient across the plasma membrane requires a functional Na^+/K^+ ATPase (1,23), however, apoptosis is

associated with dysfunctions of the exchanger (173), intracellular K^+ levels are continuously decreasing (174). The fact that K^+ is fundamentally involved in the regulation of apoptosis through the modulation of enzyme function was excessively investigated during the 90s (174–177). Key regulator enzymes of apoptosis include caspases degrading proteins, and nucleases that degrade DNA (**Figure 9**) (178,179). These enzymes fulfill their function in a K^+ dependent manner. Thus, a decrease in $[K^+]_i$ is a key event during the programmed cell death, as physiological $[K^+]_i$ levels of ~ 140 mM fully suppress the apoptotic cascade (**Figure 9a**) (180,181). Nonetheless, these enzymes become active with an intracellular K^+ depletion, initiating apoptosis (**Figure 9b**) (180,181). These results become more significant as keeping the cells in high $[K^+]_{ex}$ after an apoptotic stimulus prevents cells from dying via the programmed cell death (182). However, whether the $[K^+]_i$ drop is an initiator or a consequence of apoptosis remains elusive, but the effect is probably universal (183).

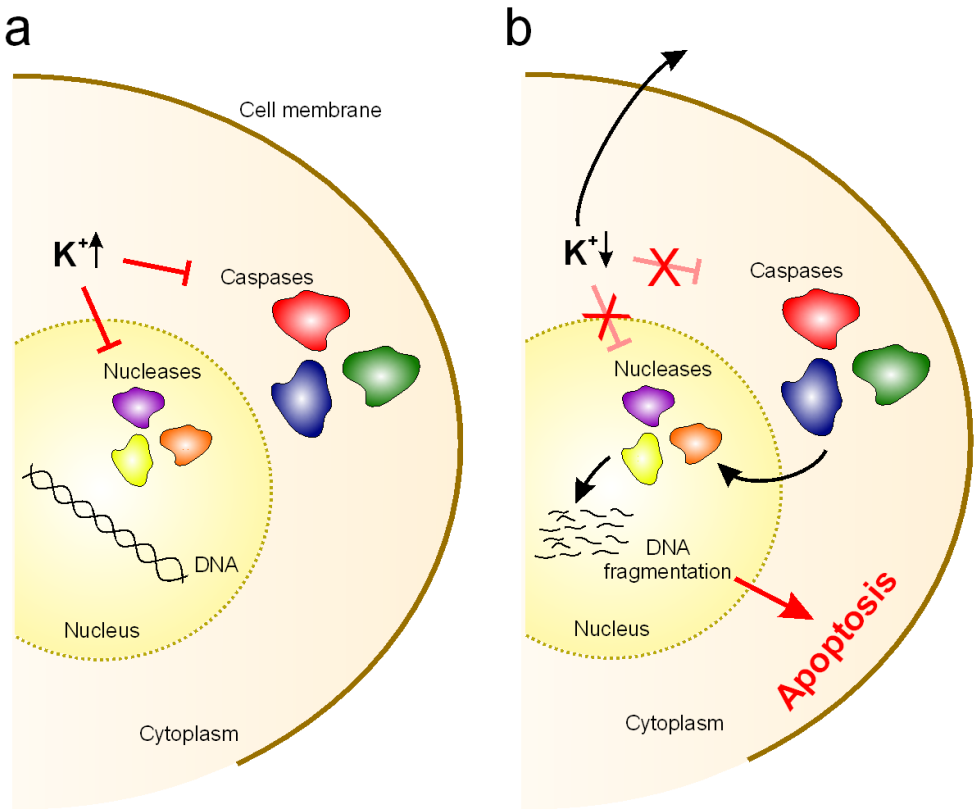

Figure 9: Effects of $[K^+]_i$ on apoptotic pathways. Schematic representation of a cell with its cytoplasm (light brown), nucleus (yellow) and the plasma membrane (dark brown). Caspases (red, blue and green), nucleases (violet, yellow and orange) and DNA (black double helix) are represented. (**a**) Under physiological conditions with high $[K^+]_i$, K^+ inhibits caspase- (red, blue and green) and nuclease activity (violet, yellow and orange), thus preventing the induction of apoptosis and avoiding DNA fragmentation. (**b**) The inhibition of caspase and nuclease activity is abrogated upon loss of the intracellular K^+ gradient, leading to caspase- and nuclease activation, DNA fragmentation and finally apoptosis of the cell.

1.2.6 K^+ and cancer

Typically, carcinogenic compounds decrease $[K^+]_i$ while increasing the intracellular Na^+ concentration ($[Na^+]_i$), while anti-carcinogenic compounds have the opposite effect (184). Some examples of such carcinogenic compounds reversing the intracellular ion composition are for example cadmium (185), fat (186) or alcohol (187). Anti-carcinogenic agents such as vitamin C (188) and D (184), selenium (189) and indomethacin (190) have the opposite effect of elevating $[K^+]_i$. Interestingly, similar effects of decreasing global $[K^+]$ can be observed in stress (191) or diseases such as alcoholism (192), which come along with increased cancer rates (193,194).

In addition to the direct influence of (anti)carcinogenic compounds on the intracellular ion composition, cancer is very often associated with alternations in the K^+ channel expression pattern (195). Thus, breast, colon or prostate cancers are commonly associated with an overexpression of Kv 1.3 (195). Some cancer types, especially adrenal cancers are correlated with recurring somatic mutations of Kir 3.4 (196). These mutations and different channel expression patterns not only promote cancer development, but might be an important hallmark for cancer malignancy (195). Expression level of the G-protein-activated inwardly rectifying K^+ channel (GIRK1), for example in breast cancer cells, correlates with the degree of lymph node metastases (197).

All these examples demonstrate the importance of an intact intracellular K^+ homeostasis for the maintenance of cellular physiology, as imbalances can promote cancer development (195).

1.3 Fluorescent proteins and their usage for the design of genetically encoded biosensors

1.3.1 Discovery of fluorescent proteins and their engineering

In 1955, Davenport and Nichol discovered proteins that possess the ability to fluoresce, when they were experimenting with diverse hydromedusae (198). However, the first isolation of a so-called green fluorescent protein (GFP) was achieved several years later in 1962 from the jellyfish *Aequorea victoria* (199). From a structural point of view, a fluorescent protein (FP) consists of 11 antiparallel β-strands arranged in a so-called β-barrel structure (**Figure 10**) (200).

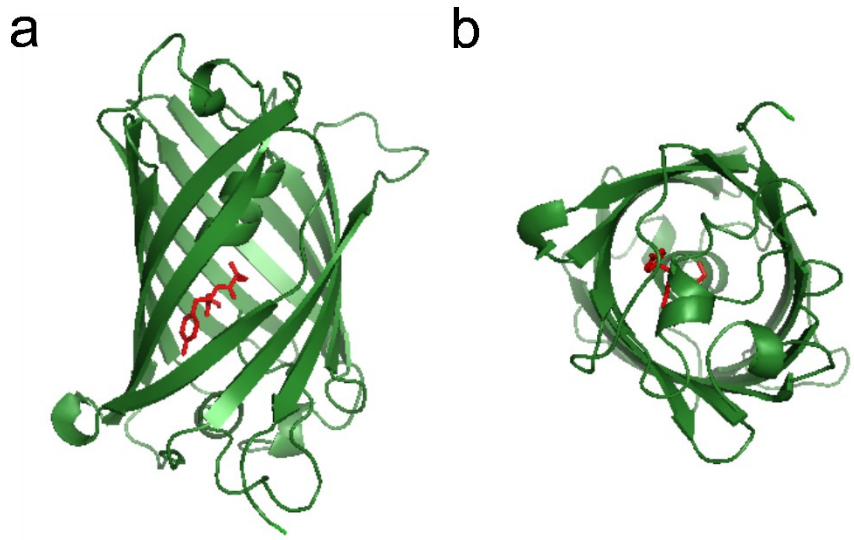

Figure 10: Structure of wild type green fluorescent protein. Front (**a**) and bottom view (**b**) of wild type green fluorescent protein isolated from *Aequorea victoria.* Chromophore composed of the amino acids serine-tyrosine-glycine (SYG) is visualized in red. 3D-structures of the protein were predicted using the Phyre2 online prediction tool and illustrated using PyMol Viewer.

In principal, specific amino acids within the FPs, referred to as chromophore, are responsible for their ability of fluorescence (**Figure 10**). Interestingly, a FP is not directly fluorescent after its synthesis, but requires several minutes for its maturation. This process known as chromophore maturation requires, however, no cofactors instead of molecular oxygen (O_2) (201). The advantageous features of FPs led already some while after their discovery to the use of GFP for the visualization of gene expression (202) or the identification of protein localizations (203) in single living cells. Further homologous proteins of GFP have been identified in marine animals, thus, for example a red fluorescent protein expressed in the coral *Discosoma* (204).

Nowadays, countless homologous variants of this GFP evolved via mutations of the original variant, covering the whole visible spectra including the UV- and infrared-area (205). These FPs referred to as UV-, blue-, cyan-, yellow-, orange-, red and far-red fluorescent proteins (UVFPs, BFPs, CFPs, YFPs, OFPs, RPFs and fRFPs) feature highly variable properties concerning their excitation- and emission spectra, brightness, photo- and pH-stability and chromophore maturation time (205).

1.3.2 Usage of fluorescent proteins for the design of genetically encoded FRET-based probes

The fact that these FPs are not only a valuable tool for the visualization of gene expression and investigation of protein localizations within cells, but are also suitable for the design of so-called genetically encoded probes (GEPs) was recognized many years after their isolation in 1962 (199). The first development of a GEP succeeded in 1997 by Miyawaki et al., who exploited Förster resonance energy transfer (FRET) occurring between two FP variants, CFP and YFP, for the design of genetically encoded Ca^{2+} indicators (206). By fusing calmodulin (CaM), a Ca^{2+} binding protein (207) and the myosin light chain kinase M13, a protein interacting with Ca^{2+} bound CaM (208), with an N-terminal CFP and a C-terminal YFP, they yielded functional Ca^{2+} indicators (206). In the absence of Ca^{2+}, FRET-efficiency between CFP and YFP is low, while the binding of Ca^{2+} to CaM triggers a conformational change of the probe, yielding increased FRET-fluorescence, i.e. decreased CFP fluorescence (**Figure 11a**) (206). According to the feature of these indicators to be protein-based, they can also be introduced into cellular organelles by fusing localization specific peptides or domains to the N- or C- terminus, respectively (206).

In addition to these CFP/YFP based FRET-probes (**Figure 11a**), red shifted variants using GFPs as donor and RFPs as acceptor have been developed (209). These probes feature some advantages over their CFP/YFP based ancestors, including reduced photo-toxicity due to longer excitation wavelengths and facilitated combination with second indicators, thus allowing simultaneous measurements within single cells (209). Having recognized the possibility of generating such GEPs by the usage of FP-based FRET-pairs soon led to the development of a huge variety of other sensors (210–213).

Although the requirements for the design of novel probes are rather simple, the major difficulty represents the identification of appropriate ion-, metabolite- or cell signaling event specific domains. In case of FRET-based GEPs these domains usually undergo conformational changes in response to association or dissociation of the ligand, increasing FRET, thereby decreasing donor fluorescence (**Figure 11a**) (214). Additionally, proteins used within GEPs should not interfere with cell signaling pathways and should not show toxic effects upon expression in mammalian systems. However, several suitable domains fulfilling all these requirements have already been identified and used for the generation of FRET-based probes (**Figure 11a**). Nowadays a huge variety of these GEPs is available for the visualization of diverse intracellular metabolites and ions. Only some of many examples are sensors sensitive for Ca^{2+} (206,209), ATP (210), ATP/ADP ratio (215), pyruvate (211), Cl^- (216) or Mg^{2+} (212).

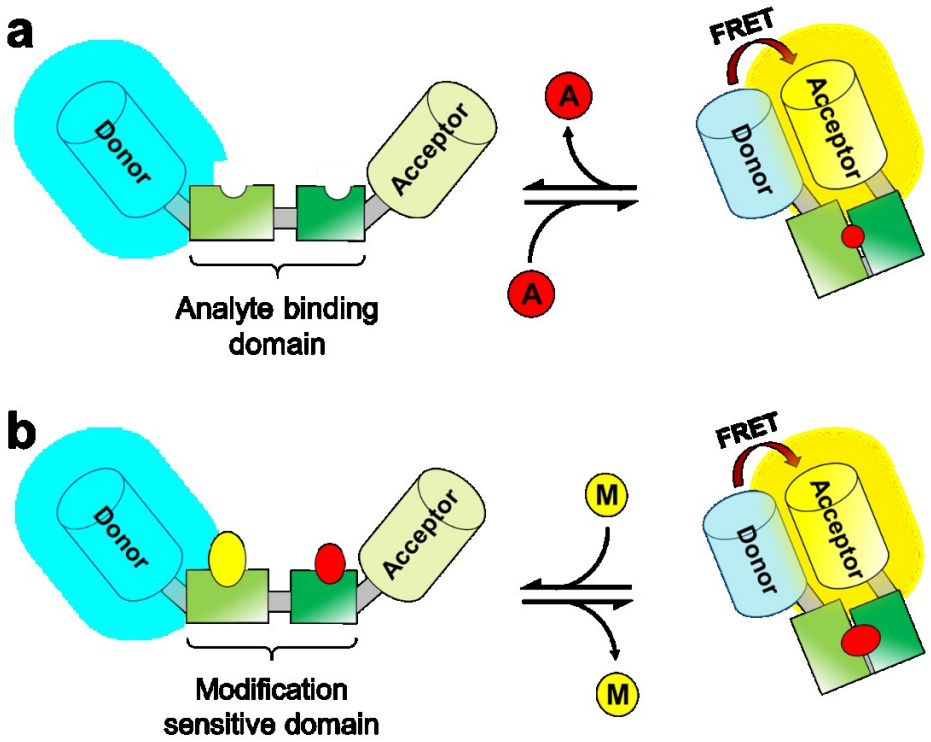

Figure 11: Functional principle of genetically encoded FRET-based probes. (**a**) Schematic illustration of an analyte binding, genetically encoded, FRET-based indicator. The analyte binding domain is located within two FPs, referred to as FRET-donor (donor) and FRET-acceptor (acceptor). In the analyte unbound conformation, the two FPs are distant from each other, yielding high donor and low acceptor fluorescence (left panel). Upon analyte binding (A, red circle) to an analyte binding domain the probe undergoes a conformational rearrangement, yielding increased FRET- and decreased donor fluorescence. (**b**) Schematic representation of a modification sensitive FRET-based indicator. A modification sensitive domain is located between the FRET-donor (donor) and the FRET-acceptor (acceptor). FRET-acceptor fluorescence is low in the unmodified conformation (left panel). Upon (de)modification of the modification sensitive domain, the probe undergoes a conformational rearrangement, yielding high FRET- and decreased donor fluorescence (right panel). Figure adapted from Bischof et al., 2017, with permissions from the publisher Nature Communications (217).

Also FRET-based probes for the visualization of kinase activities in single living cells have been developed, including Akt, AMPK, ERK, FAK, MAPK, mTOR, Src, and many more (218). These probes mainly rely on a chemical modification which then alters the conformation of the probe, and thus, FRET-efficiency (**Figure 11b**) (218).

Nevertheless, besides FRET-probes depending on a conformational rearrangement, other principles have been described, including protein-protein interactions linked to a FRET-based read-out (219), or indirectly using a combination of pH sensitive and stable FPs as FRET-donors and -acceptors (220). These FRET-based sensors are suitable for the visualization of highly dynamic processes within cells, including visualizations protein-protein interactions (219) or autophagy and pH transitions within intracellular vesicles (220).

1.3.3 Usage of fluorescent proteins for the design of genetically encoded single FP-based probes

Quite recently, besides these FRET-based indicators, also probes consisting of only one fluorescent protein have been developed (**Figure 12**) (221–223). According to their design, these indicators are also referred to as single FP-based probes. Mostly, these tools consist of circularly permuted FPs (cpFPs) fused to specific analyte-binding domains (**Figure 12**) (223,224). The most famous examples for these kind of indicators represent the genetically encoded Ca^{2+} indicators for optical imaging (GECOs) (224,225), the genetically encoded nitric oxide probes (geNOps) (222), and the quantitative evaluators of cellular energy (QUEENs) (221).

The major advantage of such single FP-based probes, in comparison to FRET-based probes, are their narrow spectral properties (222,224,225). They often only have one excitation maximum, with one or two emission wavelengths, allowing an intensiometric (**Figure 12a**), or even ratiometric read-out (**Figure 12b** and **12c**). However, their principle of function can be very diverse, as upon analyte binding to the analyte specific domain fused to the FP, either their emission intensity is altered (**Figure 12a**) (222,224,225), their emission wavelength is shifted to another maximum (**Figure 12b**) (224), or their excitation maximum is shifted at a constant emission wavelength (**Figure 12c**) upon analyte binding (221,223).

As these indicators are also protein-based, they can be fused to localization specific peptides for their targeting to specific (sub)cellular localizations (222,224). According to their features, the probes can rather easily be combined to perform multi-color and/or multi-parameter imaging of various analytes in different cellular compartments on the single cell level (222,224,225).

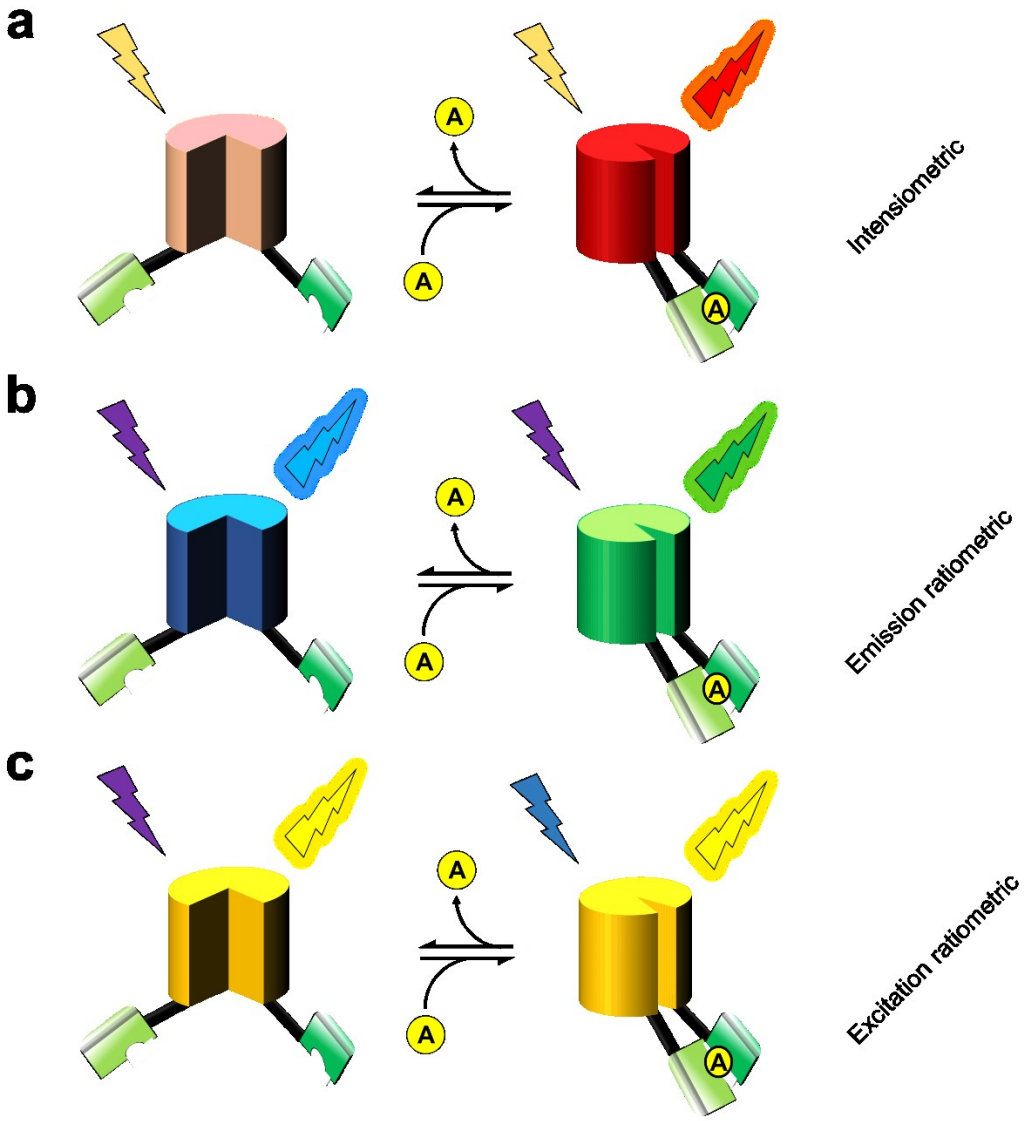

Figure 12: Functional principle of genetically encoded single FP-based probes. Schemata represent illustrations of genetically encoded, single FP-based probes. Mostly, these probes consist of circularly permuted FPs (cpFPs) fused to analyte specific binding domains (light and dark geen) on both, the N- and C-terminus, respectively. These sensors can either function in an (**a**) intensiometric manner, having one emission being low (left panel) or high (right panel) depending on the analyte (A, yellow circles) concentration, or in an (**b**) emission ratiometric manner, altering their emission maximum upon analyte binding (left and right panel). Their excitation maximum can also be shifted (**c**), depending on the unbound (left panel) or bound conformation of the sensor (right panel), yielding excitation ratiometric probes. cpFP colours are chosen randomly and are not restricted to the respective class of sensor. Blizzards represent excitations and emissions, respectively. Figure according to Nagai et al., 2001, Zhao et al. 2011, Wu et al., 2013 and Yaginuma et al., 2015 (219,221–223).

1.4 *E.coli* Kbp as a specific K^+ binding protein

In 2016, Ashraf et al. identified Kbp (K^+ binding protein), a protein formerly called YgaU with unknown function, as a K^+ binding protein in *E.coli* (**Figure 13**) (226). The protein with a size of around 16-kDa consists of an N-terminal bacterial OsmY and nodulation (BON) domain and a C-terminal lysine motif (LysM) (226). BON domains are predicted to be membrane-associated phospholipid binding domains (227), however, experimental evidences supporting this conclusion are controversial (226–229), while the function of LysM domains has been well characterized earlier (226,230). Frequently, these LysM domains are associated with peptidoglycan binding (231) and increased expression levels of Kbp modulate peptidoglycan crosslinking (231,232). It has been demonstrated that the expression level of Kbp (YgaU) is increased upon exposure of *E.coli* to osmotic stress, as it is part of the RNA polymerase sigma S (RpoS) regulon (233), encoding the sigma factor-38 (234). In principal, RpoS represents a central regulator of the general stress response in *E.coli*, thereby acting proactive, allowing the cell to survive environmental challenges, and retroactive, preparing cells for sequential stress (235). However, Ashraf et al. demonstrated in their work that cytoplasmic expression of Kbp is required for normal growth of *E.coli* at $[K^+]_{ex}$ above 1 mM, as well as under conditions of salt-induced osmotic stress (226). Structural analysis showed that one protein of Kbp binds one K^+ with an equilibrium dissociation constant (K_D) of 161 µM ± 8 µM, thereby undergoing a huge conformational rearrangement (**Figure 13**) (226).

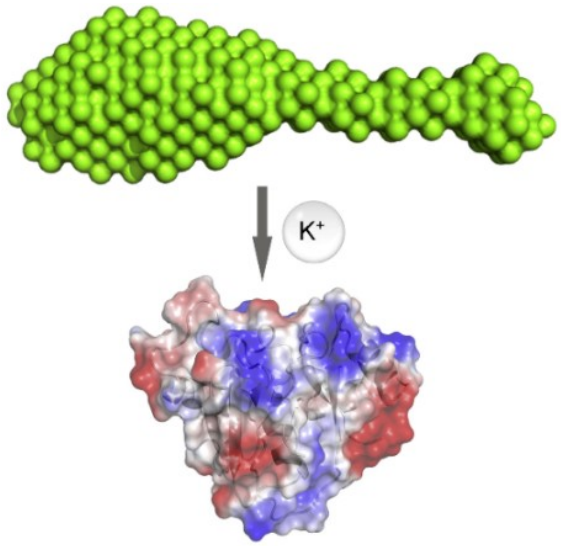

Figure 13: Schematic illustration of apo-Kbp and Kbp-K^+. Panels demonstrate schematic surface models of apo-Kbp (upper panel, K^+ unbound) and Kbp-K^+ (lower panel, K^+ bound). Lower panel is color coded according to the electrostatic potential (red=negative potential, white=neutral potential and blue=positive potential). Reproduced from Ashraf et al., 2016, with permissions from publisher Structure (226).

In principal, the BON domain represents the K^+ binding pocket, while the LysM domain flips and interacts with the BON domain upon K^+ fixation, stabilizing the complex (**Figure 13**) (226). The protein is thereby highly specific for K^+ over Na^+, probably due to the smaller size of Na^+, while Kbp was binding rubidium ions (Rb^+) (K_D=225 µM ± 8 µM), Cs^+ (K_D~ 2000 µM) and ammonium ions (NH_4^+) (K_D~ 1000 µM), all having a similar size and charge as K^+, however, with lower affinity (226).

2 Aims and Objectives

Considering the importance of an intact cellular and global K^+ homeostasis within organisms, we aimed to broaden the spectrum of available K^+ indicators. Several chemical, K^+ sensitive probes have been developed recently, however, due to their restrictions in applications we aim

1) To develop genetically encoded, FP-based sensors, meeting all criteria of state-of-the-art FP-based FRET-biosensors, including:
    i. Selectivity for K^+ over other ions, especially Na^+
    ii. Reversible association and dissociation of K^+
    iii. Thermo-stability of K^+ binding to allow *in vivo* measurements
    iv. Non-toxic upon expression in mammalian systems
    v. Appropriate K_D of the probe to allow extra- or intracellular K^+ measurements

The development of such K^+ sensitive probes may feature some advantages over conventional ion-selective electrodes (ISE), especially when applied for research diagnostics in small laboratory animals. Frequently, mice need to be sacrificed for the determination of plasma- or serum $[K^+]$, due to the required sample volumes for ISE instruments, while determinations of urine $[K^+]$ are totally unfeasible with most devices. Thus we aim

2) To apply these K^+ sensitive probes for the determination of $[K^+]$ within biological samples, which may represent a high throughput alternative for conventional ISE-based $[K^+]$ measurements

The development of FP-based probes allowing such measurements may allow the repetitive sample collection of one animal over time, due to smaller sample volumes required for the measurements.

In addition, vital cells maintain a steep K^+ gradient across their plasma membrane. Therefore, we aim

3) To apply these genetically encoded sensors sensitive for K^+ for the visualization of cell death or cell growth.

Most cell viability assays represent end-point measurements, while the analysis of [K^+] within the supernatant of cells may allow the online-visualization of cell viability and growth of one given population of cells over time.

Besides the application of the recombinant sensor protein *in vitro*, we aim

4) To apply the K^+ sensitive probes *in vivo* for the measurement of extracellular K^+ dynamics in living animals.

Having characterized and applied the recombinant, purified protein of these probes, we further aim

5) To perform the characterization of the sensors upon expression in mammalian cells, considering especially the parameters of
    i. Ion selectivity and
    ii. K^+ sensitivity *in situ*

Characterization of the probes upon expression in mammalian cells will uncover whether the measurement of K^+ fluctuations in single living cells is feasible. Besides the untargeted expression within cells we aim to

6) Target the genetically encoded K^+ indicators to subcellular localizations including
    i. Cytosol
    ii. Nucleus
    iii. Mitochondria and
    iv. Subplasmalemmal area for

7) The quantification of subcellular [K^+] within single living cells.

Finally, applying these genetically encoded sensors within excitable cells will allow

8) The visualization and correlation of (sub-)cellular K^+ and Ca^{2+} fluctuations upon cell stimulation.

3 Material and Methods

The text of the methods section is partially based on the concise description of the methods in Bischof et al., 2017 (217).

3.1 Chemicals and buffer solutions

Materials used for cell culture were purchased from PAA laboratories (Pasching, Austria). Restriction enzymes and chemically competent 10-beta *E.coli* cells were obtained from New England Biolabs (New England, GB). Agar-Agar Kobe I, $CaCl_2$, CsCl, D-glucose, EGTA, HEPES, KCl, $MgCl_2$, NaCl, NaOH, NH_3 (32 %), RbCl, Triton X-100, Tryptone/Peptone and Yeast extract were purchased from Carl Roth (Graz, Austria). Agarose was obtained from VWR International (Vienna, Austria). 1,2-Bis(2-aminophenoxy)ethane-N,N,N′,N′-tetraacetic acid tetrakis acetoxymethyl ester (BAPTA-AM), 2-deoxy-D-glucose (2-DG), digitonin, gramicidin, monensin, nifedipine, N-Methyl-D-glucamin (NMDG), oligomycin A, ouabain, tetraethylammonium chloride and valinomycin were obtained from Sigma Aldrich (Vienna, Austria). Bacterial protease inhibitor cocktail containing AEBSF, E-64, bestatin, EDTA and pepstatin were purchased from Amresco (Cleveland, US).

Bacterial cultivation was performed using Luria-Bertani (LB) medium. 1 L of medium was prepared using 10 g NaCl, 10 g trypton/pepton and 5 g yeast extract followed by autoclaving (Autoclave type 17, MELAG, Berlin, Germany).

Buffers used for the purification of recombinant GEPIIs were composed of the following: Lysis buffer contained 100 mM Na_2HPO_4, 200mM NaCl, 10mM imidazole, 250 units of benzonase nuclease and bacterial protease inhibitor cocktail, pH=8.0. Washing buffer contained 100 mM Na_2HPO_4, 200 mM NaCl, 40 mM imidazole, pH adjusted to 8.0. Purification buffer was composed of 100 mM Na_2HPO_4, 200 mM NaCl, 200 mM imidazole, pH adjusted to 8.0. Buffer used to elute the protein (Elution buffer) was composed of 10 mM HEPES, with or without 0.05% Triton X-100 and pH was adjusted to 7.3 using NMDG.

Buffers used to determine the EC_{50} values of GEPIIs *in vitro* were composed of the following: Elution buffer, with or without 0.006, 0.02, 0.06, 0.2, 0.6, 2, 6, 20, 60, 200, 600, 2000 or 4000 mM KCl. Buffers used to generate the calibration curve consisted of Elution buffer with or without (in µM): 200, 300, 400, 500, 600 or 700 KCl. Selectivity of GEPIIs *in vitro* was determined using Elution buffers containing 0.02,

0.06, 0.2, 0.6, 2, 6, 20, 60, 200, 600, 2000 or 4000 mM $CaCl_2$, CsCl, NaCl, NH_4^+ or RbCl, pH adjusted to 7.3 with NMDG and HCl (Carl Roth, Graz, Austria)

The buffers used for the EC_{50} determination of GEPIIs *in situ* were composed of the following substances (in mM): 140 NMDG, 10 HEPES pH adjusted to 7.4 with HCl (K^+ free buffer) or contained 100 KCl, 40 NMDG, 10 HEPES, pH adjusted to 7.4 with HCl (100 mM K^+ buffer). To additionally obtain buffers containing (in mM): 0.01 K^+, 0.03 K^+, 0.1 K^+, 0.3 K^+, 1 K^+, 3 K^+, 10 K^+, 30 K^+, K^+ free and 100 mM K^+ buffers were mixed in appropriate portions. To receive a buffer containing 300 mM K^+, 300 mM KCl, 10 mM HEPES with pH adjusted to 7.4 using NMDG was prepared.

Hemoglobin determination in murine sera was performed using drabkin's solution composed of 77 µM KCn, 607 µM $K_3[Fe(CN)_6]$, 12 mM $NaHCO_3$ and 0.01% triton X-100.

Assay buffer used for cell viability experiments was composed of (in mM): 143 NaCl, 2 $CaCl_2$, 1 MgCl2, 10 HEPES either with 10 D-glucose or 10 2-DG.

Prior to fluorescence microscopy experiments, cells were washed and stored for 30 min in a HEPES-buffered solution (storage buffer) containing 138 mM NaCl, 5 mM KCl, 2 mM $CaCl_2$, 1 mM $MgCl_2$, 10 mM HEPES, 2.6 mM $NaHCO_3$, 0.44 mM KH_2PO_4, 0.34 mM Na_2HPO_4, 10 mM D-glucose, 0.1% vitamins, 0.2% essential amino acids and 1% penicillin–streptomycin, pH adjusted to 7.4 with NaOH.

For physiological fluorescence microscopic measurements of cells, cells were perfused in a physiological buffer containing in mM: 138 NaCl, 5 KCl, 1 $MgCl_2$, 10 D-glucose and 10 HEPES, either with 2 $CaCl_2$ (Ca^{2+} buffer) or 1 EGTA (Ca^{2+} free buffer). Inhibitory effects on INS-1 cell depolarization of nifedipine and tetraethylammonium were checked using 100 µM nifedipine or 15 mM tetraethylammonium chloride.

Depolarization buffer used to depolarize INS-1 cells was composed of (in mM): 73 NaCl, 70 KCl, 1 mM $MgCl_2$, 10 D-glucose and 1 HEPES, either with 2 $CaCl_2$ (Depolarizing Ca^{2+} buffer) with or without 15 tetraethylammonium or 0.1 nifedipine or contained 1 EGTA (Depolarizing Ca^{2+} free buffer).

Nominally Ca^{2+} free buffer used for BAPTA-AM loading contained (in mM): 138 NaCl, 5 KCl, 1 $MgCl_2$, 10 D-glucose and 10 HEPES.

3.2 Cloning of GEPIIs

Cloning was performed according to conventional restriction digestion based procedures and all products were verified by sequencing (Eurofins Genomics, Germany). Genomic DNA of *E.coli* 10-beta served as PCR template to isolate the Kbp from bacterial cells. Therefore, the following primers, also found in **Table 1**, were used: Kbp fwd that adds a ClaI restriction site at the 5' end and Kbp rev adding an EcoRI restriction site at the 3' end of wild type Kbp. To receive functional GEPIIs, wild type Kbp was fused to the fluorescent protein variants mseCFP, a cyan fluorescent protein at its N-terminal end and the circularly permuted Venus (cpV), a yellow fluorescent protein variant, at its C-terminal end via ClaI and EcoRI in the mammalian expression vector pcDNA3.1(-) (Thermo Fisher Scientific, Austria) to receive GEPII 1.0. For the construction of the K^+ insensitive probe lc-BON GEPII 1.0, several acidic amino acids within the BON domain of Kbp (E32Q, D41N, D43N, D51N, D59N, E64Q, E67Q, D83N and D84N) were mutated, respectively. The single nucleotide exchanges to receive lc-BON GEPII 1.0 were performed by a 5-step overhang PCR, sequentially using the following primers in the given order: lc-BON 01 fwd, lc-BON 02 fwd, lc-BON 03 fwd, lc-BON 04 fwd, and lc-BON 05 fwd, all in combination with Kbp rev primer resulting in ClaI and an EcoRI restriction sites at the terminal ends. To generate the low sensitive K^+ probe lc-LysM GEPII 1.0 all acidic amino acids within the LysM domain of wild type Kbp comprising D104N, E125Q and D135N were exchanged by their respective amides. Mutations were inserted into wild type Kbp by a 2-step overhang PCR using lc-LysM 01 fwd and lc-LysM 02 fwd primer, both in combination with Kbp rev, resulting in lc-LysM Kbp containing a ClaI and an EcoRI restriction site at the terminal ends, respectively. To obtain GEPII 2.7, GEPII 2.10 and GEPII 2.15 containing a 7, 10 or 15 amino acid linker within the BON and LysM domain, overlap extension PCRs using the reverse primers GEPII 2.7 rev, GEPII 2.10 rev and GEPII 2.15 rev, each in combination with Kbp fwd to receive the front fragments, were performed. The rear fragments were received using the forward primers GEPII 2.7 fwd, GEPII 2.10 fwd and GEPII 2.15 fwd, each in combination with Kbp rev. Finally, the front and rear fragments of the respective variants were fused using the ClaI restriction site adding Kbp fwd and the EcoRI site adding Kbp rev primer pair, to ligate the Kbp variants between the fluorescent proteins, respectively. Mitochondrial targeting of GEPIIs was achieved

by a tandem dimeric repeat of COX VIII targeting sequence at the N-terminal end. To obtain nuclear targeting of GEPIIs, the class III nuclear localization signal KRSWSMAFC was added via the primers cpV fwd and NLS cpV rev, or to observe cytosolic localization, the lysine rich motif LPPLERLTL derived from GP41 from human immunodeficiency virus was fused via the primers cpV fwd and NES cpV rev, both to the C-terminal end of GEPIIs. To attach GEPIIs to the inner leaflet of the plasma membrane, the K-ras-derived CAAX-motife MSKDVKKKKKKSKTKCVIM was fused to the C terminus of cpV via cpV fwd and CAAX cpV rev primers.

Table 1: Primers for the generation and targeting of GEPIIs. Table reproduced from Bischof et al., 2017, with permissions from publisher Nature Communications *(217)*.

Primer Name	Primer Sequence (5‘- 3‘)
Kbp for	GGCATCGATATGGGTCTGTTCAATTTTGTG
Kbp rev	GCTGAATTCCTCTTCCGGAATACGCAAC
lc-BON 01 fwd	CCTGAGTCAGCAGGCGAAGAACAAAATCCTTGTTGCGGTGG GGAATATTTCCGGTATTGCCAGTGTCAATAATCAGGTG
lc-BON 02 fwd	CCAATAAAGTGAATATTCAAATTGCCAACGGCAAAGCGACGGTCACTGGTAA CGGCCTGAGTCAGCAGGCGAAGAAC
lc-BON 03 fwd	AGTAAGAAGGTGCAGCAGCATCTGAACAAAACCGGTATACCGAATGCCAATA AAGTGAATATTC
lc-BON 04 fwd	TCTGTTCAATTTTGTGAAAGATGCCGGAGAAAAACTCTGGGACGCGGTTACA GGTCAGCACGATAAAGACGATCAGGCGAAGAAGGTGCAGCAGCATCTG
lc-BON 05 fwd	GGCATCGATATGGGTCTGTTCAATTTTGTG
lc-LysM 01 fwd	TTTTTAGCATCGGTTTATTCGCTTGGAAGATTTTATTGTACAGATTAGCGTTAC CGTAGACCTGTTTGGAAATGGCACTCAGAGTGTTGCCAGACTTAAC
lc-LysM 02 fwd	TGAGAATTCCTCTTCCGGAATACGCAACACTTGCCCCGGATAAATTTTATTCG GGCTTTTTAGCATCGGTTTATTCGCTTG
GEPII 2.7 fwd	GGCGGAGGCGGAAGCGGCGGACAGTTTTATACCGTTAAGTCTGGC
GEPII 2.7 rev	TCCGCCGCTTCCGCCTCCGCCGCTGGCAGTGGCTGGTGTCGCCG
GEPII 2.10 fwd	GGCGGAGGCGGAAGCGGCGGAGGCGGATCCCAGTTTTATACCGTTAAGTCT GGC
GEPII 2.10 rev	GGATCCGCCTCCGCCGCTTCCGCCTCCGCCGCTGGCAGTGGCTGGTGTCGC CG
GEPII 2.15 fwd	GGCGGAGGCGGAAGCGGCGGAGGCGGATCCGGCGGAGGCGGAAGCCAGT TTTATACCGTTAAGTCTGGC
GEPII 2.15 rev	GCTTCCGCCTCCGCCGGATCCGCCTCCGCCGCTTCCGCCTCCGCCGCTGGC AGTGGCTGGTGTCGCCG
cpV fwd	GAATTCATGGACGGCGGCGTG
NLS cpV rev	AGCAAGCTTAGCAAAACGCCATGCTCCAGCTGCGTTT GGTACCCTCGATGTTGTGGCGGATCTTGAAG
NES cpV rev	CCTAAGCTTATAACGTCAATCGTTCTAATGGAGGCAAGGTACCCTCGATGTTG TGGCGGATCTTGAAG
CAAX cpV rev	AAGCTTTTACATAATTACACACTTTGTCTTTGACTTCTTTTTCTTCTTTTTAACA TCTTTGCTCATGGTACCCTCGATGTTGTGGCGGATCTTGAAG

3.3 Protein expression and purification

For recombinant expression of purified GEPIIs the coding sequence of respective GEPII variants was sub-cloned into PETM-11 bacterial expression vectors. Proteins were expressed in *E. coli* BL-21 (DE3) cells. Single colonies were inoculated in Luria-Bertani medium (20 ml) containing 50 mg L^{-1} kanamycin and were cultured at 37 °C for 16h vigorously shaking. The pre-cultures were then transferred to 1 L of Luria-Bertani medium containing 50 mg L^{-1} kanamycin for selection. The cultures were incubated at 37 °C and shaken at 200 rpm. When an OD_{600} of 0.8 was obtained, protein expression was induced by adding 1 mM β-D-1-thiogalactopyranoside (IPTG) and cells were incubated at room temperature. After 4h cells were pelleted using a Fiberlite F9-6xx1000 rotor in a Sorvall LYNX 6000 Superspeed centrifuge at 6.000 rpm for 15 minutes, supernatant was removed and pelleted cells were resuspended in 20 mL of lysis buffer. Subsequently cells were lysed by sonication (QSONICA Ultrasonic Processor; 12 min, 50% amplitude, 1 sec on/off) and lysates were cleared by centrifugation at 12.000 rpm for 45 min at 4 °C (Sorvall LYNX 6000) followed by a filtration step (0,45 µm cellulose acetate syringe filters). Proteins were then purified using a 5 mL HisTrap column (GE Healthcare, Vienna, Austria) for immobilized metal affinity chromatography on an Äkta Pure system (GE Healthcare) at room temperature. HisTrap columns were equilibrated using lysis buffer. Cleared *E.coli* lysates were applied on the columns at a flow rate of 2 mL min^{-1} and contaminants were removed using washing buffer. Finally, proteins were eluted with purification buffer and the His6-Protein A tag was cleaved overnight at 4 °C using 2% (w/w) of 1 mg/mL recombinant His-tagged TEV protease. Processed proteins were repurified from the fusion tags and TEV protease at room temperature using size exclusion columns (16/600 200 pg, GE Healthcare) on an ÄKTA Pure system (GE Healthcare, Vienna, Austria). Subsequently proteins were eluted using elution buffer. Finally, molar protein concentration was calculated using absorbance at 280 nm, determined by NanoDrop 1000 UV/VIS spectrometer (Thermo Fisher Scientific, Vienna, Austria) and the specific molar extinction coefficient of the protein constructs (ε280: 59500 $M^{-1}cm^{-1}$).

3.4 Characterization of purified GEPIIs

Purified GEPIIs were analyzed using the CLARIOstar fluorescent plate reader (BMG Labtech, Ortenberg, Germany). For GEPII characterization, black CELLSTAR 96-well cell culture microplates (PS, F-Bottom, Greiner-Bio-One, Linz, Austria) were used. Permanently, 50 µL of diluted proteins with a concentration of 1 µM were pre-laid in the single wells.

For spectral recordings, 50 µL of elution buffers containing KCl at concentrations ranging from 0 mM to 4000 mM were added to the wells containing the purified GEPIIs, yielding a final protein concentration of 500 nM and K^+ concentrations ranging from 0 mM to 2000 mM. Spectral recordings upon increasing K^+ levels were then performed using the following setup: Excitation at 413.4 nm ± 8 nm, No. of single recorded wavelength points: 121, Emission from 441.4 nm to 561.4 nm in steps of 1 nm ± 5 nm, Gain: 2000, focal height adjusted to blank. Recorded spectra were analyzed using Graphpad Prism5 Software (Graphpad, La Jolla, USA), equalized for area under curve and smoothed using 6th order polynomial, averaging 6 neighbors on each side.

For assessment of EC_{50} values and the specificity of GEPIIs, single point scans were performed using the fluorescence multichromatic mode of BMG Analysis software with the following standardized settings: Excitation 430 nm ± 10 nm, Emissions: 475 nm ± 5 nm and 525 nm ± 5 nm. Dichroic filters used: 455 nm and 480 nm, Gain: 2000, focal height adjusted to blank. EC_{50} values of GEPIIs were determined using elution buffers containing either KCl, NaCl, RbCl, CsCl, NH_4^+ or $CaCl_2$ at concentrations ranging from 0 mM to 4000 mM. 50 µL of the respective elution buffers containing different ions at increasing concentration were then added to the proteins, resulting in a final protein concentration of 500 nM and ion concentrations ranging from 0.003 mM to 2000 mM. Finally, data were calculated dividing emissions 525/ 475 nm and ratio values were shown as difference from blank (0 mM [ion]), either normalized to 100% using maximal response or raw-values were represented and fitted using sigmoidal dose-response (variable slope) equation in Prism5 (Graphpad).

The pH stability of GEPII 1.0 was determined using the following setup: Excitation 430 nm ± 10 nm, Emissions: 475 nm ± 5 nm and 525 nm ± 5 nm. Dichroic filters used: 455 nm and 480 nm, Gain: 2000, focal height adjusted to blank. Elution buffers with pH adjusted from 5.5 to 10.0 in steps of 0.5 and recombinant GEPII 1.0 were diluted to a final protein concentration of 1 µM. 50 µL of the protein containing solutions were then transferred into the single wells of the CELLSTAR 96-well plates (Greiner-Bio-One). Elution buffers featuring different pH values were prepared, either containing 0, 0.2, 2.0 or 20.0 mM KCl and were added to the proteins bearing the same pH values, resulting in final protein concentrations of 500 nM, K^+ concentrations from 0 mM to 10 mM and adjusted pH values. Data were calculated dividing emissions 525/ 475 nm and raw ratio values were plotted over pH.

3.5 Animals

For all experiments, male C57BL/6J mice obtained from Charles River Laboratories (Sulzfeld, Germany) were used. Mice were maintained in a clean environment with a regular light-dark cycle (12h/12h) and unlimited access to chow or Western-type diet (WTD; 21% fat, 0.2% cholesterol; Ssniff Spezialdiaeten GmbH, Soest, Germany) and water. Blood was collected by either retro-bulbar or v. facialis puncture and serum was prepared by centrifugation for 10 min at 2000 rpm (himac CT15RE, Hitachi, Dusseldorf, Germany). To receive the bile from the animals, mice were sacrificed by cervical dislocation. Gallbladders were removed and centrifuged for 15 min at 2000 rpm to release the bile (Hitachi). Urine was collected from mice fed WTD for 20 weeks after cervical dislocation by direct aspiration from bladders using syringe and needle. Animal experiments were carried out in accordance with the European Directive 2010/63/EU and approved by the Federal Ministry of Science, Research, and Economy, Vienna, Austria. Renal ischemia was induced in anesthetized mice. Taking care of intestines, bowel and vasculature, microvascular clamps were applied to both renal pedicles for 25 minutes. During surgery, mice were hydrated and body temperature was kept at approximately 37 °C using an adjustable heating pad. As a control, non-operated healthy mice were used.

3.6 Assessment of clinical renal injury parameters

Biochemical analysis included serum urea and creatinine (Roche Diagnostics, Mannheim, Germany). Serum neutrophil gelatinase-associated lipocalin (Lipocalin-2) was evaluated using a commercially available enzyme-linked immunosorbent assay (R&D Systems, Minneapolis, MN, USA). Measurements were performed using a FLUOstar Omega photometer (BMG Labtech, Ortenberg, Germany).

3.7 Histology

Formalin fixed paraffin embedded kidney tissue of healthy mice and mice after ischemia reperfusion injury was sectioned at 4 µm and stained with Periodic Acid-Schiff (Sigma-Aldrich) using a standard protocol. Finally, slides were dehydrated, cleared and mounted in anhydrous mounting medium Roti-Histokitt II (Carl Roth). Stainings were evaluated for the number of tubular casts in 6 high power fields (HPFs) by one blinded examiner.

3.8 Determination of K^+ levels within human and murine samples using GEPII 1.0

For the calibration curve, elution buffers containing 200, 300, 400, 500, 600 or 700 µM KCl were prepared. 40 µL of the respective solutions were added to 40 µL containing 1 µM GEPII 1.0 containing elution buffer in the single wells, yielding a final protein concentration of 500 nM for each concentration and K^+ concentrations ranging from 100 µM to 350 µM in 50 µM steps. As a reference, elution buffer containing 0 µM KCl was analyzed. Samples were examined using the CLARIOstar fluorescence platereader (BMG Labtech) in combination with CELLSTAR 96-well plates, PS, F-Bottom (Greiner-Bio-One). Measurements were performed at an excitation of 430 nm ± 10 nm, emissions were collected at 475 nm ± 5 nm and 525 nm ± 5 nm. Dichroic filters used: 455 nm and 480 nm, Gain: 2000, focal height adjusted to blank (standard CLARIOstar setup). Final calibration curve was calculated dividing emissions 525/475 nm, the ratio values were blank corrected and were plotted over $[K^+]$. Analyzes to receive the calibration curve was performed with Prism5 (Graphpad) using one phase decay equation. The equation received was solved for x and applied to calculate the $[K^+]$ in mMol/L within biological samples, according to the formula:

$$[K^+]\left(\frac{mMol}{L}\right) = \frac{\Delta \mathrm{R} - 1.205}{-0.03651 - 1.205} \div (-0.002938) * \frac{Dilution}{1000}$$

For analyzes of [K^+] within human and murine samples, constantly GEPII 1.0 at a concentration of 1 µM and the standard CLARIOstar fluorescence plate reader setup were used. Samples were analyzed using CELLSTAR 96-well plates, PS, F-Bottom (Greiner-Bio-One).

Assessment of human plasma and murine serum K^+ levels were performed by diluting the biological samples 1:12.5 with elution buffer. Subsequently, 40 µL of each sample were added to wells already containing 40 µL GEPII 1.0 at a concentration of 1 µM, resulting in a final volume of 80 µL and a sample dilution of 1:25. Samples were analyzed, the ratios of the emissions 525/475 nm were calculated and corrected for blank. [K^+] within the samples were calculated according to the formula received from the calibration curve. Additionally, murine sera were analyzed for hemoglobin (Hb) content using drabkin's reagent and were corrected for hemolysis.

Human and murine urine [K^+] were analyzed by first diluting the samples 1:25 with elution buffer, followed by sequentially diluting this pre-dilution 3 times in 1:3 steps, resulting in 1:75, 1:225 and 1:675 dilutions. 40 µL of each urine sample were added to wells already containing 40 µL GEPII 1.0 at a concentration of 1 µM, resulting in a final volume of 80 µL and sample dilutions of 1:50, 1:150, 1:450 and 1:1350. Samples were analyzed, the ratios of the emissions 525/475 nm were calculated and corrected for blank. [K^+] within the samples were calculated according to the formula received from the calibration curve using the first serial dilution lying within the range of the calibration curve.

3.9 GEPII 1.0 based cell growth and cell death assay

Measurements at a conventional fluorescence microscope (TILL Photonics) were performed by additionally adding 5 µM GEPII 1.0 within the 100 µL of supernatant per well. INS-1 832/13 (INS-1) cells were seeded the day before the experiments in 96 well µ-plates (Ibidi, Munich, Germany) and analyzed at a confluency of 90 – 100%. Cells were permeabilized at the time point indicated by application of 30 µM digitonin. Experiments were performed at an iMic inverted and advanced fluorescent Microscope using an x20 magnification objective (alpha Plan Fluor 20x, Zeiss,

Göttingen, Germany) with a motorized sample stage (Till Photonics, Graefling, Germany). For illumination a Polychrome 5000 (Till Photonics) was used.

Emissions were recorded using a charged coupled device camera (AVT Stringray F145B, Allied Visions Technologies, Stadtroda, Germany). Filter set was obtained from AHF Analysentechnik (Tubingen, Germany). FRET-based GEPII measurements were performed at an excitation of 430 nm and emissions were collected simultaneously at 480 nm and 535 nm using an optical beam-splitter (Dichroic 69008 – ET – ECFP/EYFP/mCherry for CFP/ YFP). Alternately, FRET- and mseCFP emissions, and bright field images were acquired.

Long time cell-death experiments were performed by analyzing INS-1 cells seeded in CELLSTAR 96-well plates, PS, F-Bottom (Greiner-Bio-One). Cells were seeded one day before the experiment and showed 80-100% confluency at the day of analysis. 40 µL of assay buffer, either containing 10 mM glucose or 10 mM 2-DG and 500 nM GEPII 1.0 were used as cell supernatant. Analyses of supernatant were performed every hour for 15h by directly analyzing the plates containing the adherently growing cells using the standard CLARIOstar protocol. Calculations of $[K^+]$ were performed after blank correction using the calibration curve. For permeabilization 50 µM digitonin were added.

Bacterial growth experiments were performed using LB medium. $1{,}85*10^9$ *E.coli* cells were seeded in 39 mL at t=0h and cultured for 12 h at 37 °C vigorously shaking. After 4, 8 and 12 hours and 1 additional hour at 75 °C, suspensions were measured regarding OD_{600} and 1 mL of supernatant was centrifuged at 2500 rpm for 10 min (himac CT15RE) to pellet bacterial cells. Supernatant was taken off, the equivalent volume of 30 mM NMDG containing solution was added and the mixture was heated to 95 °C for 20 min to remove NH_4^+ from the sample and to inactivate proteases. After centrifugation at 10.000 rpm for 20 minutes, supernatant was diluted 1:10 with elution buffer, 40 µL of the pre-treated media were added to the CELLSTAR 96-well plates, PS, F-Bottom (Greiner-Bio-One), containing 40 µL of 1 µM GEPII 1.0, yielding a final dilution of 1:40, and samples were analyzed using the CLARIOstar fluorescence plate reader with standard setup. The emissions at 525/475 nm were captured and corrected for blank. $[K^+]$ within the samples were calculated according to the formula from the calibration curve.

Propidium iodide (PI) staining of bacteria was performed using PI (Sigma-Aldrich) at a final concentration of 1µg/mL in PBS. Bacterial cell numbers were adjusted to $8*10^7$ cells/mL and cells were stained for 5 min at RT using PI containing PBS, composed of (in mM): 137 NaCl, 2.7 KCl, 10 Na_2HPO_4, 1.8 KH_2PO_4. For analysis 50 µL of the bacteria containing solution were transferred into CELLSTAR 96-well plates PS, F-Bottom (Greiner-Bio-One) and fluorimetric analysis was performed using the CLARIOstar fluorescence plate reader. PI staining solution without bacteria served as blank. Excitation was set at 535 nm ± 10 nm, emission was collected at 617 nm ± 5 nm. Dichroic filters used: 576 nm, Gain: 2000, focal height adjusted to blank.

3.10 Two-photon microscopy

Surgical preparation of the cremaster muscle was performed as originally described by Baez (236) with minor modifications (237). Mouse experiments were performed according to German legislation for the protection of animals and approved by the Regierung von Oberbayern, München, Germany.

Briefly, male mice were anaesthetized with an i.p. administration of ketamine/xylazine (100 mg/kg ketamine, 10 mg/kg xylazine). The right cremaster muscle was excised by a ventral incision of the scrotum, opened ventrally and spread over the pedestal of a custom-made microscopy stage. The body temperature was maintained at 37 °C using a heating pad placed under the mouse. Throughout the procedure, as well as after surgical preparation during *in vivo* microscopy, the muscle was superfused with warm buffered saline.

In vivo imaging was performed using a Zeiss LSM 7MP microscope, equipped with a Ti:Sa laser (Chameleon Vision II). Excitation wavelength was 810 nm. Light from the specimen was collected with a W-Plan- Apochromat 20x/1.0 objective (Zeiss) and detected by two LSM BIG Detectors at 460-500 nm and 520-560 nm.

For GEPII 1.0 tissue loading, purified recombinant GEPII 1.0 was added into the muscle bath for 20 minutes (1:10 dilution) at a concentration of 4 µM. Subsequently, baseline imaging was performed. After adding 20 mM K^+ in elution buffer to a final concentration of 10mM K^+, and was washed out with buffered saline 10 min later. Measurements were conducted at 20 and 130 µm depth in the muscle tissue at the indicated time points.

3.11 Cell culture and transfection

DMEM (Sigma Aldrich) containing 10% fetal bovine serum, 100 U mL^{-1} penicillin, 100 µg mL^{-1} streptomycin and 2.5 µg mL^{-1} fungizone (Thermo Fisher Scientific) was used to grow EA.hy926, HeLa and HEK293a cells. INS-1 cells were cultivated in GIBCO RPMI Medium 1640 obtained from Thermo Fisher Scientific, additionally supplemented with 10% FCS, 10 mM HEPES, 1 mM sodium pyruvate, 0.05 mM 2-mercaptoethanl, 100 U mL^{-1} penicillin, 100 µg mL^{-1} streptomycin and 2.5 µg mL^{-1} fungizone (Thermo Fisher Scientific). Transfection of cells in 30 mm imaging dishes was performed at a confluency of 60-80% using 1 mL of serum- and antibiotic-free medium (DMEM) mixed with 1.5 µg of the respective plasmid DNA and 2.5 µg of TransFast transfection reagent (Promega, Mannheim, Germany). Cells were incubated in a humidified incubator (37 °C, 5% CO_2) for 3 h before changing back to the appropriate culture medium. After further cultivation of cells at 37 °C and 5% CO_2 for 48 h, experiments were performed.

To load cells with BAPTA-AM, culture media was removed from cells and replaced with 37 °C warm, nominally Ca^{2+} free buffer containing 50 µM of BAPTA-AM directly before fluorescence microscopic experiments. Cells were stored for 45 min in a humidified incubator (37 °C, 5% CO_2). Excessive BAPTA-AM was removed by washing steps with 37 °C warm, nominally Ca^{2+} free buffer.

3.12 Live cell imaging

Prior to the measurements, cells were equilibrated in storage buffer for 30 minutes. During the experiment, buffers were exchanged using a flow chamber containing the attached growing cells, connected to a gravity-based perfusion system (NGFI, Graz, Austria) and a vacuum pump (Chemistry diaphragm pump ME 1c, Vacuubrand, Wertheim, Germany). Experiments were performed at an iMic inverted and advanced fluorescent Microscope using a x40 magnification objective (alpha Plan Fluor 40 x, Zeiss, Göttingen, Germany) with a motorized sample stage (Till Photonics, Graefling, Germany). For illumination a Polychrome 5000 (Till Photonics) was used. Emissions were recorded using a charged coupled device camera (AVT Stringray F145B, Allied Visions Technologies, Stadtroda, Germany). Filter set was obtained from AHF Analysentechnik (Tubingen, Germany). FRET-based GEPII measurements were performed at an excitation of 430 nm and emissions were collected simultaneously at 480 nm and 535 nm using an optical beam-splitter

(Dichroic 69008 – ET – ECFP/EYFP/mCherry for CFP/YFP). Ca^{2+} imaging using CAR-GECO1 was performed at an excitation of 575 nm and emission was collected at 600 nm. For control and acquisition the software Live acquisition 2 (Till Photonics) was used.

Subcellular targeting of GEPIIs was ensured using an array confocal laser scanning microscope (ACLSM) built on a fully automatic inverse microscope (Axio Observer Z1, Zeiss, Germany), appointed with VoxCell Scan (Visitron Systems) using a x100 objective (Plan-Fluor 100x/1.45 oil, Zeiss). Excitation was performed using light coming from laser diodes (Visitron Systems). GEPIIs were excited at 445 nm (50mW) and emission was collected using emission filters ET480/40nm (Chroma Technolofies, Corporation, VT, USA). Images were captured using a CCD camera (CoolSnap HQ2, Photometrics). Pictures were processed and analyzed using the ImageJ package.

3.13 Data analysis

Analysis of raw data acquired was performed using Excel (Microsoft, Washington, US) in combination with GraphPad Prism5 software (Graphpad). Bleaching correction of live cell imaging data was performed by curve fitting.

Representative ratio images were created using MetaMorph microscopy automation and image analysis software (Molecular Devices, Sunnyvale, US). Background correction was performed and FRET- and mseCFP images were divided with appropriately set ratio range.

4 Results

4.1 Development and characterization of a genetically encoded potassium ion indicator, GEPII 1.0

Based on the recent characterization of Kbp (226) we decided to explore whether the conformational change upon K^+ binding is suitable for the design of a functional FRET-based K^+ sensor. Therefore we fused FPs such as monomeric super enhanced cyan fluorescent protein (mseCFP) (238) and circularly permuted Venus (cpV) (239), an approved FRET-pair (210), to the N- and C- terminus of Kbp, respectively, and referred to the construct as genetically encoded potassium ion indicator (GEPII) 1.0 (**Figure 14a**, upper panel) (217). This design of the probe should result in low FRET in the absence of K^+, whereas in the presence of K^+ FRET fluorescence should drastically increase due to the structural rearrangement of Kbp (**Figure 14a**, both panels). First experiments performed with the purified protein of GEPII 1.0 containing the wild type Kbp confirmed our hypothesis of a dose dependent increase of the FRET-signal with increasing K^+ concentrations, whereas FRET fluorescence was low in the absence of K^+ (**Figure 14b**). The absorbance spectrum of GEPII 1.0 remained unaffected by K^+ (**Figure 14c**). This experiments unveiled a hill slope of GEPII 1.0 for K^+ close to 1 (0,8375 ± 0,02903), indicating that one Kbp binds one K^+ (**Figure 14d** and **Appendix Table 1**), with an EC_{50} of 0,4171 mM (0.3898 mM – 0.4703 mM) (**Figure 14e** and **Appendix Table 1**) (217). In order to investigate whether GEPII 1.0 binds K^+ reversibly and repetitively, the recombinant protein was embedded in agarose and analyzed in response to addition and removal of 1 mM K^+ via a perfusion system (**Figure 14f**). This experiments pointed to a reversible binding of K^+ by Kbp, as FRET-ratio signals of GEPII 1.0 increased and decreased repetitively in response to K^+ (**Figure 14f**). Experiments determining the association rate constant (k_{on}) and the dissociation rate constant (k_{off}) unveiled fast on and off kinetics of the sensor with k_{on} values of $1{,}19*10^{-1}$ mM^{-1} s^{-1} and k_{off} values of $7{,}53*10^{-1}$ s^{-1} (**Figure 14g**) (217).

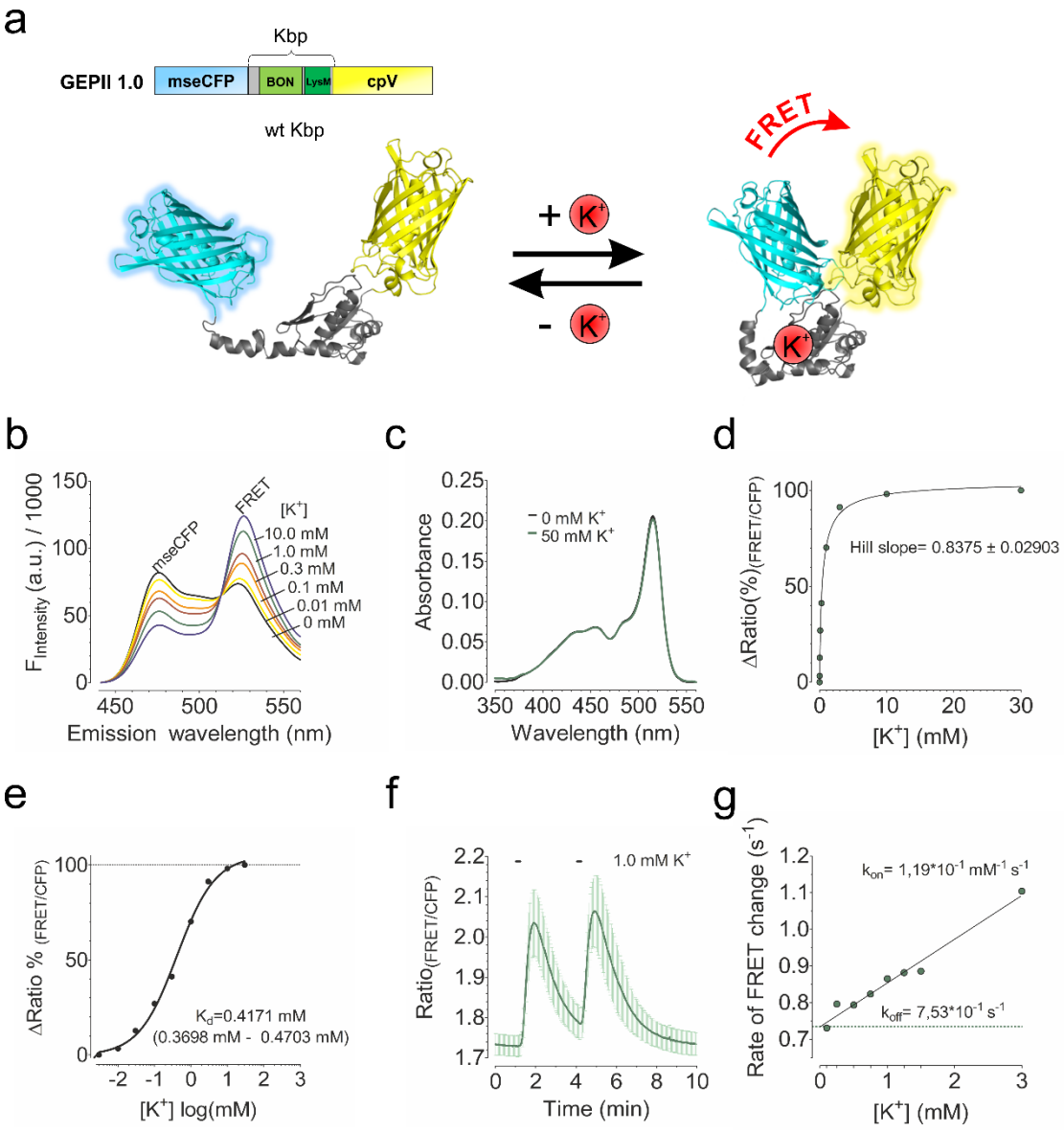

Figure 14: Design and *in vitro* characterization of GEPII 1.0. (**a**) Schematic representation of GEPII 1.0 consisting of a N-terminal monomeric super enhanced cyan fluorescent protein (mseCFP, cyan, all panels) and a C-terminal circularly permuted venus (cpV, yellow, all panels). The two fluorescent proteins flank wild type Kbp (wt Kbp), composed of (interdomain-) linkers (grey), the BON (light green) and the LysM (dark green) domains (upper panel). Lower panels demonstrate the proposed conformations and the principle of function of GEPII 1.0 as 3D-structure, either in the K^+ unbound (left panel) or K^+ bound conformation of Kbp (grey, both panels). (**b**) *In vitro* emission spectrum of GEPII 1.0 at different concentrations of K^+ ranging from 0 mM to 10.0 mM K^+. (**c**) Absorbance spectrum of GEPII 1.0 at 0 mM K^+ (black line) and 50 mM K^+ (green line), n=1. (**d**) Normalized K^+ binding kinetic of GEPII 1.0 using binding-saturation fit. Hill slope ± SD is indicated. Data represents average ± SD, n=4. (**e**) Normalized concentration response curve of GEPII 1.0 for K^+ *in vitro,* K_D and 95% confidence interval are indicated, data represents average ± SD, n=4. (**f**) K^+ binding reversibility test of GEPII 1.0 embedded in 0.5% agarose upon administration and removal of 1.0 mM K^+ using a gravity based perfusion system, data represents average ± SD, n=7. (**g**) Reaction rate constant of GEPII 1.0 at 25 °C *in vitro.* K_{on} and K_{off} are indicated in the panel, data represents average, n=3 for each concentration. Reproduced from Bischof et al., 2017 with permission of publisher Nature Communications (217).

To further characterize the novel genetically encoded probe, several important aspects involving temperature sensitivity and stability, pH constancy as well as K^+ selectivity were investigated (**Figure 15**). Interestingly, K^+ binding by GEPII 1.0 showed a temperature dependency, as the EC_{50} of GEPII 1.0 increased with increasing temperature from 0.43 mM (0.38 mM - 0.47 mM) at 25 °C to 4.257 mM (3.92 mM - 4.62 mM) at 45 °C (**Figure 15a**) (217). However, GEPII 1.0 proved very thermostable, as the FRET-ratio signal of GEPII 1.0 repeatedly and totally recovered in the presence of K^+ after repetitive heating to 65 °C and cooling to 25 °C (**Figure 15b**). Next, analyses of the pH dependency of the FRET-ratio signal received from GEPII 1.0 in the presence of different [K^+] were performed (**Figure 15c**). These experiments demonstrated an almost constant K^+ response of GEPII 1.0 from pH 7.0 to pH 9.0 (**Figure 15c**), covering the range of physiologic intra- and extracellular pH values (217,240,241).

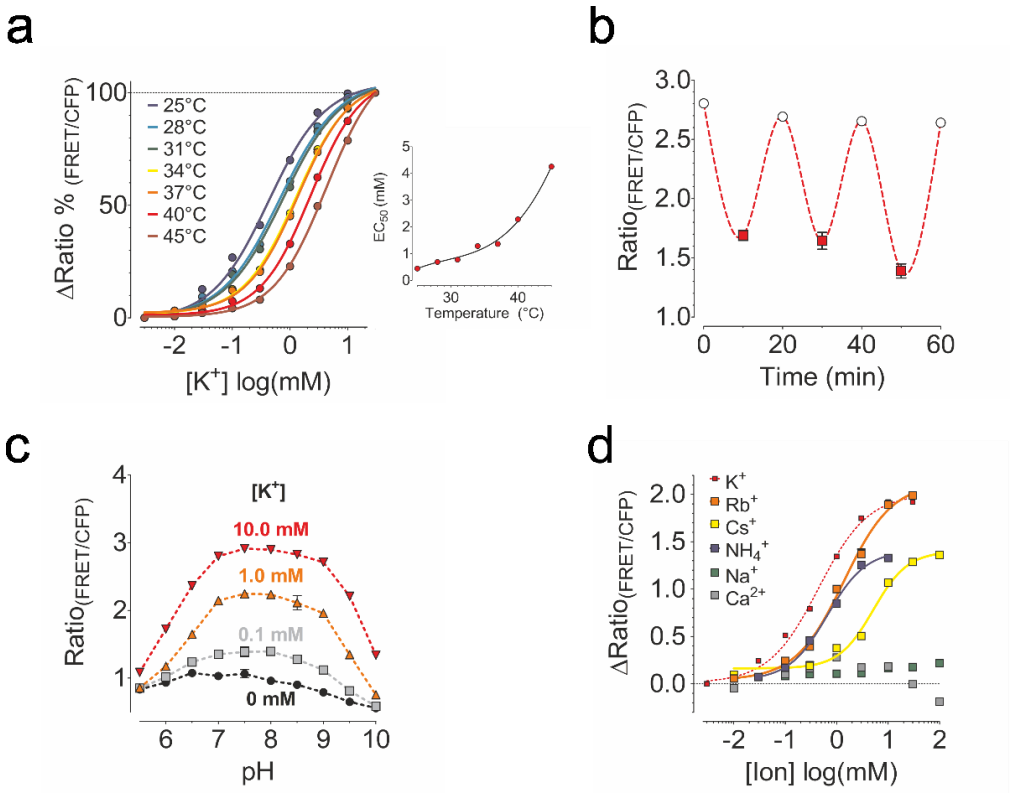

Figure 15: K^+ selectivity, thermo- and pH stability of GEPII 1.0. (**a**) Normalized EC_{50} curves of GEPII 1.0 for K^+ at different temperatures ranging from 25 °C (dark blue line) to 45 °C (dark red line) (left panel, data represents average ± SD, n=6 for all). Right panel represents respective EC_{50} values of GEPII 1.0 plotted over temperature. (**b**) FRET-ratio signal of GEPII 1.0 over time in the presence of 5.0 mM K^+ recorded at 25 °C (white circles) and 65 °C (red squares). Data shows average ± SD, n=8. (**c**) FRET-ratio signals of GEPII 1.0 in the absence (black), or presence of 0.1 mM (grey), 1.0 mM (orange) or 10.0 mM K^+ (red) at different pH values. Data represents average ± SD, n=8 for each. (**d**) Ion selectivity of GEPII 1.0 for K^+ (red dotted line and squares), in comparison to Rb^+ (orange line and squares), Cs^+ (yellow line and squares), NH_4^+ (blue line and squares), Na^+ (green line and squares and Ca^{2+} (grey line and squares). Average ± SD is indicated, n=3 for each ion and concentration. Reproduced from Bischof et al., 2017 with permission of publisher Nature Communications (217).

Further, we analyzed the selectivity of GEPII 1.0 for K^+ *in vitro*. Therefore, increasing concentrations of several monovalent cations, having a similar ionic radius as K^+ such as Rb^+, Cs^+, Na^+ and NH_4^+, or the physiologically important divalent cation Ca^{2+}, were tested. The FRET-ratio signal of GEPII 1.0 remained unaffected by the physiologically important ions Na^+ and Ca^{2+} (**Figure 15d** and **Appendix Table 1**). GEPII 1.0 did only respond to NH_4^+ (EC_{50}=0.6574 mM), Rb^+ (EC_{50}=1.379 mM) or higher concentrations of Cs^+ (EC_{50}=5.154 mM) (**Figure 15d** and **Appendix Table 1**), pointing to the selectivity of Kbp for K^+.

4.2 Quantification of K^+ within biological samples using GEPII 1.0

4.2.1 Determination of [K^+] within human and murine samples

We speculated, that the highly K^+ sensitive GEPII 1.0 is a suitable tool for the measurement of the [K^+] within tiny volumes of human and murine serum, plasma and urine samples. Thus, we tested whether GEPII 1.0 can accomplish such measurements in a convenient, fast, and reliable manner. Such an assay may be an easy, cheap, and sensitive high throughput alternative to conventional K^+ quantification methods such as the ISE (**Figure 16a**). First, an analytical calibration curve of GEPII 1.0 was established for the absolute quantification of [K^+] within biological samples using recombinant GEPII 1.0 (**Figure 16b**). To test our idea of using GEPII 1.0 for the quantification of [K^+], we then collected urine samples of healthy human donors, determined [K^+] within these samples using recombinant GEPII 1.0 and compared the results with the values determined by a conventional ISE (**Figure 16c**). The comparison showed a close agreement between the two methods (**Figure 16c**). GEPII 1.0 even proved stable within human urine samples for at least 4h (**Figure 16d**) (217).

Further, human plasma samples of healthy human donors and hemodialysis patients (HD-P) were analyzed using the same procedure. Importantly, the recombinant protein also proved stable within human plasma samples for at least 4h (**Figure 16e**). To test the suitability, accuracy and precision of the novel [K^+] determination method for the determination of [K^+] under both, physiological and pathological conditions, we again compared [K^+] determined using GEPII 1.0 with [K^+] determined using the ISE instrument (**Figure 16f**) (217).

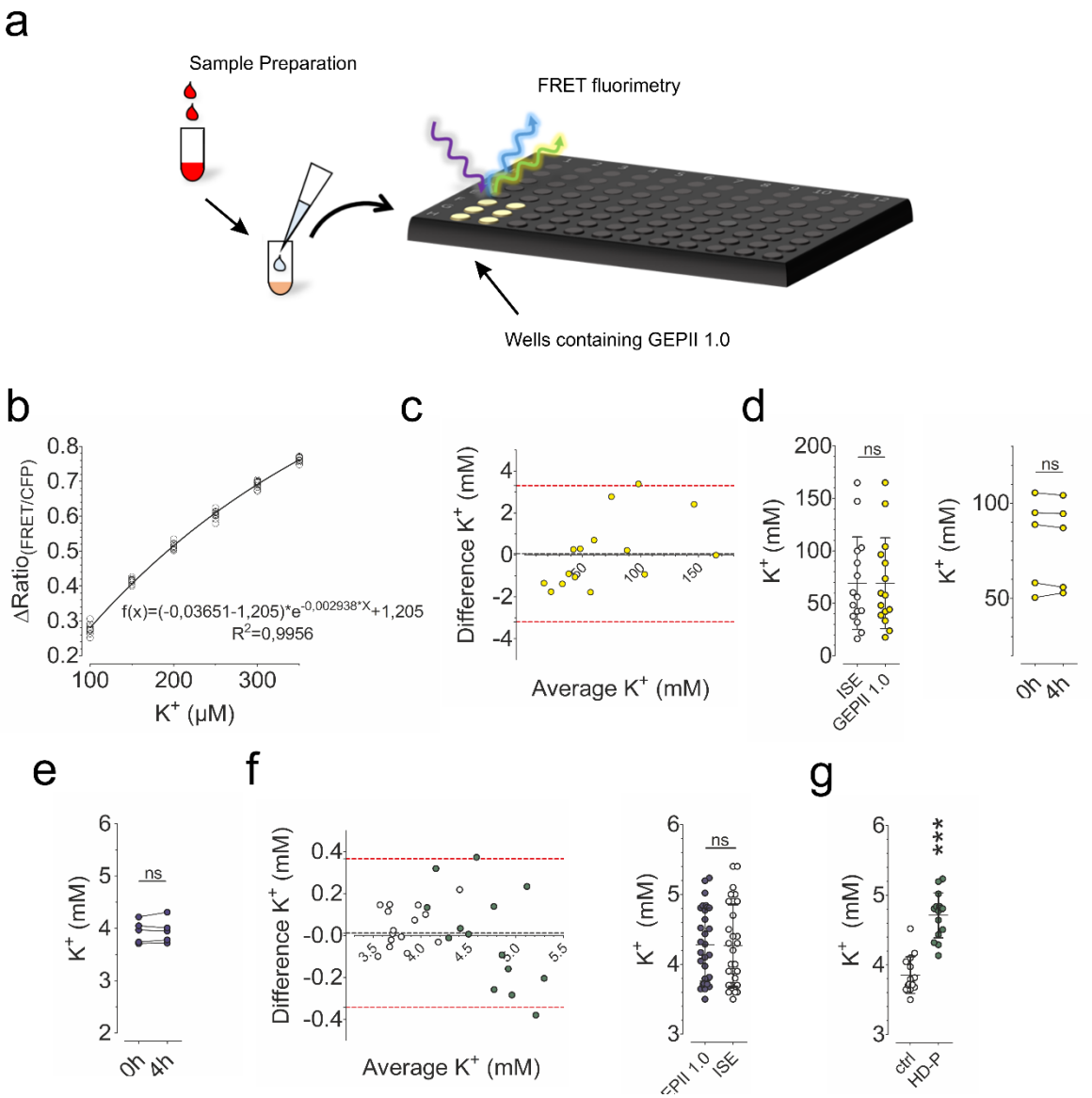

Figure 16: Application of GEPII 1.0 for the determination of [K⁺] within human urine and serum samples. (**a**) Schematic representation of the workflow to determine [K⁺] within biological samples. After sample collection and preparation, the sample is diluted and added to wells containing recombinant GEPII 1.0. (**b**) Analytical calibration curve and function of recombinant GEPII 1.0 in distilled water containing defined [K⁺] ranging from 100 µM to 350 µM K⁺. Data represents each replicate of the measurements, n=10. Values were fitted using one phase decay. R^2 and function (f(x)) are indicated in the panel. (**c**) Bland-Altman plot (left panel) showing human urine [K⁺] of healthy human donors determined using ISE and GEPII 1.0, respectively (n=15). Bias (black dashed line) and 95% limits of agreement (red dashed lines) are demonstrated. Right panel shows the direct comparison of [K⁺] determined using ISE and GEPII 1.0. Data represents each sample and average ± SD, n=15, p=0.9625, paired t-test. (**d**) Stability test of recombinant GEPII 1.0 in human urine samples. Same samples were analyzed at t=0h (white circles) and after 4h (yellow circles) (n=5, p=0.4444, paired t-test). (**e**) Stability test of recombinant GEPII 1.0 within human plasma samples. Same samples were analyzed at t=0h and after 4h (n=5, p=0.5238, paired t-test). (**f**) Left panel represents Bland-Altman plot showing plasma [K⁺] of healthy human donors (white circles, n=15) and hemodialysis patients (blue circles, n=15) determined using ISE and GEPII 1.0, respectively. Bias (black dashed line) and 95% limits of agreement (red dashed lines) are demonstrated. Right panel shows a direct comparison of [K⁺] determined using GEPII 1.0 (blue circles) and ISE (white circles) (n=30, data represents each sample and average ± SD, p=0.6504, paired t-test). (**g**) Comparison of [K⁺] determined using GEPII 1.0 of healthy human donors (white circles, ctrl) and hemodialysis patients (blue circles, HD-P), n=15 for both, data represents each replicate and average ± SD, ***p<0.0001, unpaired t-test. Reproduced from Bischof et al., 2017 with permission of publisher Nature Communications (217).

Again, GEPII 1.0 was able to precisely determine [K^+] within these samples when compared to values determined by ISE (**Figure 16f**) (217).
As expected, samples taken from HD-P showed increased plasma [K^+] in comparison to healthy human donors, as we have determined using GEPII 1.0 (**Figure 16g**).

To demonstrate the significance of such a novel assay, [K^+] within samples of small laboratory animals were determined, as these animals possess a very limited amount of bodily fluids. Having demonstrated the accuracy and precision of purified GEPII 1.0 for such applications in human samples (**Figure 16**), we determined the [K^+] within serum samples of mice. For our [K^+] measurements in murine serum samples using GEPII 1.0 there was no need to sacrifice the animal, as one drop of blood was sufficient to perform the analyses. GEPII 1.0 proved stable within murine serum (**Figure 17b**) and urine samples (**Figure 17c**) for at least 4h. Independent on the collection method, [K^+] of single animals matched whether the blood was taken from the orbital sinus (6.695 mM ± 0.3402 mM) or the facial vein (6.706 mM ± 0.3450 mM, p=0.9319) (**Figure 17c**) (217). Additionally, [K^+] measurements were performed within murine urine and bile samples with [K^+] of 242.2 mM ± 47.51 mM within urine and 6.220 mM ± 2.525 mM within bile samples (**Figure 17d**) (217).

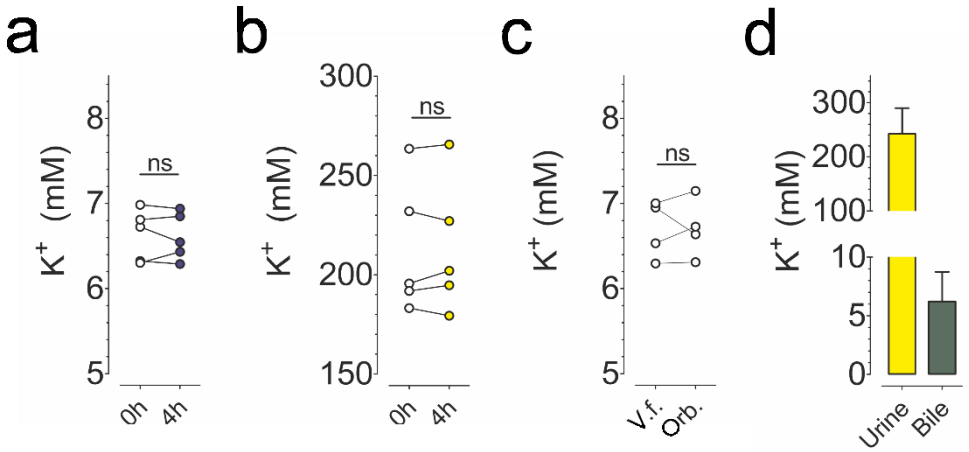

Figure 17: Determination of [K^+] within murine serum, urine and bile samples. (**a**) Stability test of recombinant GEPII 1.0 within murine serum samples. Same samples were analyzed for [K^+] at t=0h and after 4h using GEPII 1.0 (n=5, p=0.7416, paired t-test). (**b**) Same urine samples of mice were analyzed for their [K^+] at t=0h and after 4h using GEPII 1.0 (n=5, p=0.8134, paired t-test). (**c**) Comparison of murine serum [K^+] determined using GEPII 1.0. Samples were collected from the same animal, either from the vena facialis (V.f.) or by retro-orbital bleeding (Orb.) (n=5, p=0.9319, paired t-test). (**d**) [K^+] of murine urine (yellow bar, n=11, average ± SD) and bile samples (green bar, n=7, average ± SD). Reproduced from Bischof et al., 2017 with permission of publisher Nature Communications (217).

To further challenge the GEPII 1.0 based K^+ quantification assay, we went on in a murine kidney dysfunction model. Ischemia reperfusion injury (IRI) of the kidney was surgically inflicted. The renal damage was confirmed by measuring typical clinical kidney function parameters such as serum creatinine (**Figure 18a**), serum urea levels (**Figure 18b**), serum lipocalin-2 (**Figure 18c**), as well as histologically by counting tubular casts (**Figure 18d**). All of these parameters were drastically increased in IRI mice in comparison to control mice (**Figure 18a-d**) (217).

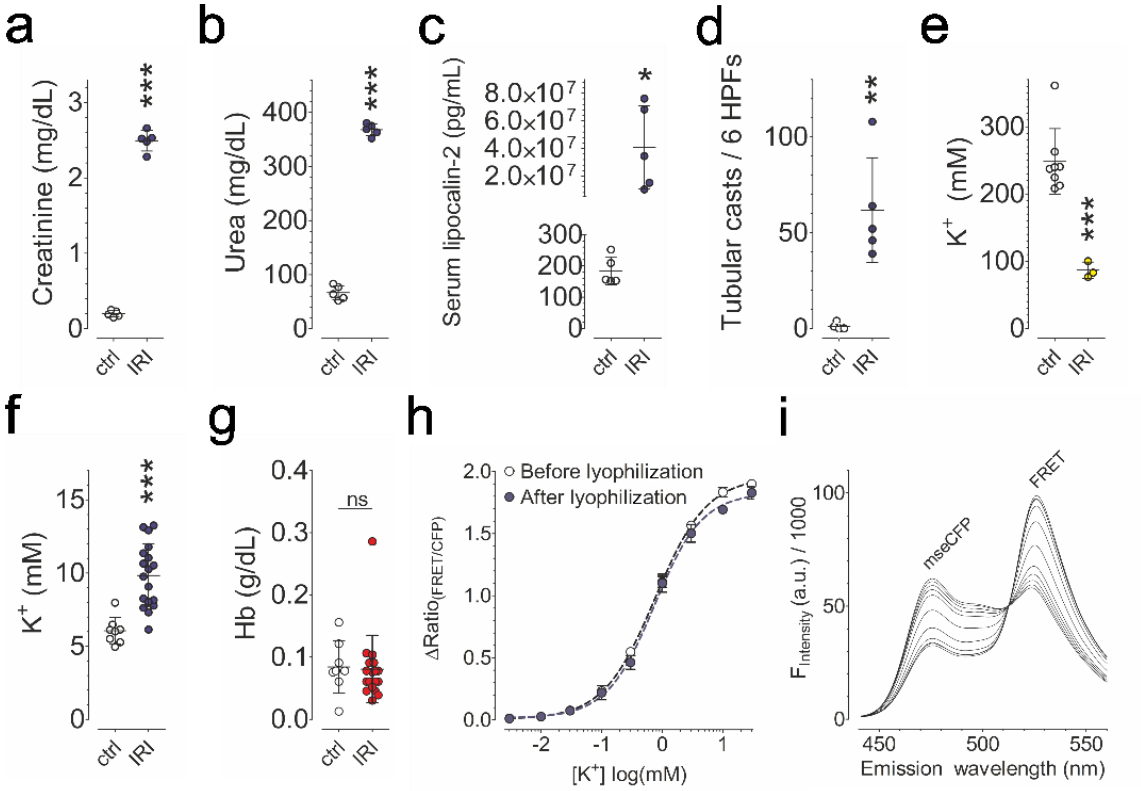

Figure 18: Determination of [K^+] with recombinant GEPII 1.0 within murine serum samples of healthy mice and mice after induced ischemia reperfusion injury. (**a**) Serum creatinine levels of healthy mice (white circles, ctrl) and mice after induced renal ischemia reperfusion injury (blue circles, IRI). Data represents each sample (n=5 for both) and average ± SD, ***p<0.0001, unpaired t-test. (**b**) Serum urea levels of healthy mice (white circles, ctrl) and mice after induced renal ischemia reperfusion injury (blue circles, IRI). Data represents each sample (n=5 for both) and average ± SD, ***p<0.0001, unpaired t-test. (**c**) Serum lipocalin-2 levels of healthy mice (white circles, ctrl) and mice after induced renal ischemia reperfusion injury (blue circles, IRI). Data represents each sample (n=5 for both) and average ± SD, *p=0.0163, unpaired t-test. (**d**) Tubular casts per six high power fields of healthy mice (white circles, ctrl) and mice after induced renal ischemia reperfusion injury (blue circles, IRI). Data represents each sample (n=5 for both) and average ± SD, **p=0.0011, unpaired t-test. (**e**) Urine [K^+] of healthy mice (white circles, ctrl, n=8) and mice after induction of ischemia reperfusion injury (yellow circles, IRI, n=3). Data represents each sample and average ± SD, ***p=0.0004, unpaired t-test. (**f**) Serum [K^+] of healthy mice (white circles, ctrl, n=8) and mice after induced ischemia reperfusion injury (blue circles, IRI, n=18). Data shows each sample and average ± SD, ***p<0.0001, unpaired t-test. (**g**) Serum hemoglobin (Hb) levels of healthy mice (white circles, ctrl, n=8) and mice after induced renal ischemia reperfusion injury (red circles, IRI, n=18) of the same serum samples as demonstrated in (**f**). Data shows each sample and average ± SD, p=0.8725, unpaired t-test. (**h**) EC_{50} curves of the same wells containing GEPII 1.0 and increasing [K^+] before (white circles, black dashed line) and after lyophilization (blue circles, blue dashed line). Data shows average ± SD, n=3 for each. (**i**) Representative emission spectrum of GEPII 1.0 in the presence of different [K^+] after lyophilization. Reproduced from Bischof et al., 2017 with permission of publisher Nature Communications (217).

Our GEPII 1.0 based K^+ quantification assay within urine (**Figure 18e**) and serum samples (**Figure 18f**) of these mice clearly confirmed the dramatic renal injury of IRI mice compared to controls, by decreased urine and increased serum [K^+] (**Figure 18e** and **18f**). Importantly, hemoglobin levels in murine serum levels were not significantly different, excluding artefacts caused by hemolysis (**Figure 18g**) (217).

As a simplification for the [K^+] determination assay, we tested whether GEPII 1.0 is still functional after a freeze-drying process. Therefore, a 96-well plate containing recombinant GEPII 1.0 in solution was lyophilized and stored for two weeks in the dark at -80 °C. For analysis, the same wells before and after lyophilization of GEPII 1.0 were compared concerning their FRET-ratio signal in response to different K^+ concentrations (**Figure 18h**). These experiments demonstrated the fully restored functionality of GEPII 1.0 *in vitro* after freeze-drying (**Figure 18h** and **18i**). Taken together, our results demonstrate the suitability of GEPII 1.0 for the quantification of K^+ levels, which can be accomplished in an automatable 2-step process, including sample preparation in wells containing (freeze-dried) GEPII 1.0 followed by analysis using FRET-fluorimetry (**Figure 16a** and **Figure 18h** and **18i**) (217).

4.2.2 Quantification of [K^+] in cell cultivation media to determine cell viability and cell death

Almost all cells, ranging from simple bacteria to highly differentiated mammalian cells, maintain a steep K^+ gradient across their plasma membrane (1,17,242). This K^+ gradient is mostly achieved by an active, ATP consuming process of a Na^+/K^+ ATPase and is important for many cellular processes and biological functions. Based on this common characteristic of vital cells, we decided to test whether the measurement of $[K^+]_{ex}$ is a reasonable marker to estimate cell death (**Figure 19a**). First we examined an increasing number of cells after full cell permeabilization in a K^+ free environment and tested the cell supernatant for its [K^+] using recombinant GEPII 1.0 (**Figure 19b**) (217). As expected, $[K^+]_{ex}$ linearly correlated with increasing cell numbers (**Figure 19b**), suggesting that cells of the same type possess same $[K^+]_i$. Considering these results, demonstrating that already a few dying cells release a K^+ amount to the extracellular medium detectable with recombinant GEPII 1.0, we proceeded by analyzing the supernatant of INS-1 cells, a pancreatic β-cell line, over time (**Figure 19c**). Cells were kept either in the presence of 10 mM glucose or 10 mM of its toxic antimetabolite 2-deoxy-D-glucose (2-DG) and GEPII 1.0 in the

supernatant (**Figure 19c**). While in the presence of physiological concentrations of glucose in the cultivation media $[K^+]_{ex}$ remained almost constant over time, cells cultured in the presence of 2-DG gradually increased $[K^+]_{ex}$ as a consequence of the severe energy crisis caused by the glycolysis inhibitor (**Figure 19c**) (243). By addition of digitonin at the end of the measurements, $[K^+]_{ex}$ increased to similar levels, pointing to the same cell number under both condition (**Figure 19c**) (217). To explore whether the usage of GEPII 1.0 in the extracellular space is also applicable using a conventional fluorescence wide-field microscope, cells seeded in 96-well plates were analyzed in response to a necrotic stimulus (**Figure 19d**).

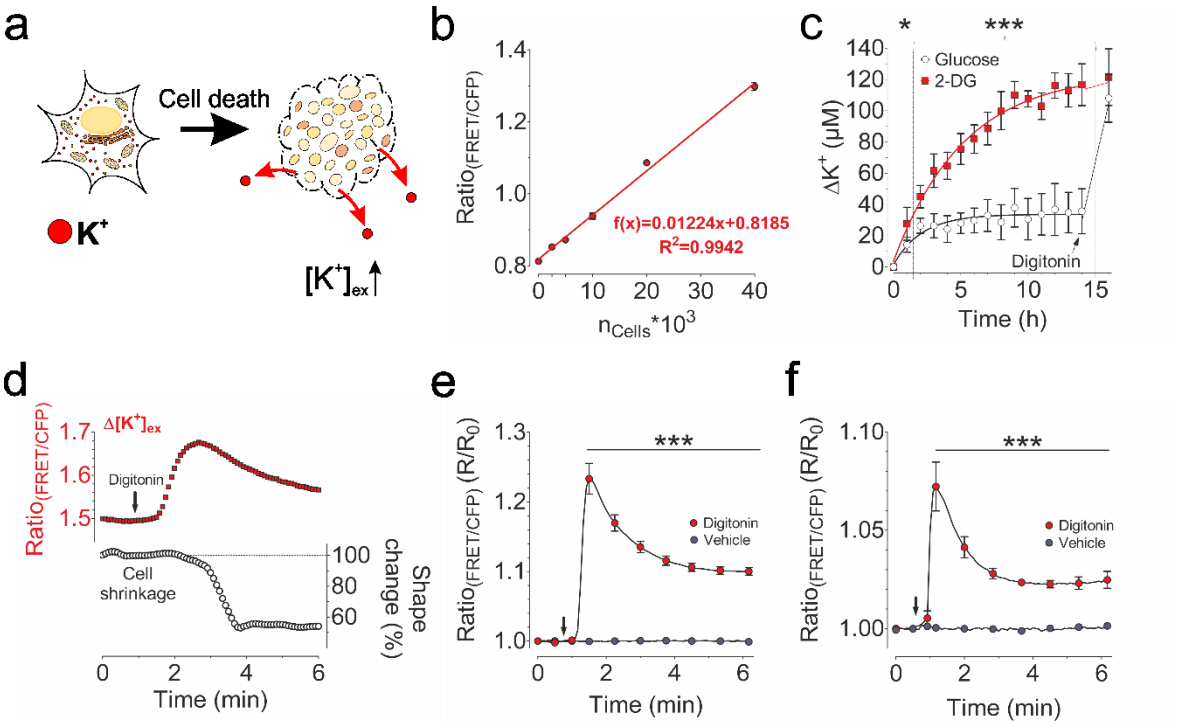

Figure 19: Application of recombinant GEPII 1.0 for the dynamic visualization of cell death over time. (**a**) Schemata demonstrating cellular loss of K^+ upon cell death, leading to an increase in $[K^+]_{ex}$. (**b**) Correlation analysis of the average FRET-ratio signal ± SD measured using recombinant GEPII 1.0 plotted over defined HeLa cell numbers. HeLa cells were permeabilized using 30 µM digitonin (n=4 for each cell number). (**c**) Extracellular $[K^+]$ in the supernatant of INS-1 cells measured with recombinant GEPII 1.0 plotted over time. Cells were either kept in the presence of 10 mM glucose (white circles, black line) or 10 mM 2-DG (red squares, red line). After 14h, 50 µM digitonin were applied. Data shows average ± SD, n=6 for both, *p=0.0189, ***p<0.0005 using unpaired t-test. (**d**) Representative FRET-ratio signal over time of GEPII 1.0 (red squares) in the supernatant of HeLa cells upon application of 30 µM digitonin at the time point indicated in the panel. Representative single cell morphology (white circles) of a HeLa cell is demonstrated as % of shape change. (**e**) Normalized FRET-ratio signal of GEPII 1.0 in the supernatant of HEK293a cells upon application of 30 µM digitonin (red circles) or the same amount of DMSO (blue circles) at the time point indicated in the panel (black arrow). Data represents average ± SD, n=6 for both conditions, ***p<0.0001. (**f**) Normalized FRET-ratio signal of GEPII 1.0 in the supernatant of Ea.hy926 cells upon application of 30 µM digitonin (red circles) or the same amount of DMSO (blue circles) at the time point indicated in the panel (black arrow). Data represents average ± SD, n=6 for both conditions, ***p<0.0005. Reproduced from Bischof et al., 2017 with permission of publisher Nature Communications (217).

Simultaneously to recording the FRET-ratio signal of GEPII 1.0, bright-field images of HeLa cells were acquired for the correlation of morphological cell changes with their K^+ release (**Figure 19d**). Interestingly, $[K^+]_{ex}$ drastically increased prior to detectable morphological alterations of the cells (**Figure 19d**). Similar results of increasing $[K^+]_{ex}$ upon application of digitonin were obtained using other cell lines, such as human embryonic kidney cells (HEK293a) (**Figure 19e**) or Ea.hy926, an endothelial hybridoma cell line (**Figure 19f**) (217).

4.2.3 Quantification of $[K^+]$ in cell cultivation media to determine cell growth

In contrast to dying cells we hypothesized that, vice versa, cell proliferation may decrease $[K^+]_{ex}$ (**Figure 20a**). To test our assumption, we investigated the $[K^+]_{ex}$ over time of bacterial culture media. $1.85*10^9$ *E.coli* cells were seeded at t=0h in 39 mL LB media, and $[K^+]_{ex}$ using purified GEPII 1.0 as well as the OD_{600} were analyzed every 2h for 12h (**Figure 20b**) (217). Our experiments demonstrated a gradual decrease of $[K^+]_{ex,}$ especially during the exponential phase of bacterial growth (**Figure 20b**). Altogether, $[K^+]_{ex}$ within the media decreased from 10.2 mM at t=0h to 9.4 mM after 12h of bacterial cultivation (**Figure 20b**). As expected, $[K^+]_{ex}$ well correlated with the increasing cell number (**Figure 20c**). Final heating of the culture to 75 °C for 1h resulted in positive propidium iodide (PI) staining (**Figure 20d**) and restored $[K^+]$ within the media, demonstrating the applicability of measuring $[K^+]_{ex}$ for the assessment of vital cells, whereas OD_{600} remained almost unaffected under these conditions (**Figure 20b**) (217).

Interestingly, within a group of diverse antibiotics tested, only ampicillin led to positive PI staining, whereas kanamycin and gramicidin treatment did not alter PI fluorescence (**Figure 20d**). However, $[K^+]_{ex}$ was significantly elevated by all substances tested, indicating low cell viability, which was detected using GEPII 1.0 (**Figure 20e**).

To simplify the method of measuring $[K^+]$ over time within culture medium, we tested the functionality of GEPII 1.0 within agar-agar (**Figure 20f and 20g**) (217). Also under these conditions, GEPII 1.0 was able to report different predefined (**Figure 20f**) as well as dynamic K^+ alterations (**Figure 20g**), indicating that the fluorescent tool can be used for the determination of cell growth or death within solid cultivation matrices such as agar-agar as well (217).

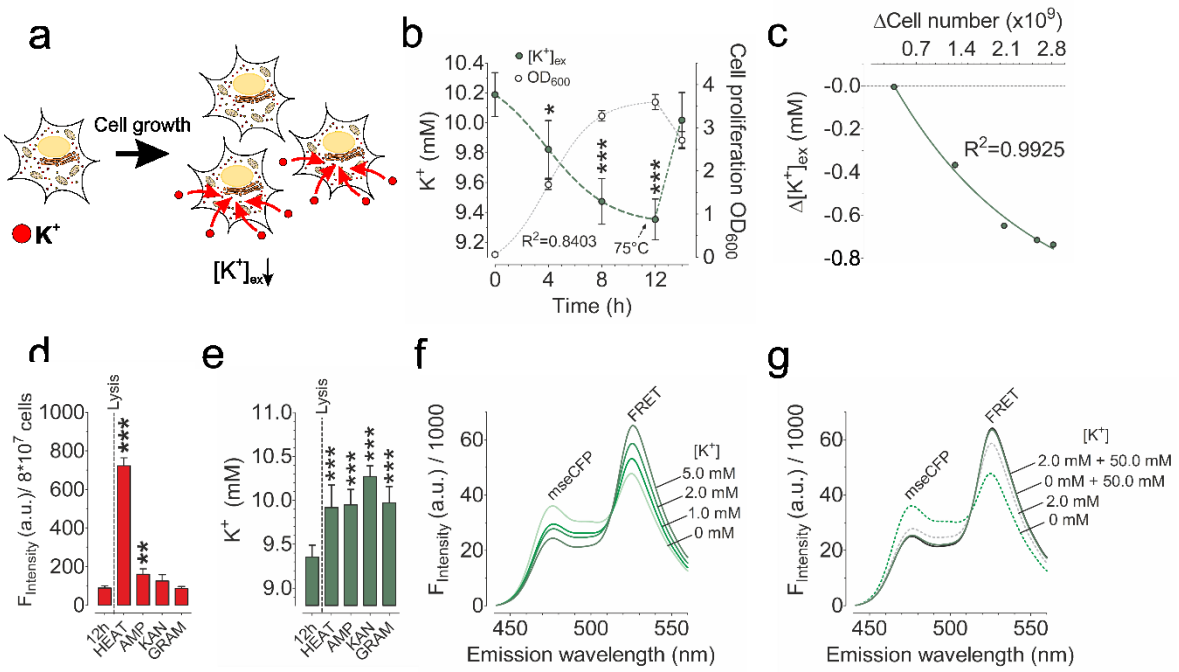

Figure 20: Application of recombinant GEPII 1.0 for the dynamic visualization of cell growth over time. (**a**) Schemata demonstrating cellular uptake of K^+ upon cell growth, leading to a decrease in $[K^+]_{ex}$. (**b**) $[K^+]_{ex}$ of *E.coli* culture medium determined using recombinant GEPII 1.0 (green circles and green dashed line) and OD_{600} (white circles and grey dashed line) plotted over time. Data shows average ± SD of 5 measurements, *p=0.05, ***p<0.0005 using one-way ANOVA test with Tukey´s multiple comparison test. After 12h bacterial cultures were heated to 75 °C as indicated in the panel. R^2 of $[K^+]_{ex}$ fitted using a sigmoidal curve is given in the panel. (**c**) Correlation analysis of $[K^+]_{ex}$ and cell number of data represented in (**b**). Data represents average measurement values. R^2 of points, fitted using one phase decay, is indicated in the panel. (**d**) Propidium iodide (PI) fluorescence intensity of PI stained *E.coli* cultures after 12h of bacterial growth (12h) or after different approaches to lyse the cells for 1h including heating the culture to 75 °C (HEAT), or treatment with ampicillin (AMP), kanamycin (KAN) or gramicidin (GRAM). Bars represent average ± SD, n=5 for each condition, **p<0.001, ***p<0.0001 using one-way ANOVA test with Tukey's multiple comparison test. (**e**) Same bacterial cultures as seen in (**d**) were analyzed for $[K^+]_{ex}$ using recombinant GEPII 1.0 after 12h of bacterial growth (12h), or after different approaches to lyse the cells for 1h using heating the culture to 75 °C (HEAT), or treatment with ampicillin (AMP), kanamycin (KAN) or gramicidin (GRAM). Bars show average ± SD, n=5 for each condition ***p<0.0001 using one-way ANOVA test with Tukey's multiple comparison test. (**f**) Fluorescence emission spectra of GEPII 1.0 embedded in agar-agar containing 0, 1.0, 2.0 or 5.0 mM K^+. (**g**) Fluorescence emission spectra of GEPII 1.0 embedded in agar-agar containing 0 (green dashed line) or 2.0 mM K^+ (grey dashed line), and same both samples after addition of 50.0 mM K^+ (solid lines). Reproduced from Bischof et al., 2017 with permission of publisher Nature Communications (217).

4.3 Recombinant GEPII 1.0 is applicable for *in vivo* imaging using two-photon excitation

To test the ability of GEPII 1.0 to detect K^+ fluctuations *in vivo*, purified GEPII 1.0 was loaded into an exposed striated muscle of a mouse. Application of the recombinant protein onto the exposed muscle led to a deep diffusion of GEPII 1.0 into the tissue within 20 minutes, without entrance of the protein into blood vessels (**Figure 21a**). First experiments demonstrated a constant fluorescence signal, indicating that the probe was stable (**Figure 21a**) (217). To figure out whether the recombinant probe is still functional *in vivo*, 10 mM of K^+ were added and removed from the preparation via a water bath (**Figure 21b *and* 21c**). The addition of K^+ resulted in a dramatic increase of the FRET-ratio signal measured in different tissue depths, demonstrating that the probe remained

fully functional under these conditions (**Figure 21b** and **21c**). Vice versa, GEPII 1.0 also responded upon removal of K^+ by a decrease of the FRET-ratio signal (**Figure 21b**) (217).

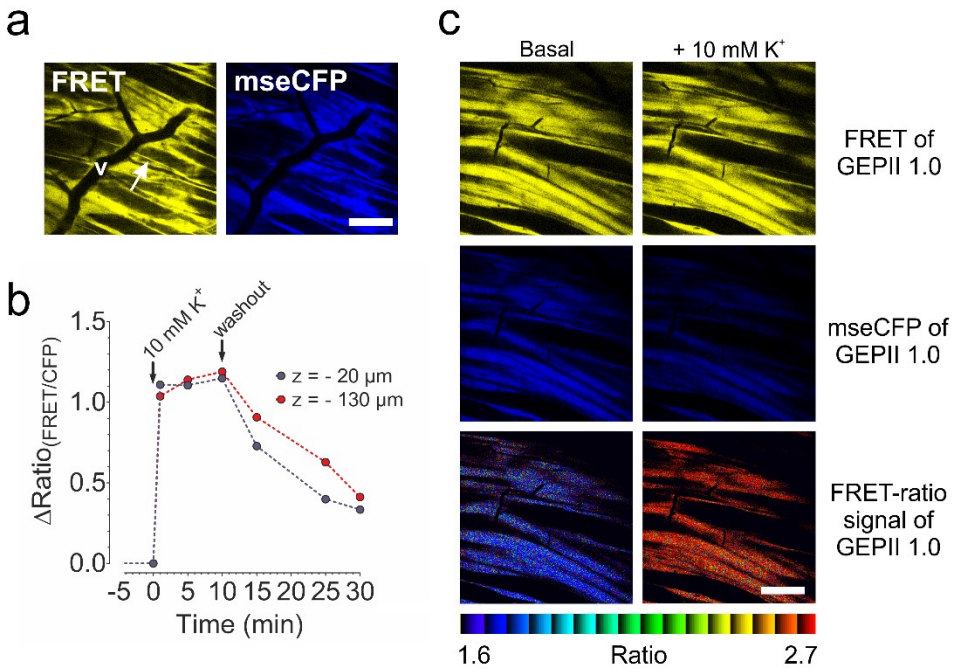

Figure 21: Application of GEPII 1.0 for *in vivo* imaging of extracellular K^+ alterations. (**a**) Representative FRET (left panel) and mseCFP images (right panel) of GEPII 1.0 loaded in the mouse cremaster muscle. Images were acquired at a z-depth of 50 µm. Blood vessels (v) and localization of GEPII 1.0 along muscle fibers (arrow) are shown. Scale bar represents 100 µm. (**b**) Representative FRET-ratio responses of GEPII 1.0 over time loaded into the cremaster muscle of a mouse. Response was recorded at different z-depths of 20 µm (blue circles) and 130 µm (red circles) upon administration and washout of 10.0 mM K^+ at time points indicated (black arrows). (**c**) Representative FRET (yellow, upper) and mseCFP (blue, middle) intensity images of recombinant GEPII 1.0 loaded into the cremaster muscle of a mouse. Bottom images represent pseudo-colored ratio images.

Images were acquired either under basal conditions (left images) or upon administration of 10 mM K^+ (right images) as shown in (**b**). Scale bar represents 100 µm. Reproduced from Bischof et al., 2017 with permission of publisher Nature Communications (217).

4.4 Testing the functionality of GEPII 1.0 in situ

A further important aspect of the novel genetically encoded K^+ indicator was to test its functionality when expressed in single living mammalian cells. Therefore, HeLa and INS-1 cells transiently transfected and expressing cytosolic targeted GEPII 1.0 were analyzed using a conventional fluorescence wide-field microscope. Cells expressing the probe showed a physiologic morphology, indicating that GEPII 1.0 is non-toxic for mammalian cells (**Figure 22a**). To test the sensor also for its functionality when expressed in living cells, increasing concentrations of extracellular K^+ were administered to permeabilized cells using a gravity based perfusion system. Subsequently upon administration, GEPII 1.0 responded by an increase in FRET and a decrease in the donor fluorescence (**Figure 22b**) (217). As expected, the FRET-ratio signal represented the increase in $[K^+]$ in a dose dependent manner (**Figure 22b** and **22c**). We furthermore generated a red-shifted GEPII variant referred to as R-GEPII 1.0, by exchanging the donor FP, mseCFP, for the GFP variant Clover, and the FRET-acceptor, cpV, for mRuby2 (**Figure 22d**). Also this probe was tested for its functionality in permeabilized cells upon administration of increasing $[K^+]$ (**Figure 22e**). Interestingly, the sensitivity of GEPII 1.0 for K^+ *in situ* was decreased to 0.8186 mM (0.7209 mM – 0.9296 mM) (**Figure 22f** and **Appendix Table 1**) in comparison to the sensitivity determined *in vitro* (EC_{50}=0.4171 mM, **Figure 14e**) (217). The EC_{50} of R-GEPII 1.0 was elevated in comparison to GEPII 1.0, to 3.253 mM (2.825 mM – 3.745 mM) (**Figure 22f** and **Appendix Table 2**). However, due to the reduced dynamic range of R-GEPII 1.0 (**Figure 22e**) in comparison to GEPII 1.0 (**Figure 22b**), we proceeded our experiments using the CFP/ YFP based probe.

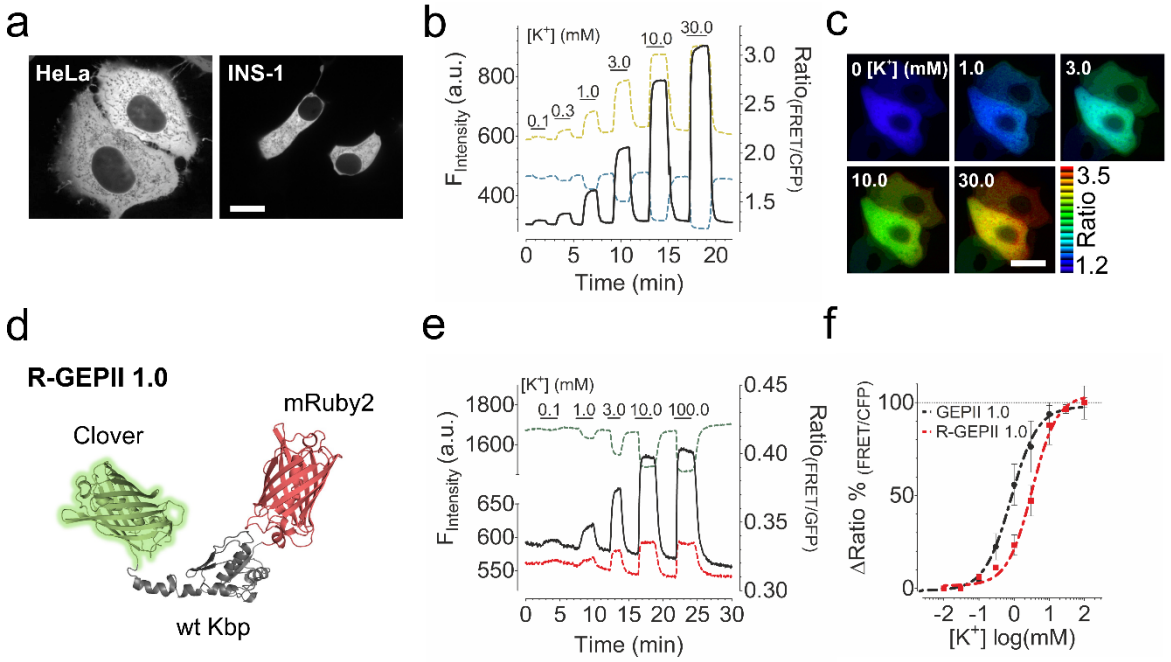

Figure 22: Testing the functionality of GEPII 1.0 and R-GEPII 1.0 *in situ*. (**a**) Representative array confocal laser microscopy (ACLSM) images of HeLa (left image) and INS-1 cells (right image) expressing cytosolic GEPII 1.0. Scale bar represents 10 µm. (**b**) Representative response of digitonin treated HeLa cells perfused in the absence of $[K^+]_{ex}$. At the time points indicated, increasing concentrations of K^+ were administered and removed from the cells using a gravity-based perfusion system. Fluorescence curve of circularly permuted Venus (cpV, yellow dashed line) and monomeric super enhanced CFP (mseCFP, blue dashed line) as well as FRET-ratio signal over time (black solid line) are demonstrated. (**c**) Pseudo-colored FRET-ratio images of HeLa cells expressing cytosolic GEPII 1.0. Cells were permeabilized with digitonin. Pseudo-colored FRET-ratio images upon application of increasing extracellular $[K^+]$ are shown. Scale bar in the lower left image represents 10 µm. (**d**) Schematic representation of R-GEPII 1.0 containing wild type Kbp (wt Kbp, grey) fused to a N-terminal GFP-variant, Clover, and a C-terminal RFP-variant, mRuby2. (**e**) Representative response of gramicidin treated HeLa cells perfused in the absence of $[K^+]_{ex}$. At the time points indicated, increasing concentrations of K^+ were administered and removed from the cells using a gravity-based perfusion system. Fluorescence curve of Clover (green dashed line) and mRuby2 (red dashed line) as well as FRET-ratio signal over time (black solid line) are demonstrated. (**f**) Normalized EC_{50} curves of GEPII 1.0 and R-GEPII 1.0 *in situ*. Data represents average ± SD, n=6 for GEPII 1.0, n=3 for R-GEPII 1.0. Reproduced from Bischof et al., 2017 with permission of publisher Nature Communications (217).

Since K^+ alterations are mostly associated with Na^+ fluctuations within living cells (244), we aimed to elucidate whether Na^+ might potentially affect the K^+ sensing ability of GEPII 1.0 *in situ*. Cells expressing GEPII 1.0 were permeabilized and analyzed in response to a given concentration of K^+ at different intra- (**Figure 23a**) or extracellular (**Figure 23b**) physiologically relevant Na^+ concentrations ($[Na^+]$). This experiments pointed to the independence of physiological intra- and extracellular Na^+ alterations when K^+ is measured using GEPII 1.0 (**Figure 23a** and **23b**) (217).

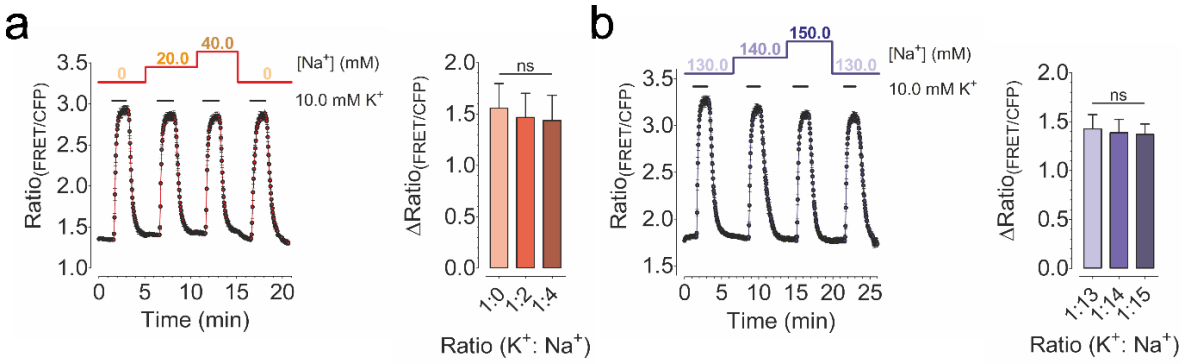

Figure 23: Effects of intra- and extracellular Na^+ concentrations on K^+ sensing with GEPII 1.0. (**a**) HeLa cells expressing GEPII 1.0 were pre-treated with digitonin, valinomycin and monensin for cell permeabilization. FRET-ratio signals over time in the presence of different intracellular relevant [Na^+] ranging from 0 – 40.0 mM were recorded in response to 10 mM K^+. Buffers were exchanged using a gravity based perfusion system (left panel). Maximally received ΔFRET-ratio signals at different [Na^+] were then analyzed and compared (right panel). All data represent average ± SD, n=4, one-way ANOVA test with Tukey's multiple comparison test. (**b**) HeLa cells expressing GEPII 1.0 were pre-treated with digitonin, valinomycin and monensin for cell permeabilization. FRET-ratio signals over time in the presence of different extracellular relevant [Na^+] ranging from 130.0 – 150.0 mM were recorded in response to 10 mM K^+. Buffers were exchanged using a gravity based perfusion system (left panel). Maximally received ΔFRET-ratio signals at different [Na^+] were then analyzed and compared (right panel). All data represent average ± SD, n=3, one-way ANOVA test with Tukey's multiple comparison test. Reproduced from Bischof et al., 2017 with permission of publisher Nature Communications (217).

4.5 The sensitivity of GEPII 1.0 is dependent on acidic amino acids and on the steric interaction of the BON and LysM domain within Kbp

The intracellular K^+ concentration is assumed to be close around 140 mM (1,43). However, as GEPII 1.0 is already saturated at around one third of this concentration, we further aimed to reduce the K^+ sensitivity, without affecting the specificity of GEPIIs. First, we hypothesized that within Kbp, negatively charged residues of amino acids might be responsible for K^+ binding (217). Thus, we replaced all acidic amino acids within the BON domain, representing the actual K^+ binding pocket (226), with their corresponding amides, and named the resulting construct low-charge BON (lc-BON) GEPII 1.0 (**Figure 24a**). To test the variant for its K^+ sensing ability, the recombinant protein of lc-BON GEPII 1.0 was exposed to increasing concentrations of K^+ (**Figure 24b** and **24c** and **Appendix Table 1**). These experiments demonstrated, that a replacement of all acidic amino acids within the BON domain yielded a K^+ insensitive variant. Importantly, the probe was also insensitive to other ions including Ca^{2+}, Cs^{2+}, Na^+, NH_4^+, and Rb^+ (**Figure 24c** and **Appendix Table 1**) (217).

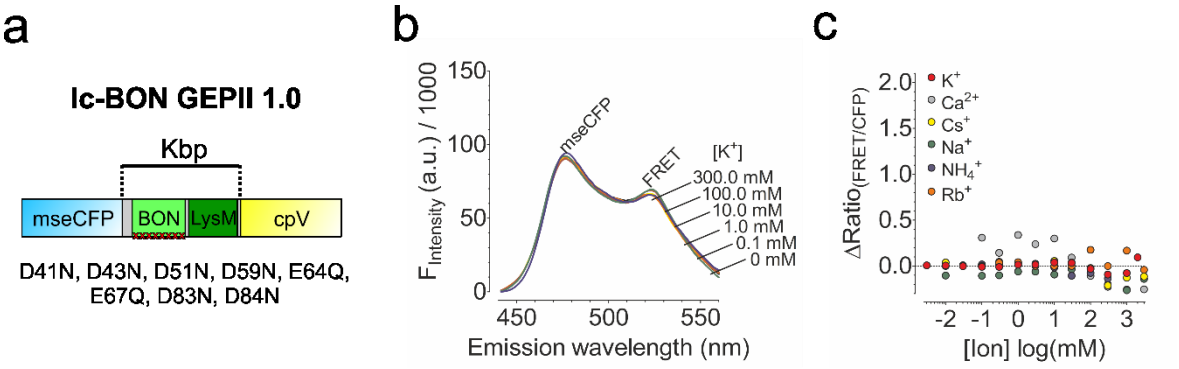

Figure 24: Design and characterization of Ic-BON GEPII 1.0 *in vitro.* (**a**) Schematic representation of Ic-BON GEPII 1.0. The N-terminal monomeric super enhanced CFP (mseCFP, cyan) and the C-terminal circularly permuted Venus (cpV) flank a mutated Kbp (grey, light green and dark green). Point mutations introduced and their position within the Kbp of Ic-BON GEPII 1.0 are shown. (**b**) *In vitro* fluorescence emission spectra of Ic-BON GEPII 1.0 at different [K^+]. (**c**) Concentration response demonstration of Ic-BON GEPII 1.0 in response to increasing concentrations of K^+ (red circles), Ca^{2+} (grey circles), Cs^+ (yellow circles), Na^+ (green circles), NH_4^+ (blue circles) and Rb^+ (orange circles). Data represents average ± SEM, n=2 for each ion and concentration. Reproduced from Bischof et al., 2017 with permission of publisher Nature Communications (217).

Having identified that the K^+ sensitivity of GEPIIs can be shifted by inserting mutations within Kbp, we speculated that the generation of a variant lacking all acidic amino acids within the LysM domain will also show reduced affinity for K^+ (**Figure 25a**). We referred to the construct as low-charge LysM (lc-LysM) GEPII 1.0 (**Figure 25a**), purified the recombinant protein and added increasing [K^+] to the protein (**Figure 25b** and **25c**) (217). These experiments unveiled concentration dependent alterations of the fluorescence emission spectrum of lc-LysM GEPII 1.0, where FRET fluorescence was rising, i.e. mseCFP fluorescence decreasing with increasing [K^+] (**Figure 25b**). The EC_{50} of lc-LysM GEPII 1.0 for K^+ in vitro was found to be 27.53 mM (24.38 mM – 30.87 mM) (**Figure 25c** and **Appendix Table 1**) with a hill slope of 1.090 ± 0.061 (**Figure 25d** and **Appendix Table 1**), indicating that the insertion of mutations did not change the binding stoichiometry of Kbp (217). Similar to GEPII 1.0 the construct showed a thermo-sensitive binding behavior, as the EC_{50} was increasing with increasing temperature (**Figure 25e** and **25f**). However, the probe kept its specificity for K^+ over all other ions and turned out to be even more specific for K^+ in comparison to GEPII 1.0, as only Rb^+ increased the FRET-ratio signal of lc-LysM GEPII 1.0 with an EC_{50} of 42.58 mM (35.01 mM – 51.79 mM) (**Figure 25g** and **Appendix Table 1**). These experiments pointed to the high specificity of the novel, low K^+ sensitive GEPII variant, lc-LysM GEPII 1.0 (217).

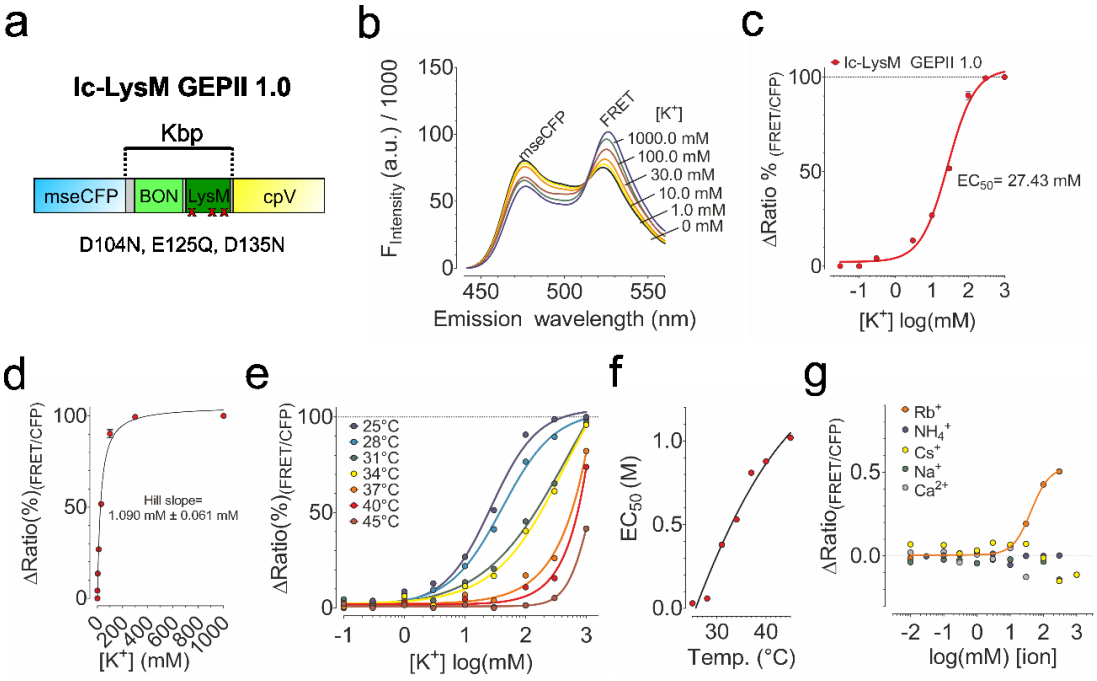

Figure 25: Design and *in vitro* characterization of Ic-LysM GEPII 1.0. (**a**) Schematic representation of Ic-LysM GEPII 1.0 composed of a N-terminal monomeric super enhanced CFP (mseCFP, cyan) and a C-terminal circularly permuted Venus (cpV). The two fluorescent proteins flank a mutated Kbp (grey, light green and dark green). Point mutations introduced and their position within the Kbp of Ic-LysM GEPII 1.0 are shown. (**b**) Fluorescence emission spectra of Ic-LysM GEPII 1.0 in the presence of increasing [K^+]. (**c**) Normalized *in vitro* EC_{50} curve of Ic-LysM GEPII 1.0 for K^+. Data represents average ± SD, n=4. (**d**) Normalized K^+ binding kinetic of Ic-LysM GEPII 1.0 using binding-saturation fit. Hill slope and 95% confidence interval is indicated, data represents average ± SD, n=4. (**e**) Normalized EC_{50} curves of Ic-LysM GEPII 1.0 for K^+ at different temperatures ranging from 25 °C (dark blue line) to 45 °C (dark red line). Data shows average ± SD, n=6). (**f**) Respective EC_{50} values of Ic-LysM GEPII 1.0 as determined in (**e**) plotted over temperature. (**g**) Ion selectivity of Ic-LysM GEPII 1.0 for Rb^+ (orange line and circles), NH_4^+ (blue line and circles), Cs^+ (yellow line and circles), Na^+ (green line and circles) and Ca^{2+} (grey line and circles). Average ± SD is indicated, n=3 for each ion and concentration. Reproduced from Bischof et al., 2017 with permission of publisher Nature Communications (217).

Furthermore, we hypothesized that the introduction of linkers of variable lengths between the BON and LysM domain might also result in variants having lower K^+ sensitivity by impeding their interaction (**Figure 26a – 26c**). Also these mutated constructs, referred to as GEPII 2.7 (**Figure 26a**), GEPII 2.10 (**Figure 26b**) and GEPII 2.15 (**Figure 26c**) showed lower affinity for K^+ in comparison to GEPII 1.0, with EC_{50} values of 3.24 mM (2.96 mM – 3.55 mM), 4.39 mM (4.01 mM – 4.80 mM) and 8.59 mM (7.70 mM – 9.58 mM) *in vitro* at 25 °C, respectively (**Figure 26d** and **Appendix Table 3**) (217). Analysis of the binding kinetics unveiled, however, hill slopes close to 1 for all constructs (**Figure 26e – 26g** and **Appendix Table 3**), indicating that all of these variants bind K^+ in a non-cooperative manner and that one protein of Kbp binds one K^+ (217).

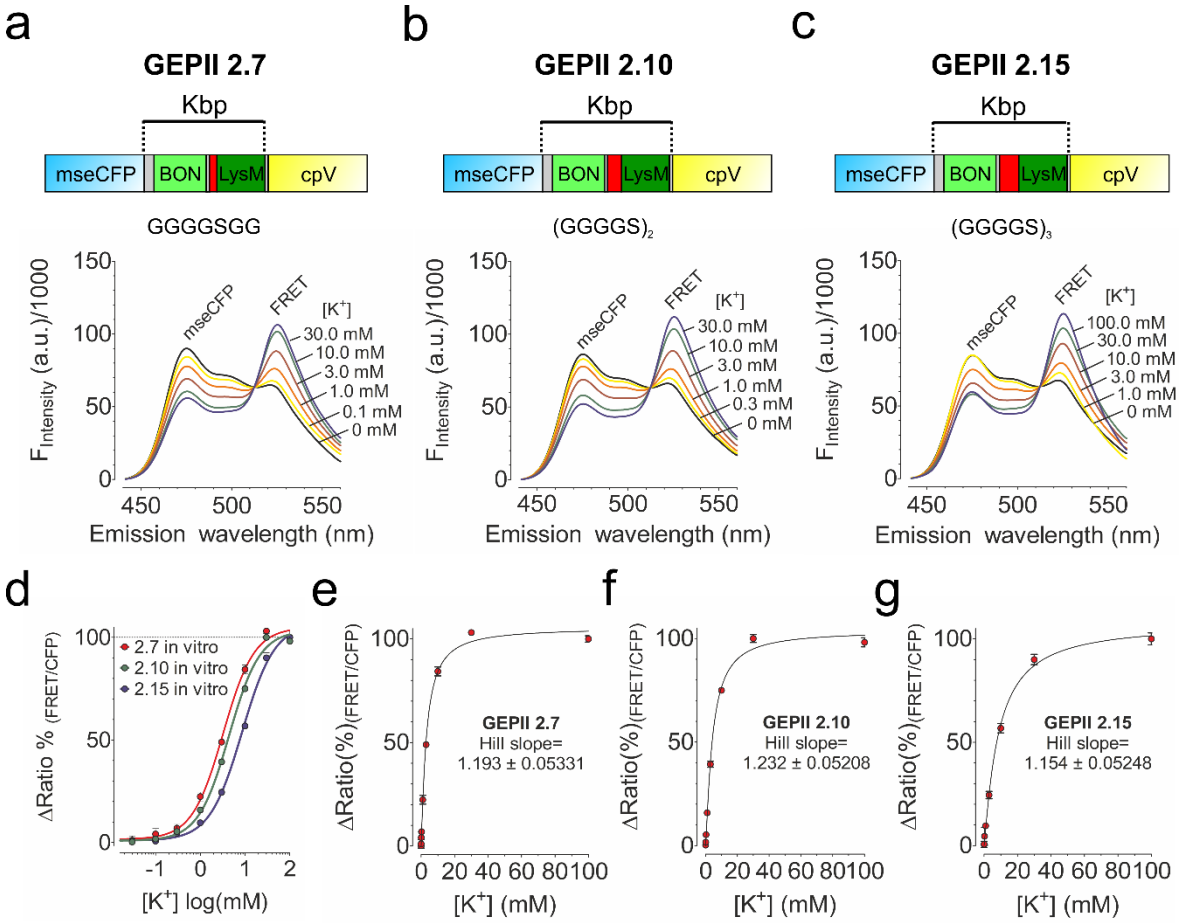

Figure 26: Design and *in vitro* characterisation of GEPII 2.7, GEPII 2.10 and GEPII 2.15. (**a-c**) Upper panels show schematic representations of GEPII 2.7, GEPII 2.10 and GEPII 2.15, composed of a N-terminal monomeric super enhanced CFP (mseCFP, cyan) and a C-terminal circularly permuted Venus (cpV). The two fluorescent proteins flank mutated Kbps (grey, light green and dark green) containing inter-domain linkers of 7, 10 and 15 amino acids between the BON and LysM domain, respectively. Sequences of the introduced linkers are given. Lower panels demonstrate respective fluorescence emission spectra of GEPII 2.7, GEPII 2.10 and GEPII 2.15 at different [K^+], respectively. (**d**) Normalized EC_{50} curves of GEPII 2.7 (red circles and curve), GEPII 2.10 (green circles and curve) and GEPII 2.15 (blue circles and curve) for K^+ *in vitro*. Data represents average ± SD, n=4 for each construct and [K^+]. (**e-f**) Normalized K^+ binding kinetics of GEPII 2.7, GEPII 2.10 and GEPII 2.15 using binding-saturation fit. Hill slopes and 95% confidence intervals for each construct is indicated, respectively. Data represents average ± SD, n=4. Reproduced from Bischof et al., 2017 with permission of publisher Nature Communications (217).

4.6 Characterization of mutated GEPII variants within single living cells

Having characterized the novel GEPII variants *in vitro*, we further aimed to apply them *in situ* for the quantification of (sub-) cellular K^+ concentrations and dynamics. To address these objectives, we decided to use our novel generated construct referred to as lc-LysM GEPII 1.0, having the highest apparent K_D, which seemed the most promising variant for the visualization of physiologic intracellular K^+ concentrations. Similar to the experiments performed with GEPII 1.0, we expressed cytosolic lc-LysM GEPII 1.0 in HeLa cells (**Figure 27a**), pre-permeabilized the cells using gramicidin or digitonin and administered increasing $[K^+]_{ex}$ to the cells (**Figure 27b**) (217).

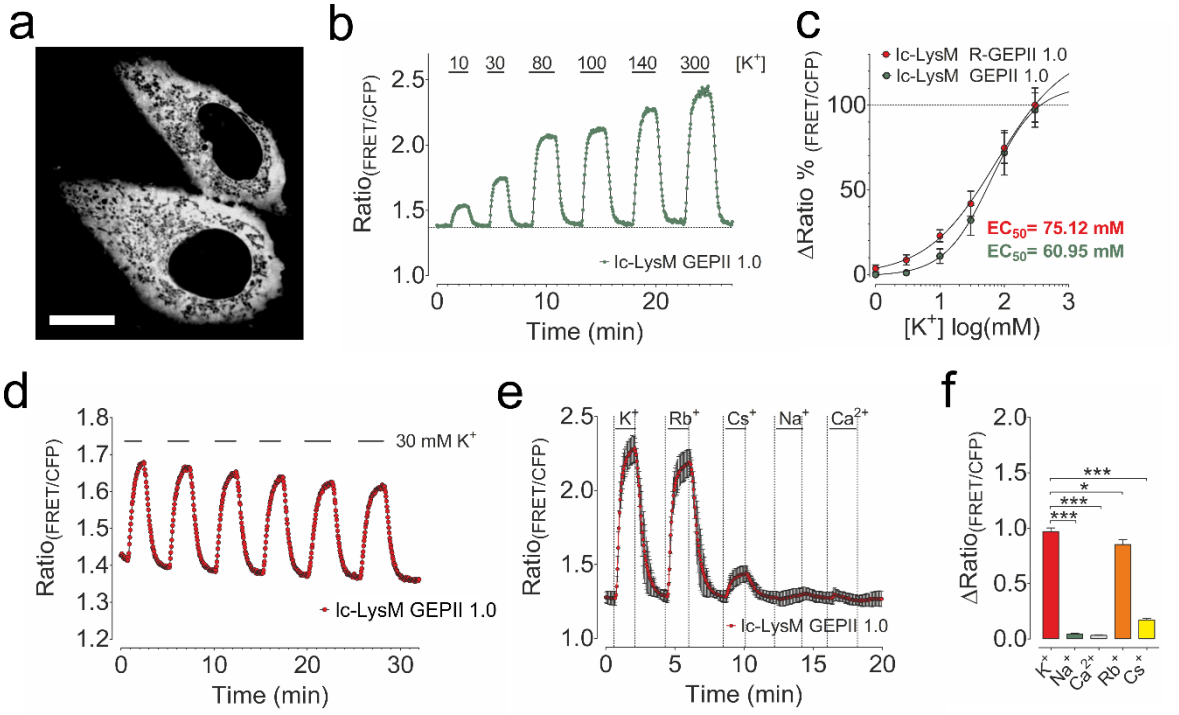

Figure 27: *In situ* characterization of lc-LysM GEPIIs. (**a**) Representative array confocal laser scanning microscopy (ACLSM) image of HeLa cells expressing cytosolic lc-LysM GEPII 1.0. Scale bar represents 10 µm. (**b**) Representative FRET-ratio signal of a gramicidin treated HeLa cell expressing lc-LysM GEPII 1.0, perfused in the absence of $[K^+]_{ex}$. At the time points indicated, increasing concentrations of K^+ were administered and removed from the cells using a gravity-based perfusion system. (**c**) Normalized EC_{50} curves of lc-LysM GEPII 1.0 (green circles and EC_{50} value written in green) and lc-LysM R-GEPII 1.0 (red circles and EC_{50} value written in red), containing the green fluorescent protein variant Clover and the red fluorescent protein variant mRuby2 instead of mseCFP and cpV, respectively, determined in HeLa cells. Data represents average ± SD, n=6 for lc-LysM GEPII 1.0, n=3 for lc-LysM R-GEPII 1.0. (**d**) Representative single cell response of a HeLa cells expressing lc-LysM GEPII 1.0, permeabilized with gramicidin. At the time points indicated, buffers either containing 0 mM K^+ or 30.0 mM K^+ were administrated to the cells (**e**) HeLa cells were permeabilized with digitonin, monensin and valinomicin. After cell treatment, 140 mM K^+, 140 mM Rb^+, 140 mM Cs^+, 140mM of Na^+ or 90 mM of Ca^{2+} were administrated to the cells. Data represents average ± SEM, n=3. (**f**) Analysis of the maximum ΔFRET-ratio signals upon administration of different ions as demonstrated in (**e**). Bars represent average ± SEM, n=3, *p<0.05, ***p<0.0005, one-way ANOVA test with Tukey's multiple comparison test. Reproduced from Bischof et al., 2017 with permission of publisher Nature Communications (217).

Respective FRET-ratio signals were then blotted over [K^+] to estimate the EC_{50} of the probe *in situ* (**Figure 27c**). Interestingly, also the EC_{50} of lc-LysM GEPII 1.0 was drastically increased when expressed in cells to 60.95 mM (45.52 mM – 81.62 mM) (**Figure 27c** and **Appendix Table 1**) (217). In analogy to R-GEPII 1.0, we generated a construct containing Clover and mRuby2 flanking lc-LysM Kbp and referred to the construct as lc-LysM R-GEPII 1.0. EC_{50} of lc-LysM R-GEPII 1.0 was found to be 75.12 mM (35.05 mM – 161.0 mM) (**Figure 27c** and **Appendix Table 2**). lc-LysM GEPII 1.0 responded repetitively and reversibly over time to the administration or removal of K^+, indicating that the probe is suitable for dynamic long time imaging of K^+ alterations *in situ* (**Figure 27d**) (217). The selectivity of lc-LysM GEPII 1.0 *in situ* was tested in pre-permeabilized cells upon administration of 140 mM K^+, Rb^+, Cs^+ and Na^+ or 90 mM of Ca^{2+}, respectively (**Figure 27e** and **27f**), and was comparable to experiments performed *in vitro* (**Figure 25g**) (217).

To test whether also lc-BON GEPII 1.0 shows a similar behavior *in situ*, the variant was expressed in HeLa cells. Upon cell permeabilization, 140 mM of K^+, Rb^+, Cs^+, Na^+ or 90 mM of Ca^{2+} were administered to the cells (**Figure 28a and 28b**). Importantly, none of these ions and concentrations tested increased the FRET-ratio signal of lc-BON GEPII 1.0 (**Figure 28a and 28b**). These experiments pointed to the insensitivity of lc-BON GEPII 1.0 to various ions being physiologically important or having a similar size and charge as K^+.

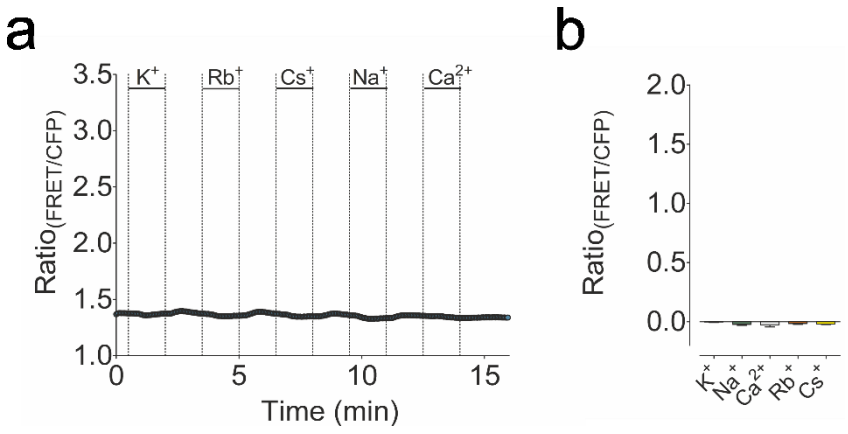

Figure 28: Characterization of lc-BON GEPII 1.0 *in situ*. (**a**) HeLa cells were permeabilized with digitonin, monensin and valinomicin. After cell treatment, 140 mM K^+, 140 mM Rb^+, 140 mM Cs^+, 140mM of Na^+ or 90 mM Ca^{2+} were administrated to the cells. Data represents average ± SEM, n=3. (**b**) Analysis of the maximum ΔFRET-ratio signals upon administration of different ions as demonstrated in (**a**). Bars represent average ± SEM, n=3, one-way ANOVA test with Tukey's multiple comparison test.

4.7 Application of GEPIIs *in situ*

4.7.1 Application of lc-LysM GEPII 1.0 for the online visualization of $[K^+]_i$ upon cell permeabilization

Based on the characterization of lc-LysM GEPII *in situ*, we exploited the probe for the dynamic visualization of cell death over-time in response to a necrotic stimulus using digitonin or gramicidin. After expression of lc-LysM GEPII 1.0 in HeLa cells, necrotic stimuli were applied to the cells using a gravity based perfusion system. As expected, application of digitonin (**Figure 29a**) as well as gramicidin (**Figure 29b**) rapidly and drastically reduced intracellular $[K^+]$ indicating cell death. These results pointed to the suitability of digitonin and gramicidin, a prominent K^+ selective pore forming peptide, to rapidly manipulate intracellular $[K^+]$. Additionally, these experiments demonstrated the suitability of lc-LysM GEPII 1.0 for the dynamic visualization of $[K^+]_i$ (217).

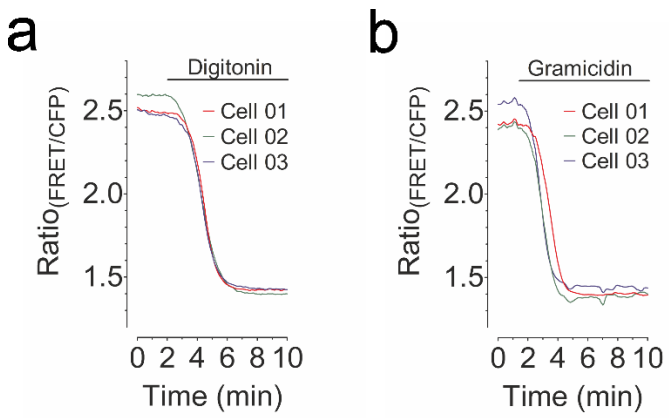

Figure 29: Online visualization of intracellular K^+ fluctuations upon cell permeabilization. (**a**) Representative responses of 3 HeLa cells expressing lc-LysM GEPII 1.0 treated with 5 µM digitonin at the time point indicated in the panel. During the measurements cells were perfused in the absence of extracellular K^+ using a gravity based perfusion system (n=4). (**b**) Representative responses of 3 HeLa cells expressing lc-LysM GEPII 1.0 treated with 10 µM gramicidin at the time point indicated in the panel. During the measurements cells were perfused in the absence of extracellular K^+ using a gravity based perfusion system (n=4). Reproduced from Bischof et al., 2017 with permission of publisher Nature Communications (217).

4.7.2 Quantification of subcellular [K^+] using targeted GEPIIs

Besides the expression of cytosolic GEPIIs, we generated constructs without targeting sequence, localizing in both, the nucleus and cytosol of cells, as well as constructs localizing in nucleus and mitochondria of single living cells **(Figure 30a**). Basal FRET-ratio signals of intact HeLa cells of different GEPIIs were recorded (**Figure 28b – 28d**). While the average FRET- ratio signals of the insensitive variant lc-BON GEPII 1.0 remained unaffected by the targeting (**Figure 28b**), GEPII 1.0 (**Figure 28c**) and lc-LysM GEPII 1.0 (**Figure 28d**) reported organelle-specific differences depending on their subcellular localizations (217).

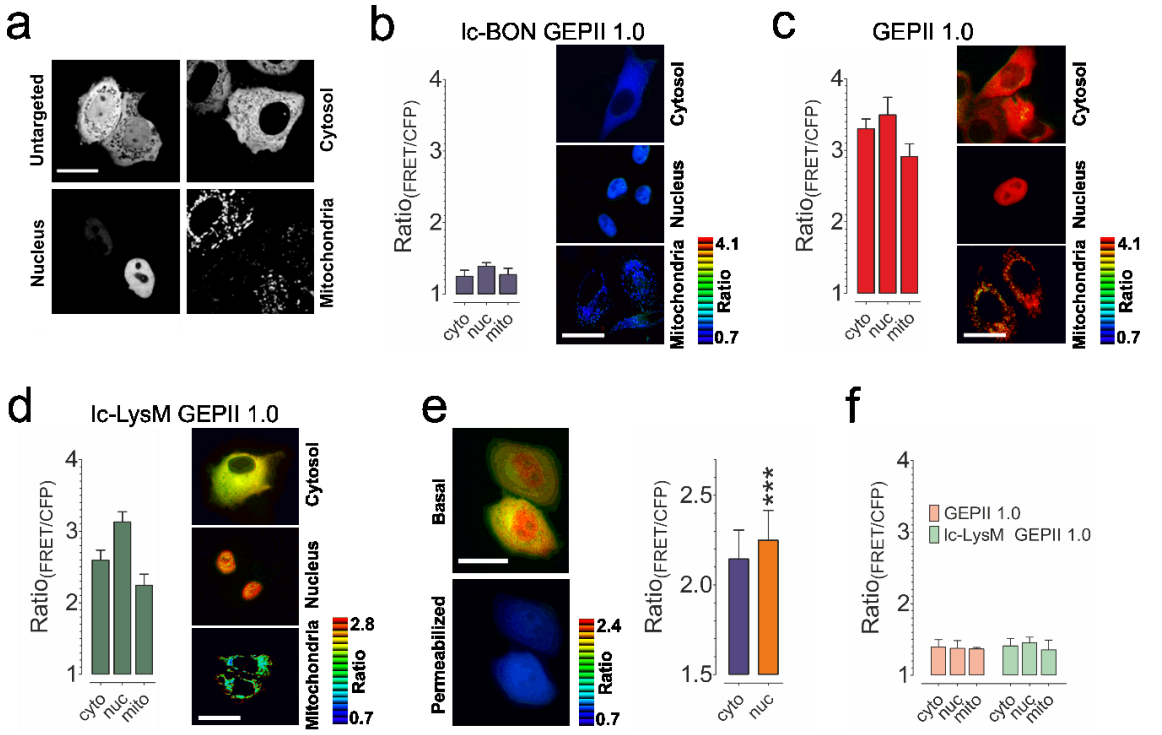

Figure 30: Targeting of GEPIIs to subcellular localizations. (**a**) Representative array confocal laser scanning microscopy (ACLSM) images of HeLa cells expressing either untargeted, cytosolic, nuclear or mitochondrial targeted GEPII 1.0. Scale bar in the upper left image represents 20 µm. (**b**) Basal FRET-ratio values (left panel) and pseudo-colored FRET-ratio images (right panel) of HeLa cells expressing lc-BON GEPII 1.0 either in the cytosol (cyto), the nucleus (nuc) or the mitochondria (mito). Scale bar represents 20 µm. Bars in the left panel represent average ± SD, n=5. (**c**) Basal FRET-ratio values (left panel, average ± SD, n=3) and pseudo-colored FRET-ratio images (right panel) of HeLa cells expressing GEPII 1.0 either in the cytosol (cyto), the nucleus (nuc) or the mitochondria (mito). Scale bar represents 20 µm. (**d**) Basal FRET-ratio values (left panel, average ± SD, n=6) and pseudo-colored FRET-ratio images (right panel) of HeLa cells expressing lc-LysM GEPII 1.0 either in the cytosol (cyto), the nucleus (nuc) or the mitochondria (mito). Scale bar represents 20 µm. (**e**) Left panel demonstrates representative pseudo-colored FRET-ratio images of HeLa cells expressing untargeted lc-LysM GEPII 1.0 either under basal conditions (upper image) or after cell permeabilization using 5 µM digitonin (lower image). Right panel shows the corresponding statistics of the FRET-ratio signal recorded in single cells either within the cytosol (cyto, blue bar) or the nucleus (nuc, orange bar). Data represents average ± SD, n=5, ***p<0.0001, paired t-test. (**f**) FRET-ratio signals of digitonin permeabilized HeLa cells expressing GEPII 1.0 (light orange bars, n=3 for each bar) or lc-LysM GEPII 1.0 (light green bars, n=6 for each bar), both either targeted to the cytosol (cyto), the nucleus (nuc) or the mitochondria (mito). Data represents average ± SD. Reproduced from Bischof et al., 2017 with permission of publisher Nature Communications (217).

FRET-ratio signal differences were more prominent in case of lc-LysM GEPII 1.0 (**Figure 28c**), due to the higher K_D for K^+. Highest FRET-ratio values were thereby measured in the nucleus, lowest ratio values within mitochondria (**Figure 28d**). These differences in FRET-ratio values between the cytosol and nucleus were also observed using untargeted lc-LysM GEPII, localizing in the cytosol and nucleus (**Figure 28e**). However, all localization specific differences of GEPII 1.0 and lc-LysM GEPII 1.0 were equalized by cell permeabilization (**Figure 28f**), indicating that the targeting of GEPIIs did not cause any significant artefacts (217).

Next, we aimed to quantify $[K^+]_i$ within different subcellular compartments of INS-1, HeLa, HEK293a and Ea.hy926 cells. (**Figure 31a**). These experiments revealed higher $[K^+]$ within the nuclei than within the cytosol of all cell lines tested (**Figure 31a**). Interestingly, these differences were most pronounced in Ea.hy926 cells, with a nuclear $[K^+]$ ($[K^+]_{nuc}$)/cytosolic $[K^+]$ ($[K^+]_{cyto}$) ratio of 3.77, while being lower in HeLa ($[K^+]_{nuc}/[K^+]_{cyto}$=3.38), HEK293a (2.39) and INS-1 (1.94) cells (**Figure 31b**) (217). Vice versa, the mitochondria of all cell lines showed a lower $[K^+]$ in comparison to the cytosol (**Figure 31a**), with mitochondrial $[K^+]$ ($[K^+]_{mito}$)/$[K^+]_{cyto}$ ratios of 0.78, 0.49, 0.65 and 0.42 in Ea.hy926, HeLa, HEK293a and INS-1 cells, respectively (**Figure 31c**) (217).

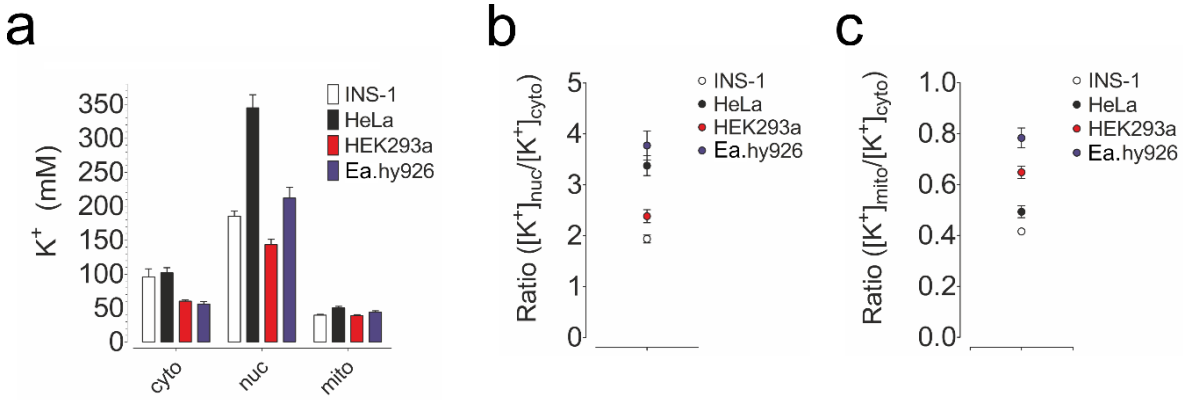

Figure 31: Quantification of subcellular $[K^+]$ within the organelles of single living INS-1, HeLa, HEK293a and Ea.hy926 cells. (**a**) Basal $[K^+]$ ± SEM of INS-1 (white bars), HeLa (black bars), HEK293a (red bars) and Ea.hy926 cells (blue bars) expressing lc-LysM GEPII 1.0 targeted to the cytosol (cyto), the nucleus (nuc) or the mitochondria (mito), respectively. N=7 independent experiments for all cells and all localizations. (**b**) Nuclear $[K^+]$/Cytosolic $[K^+]$ ($[K^+]_{nuc}/[K^+]_{cyto}$) ratios of INS-1 (white circle), HeLa (black circle), HEK293a (red circle) and Ea.hy926 cells (blue circle). Data were calculated from the data represented in (**a**) and shows average ± SEM. (**c**) Mitochondrial $[K^+]$/Cytosolic $[K^+]$ ($[K^+]_{mito}/[K^+]_{cyto}$) ratios of INS-1 (white circle), HeLa (black circle), HEK293a (red circle) and Ea.hy926 cells (blue circle). Data were calculated from the data represented in (**a**) and shows average ± SEM. Reproduced from Bischof et al., 2017 with permission of publisher Nature Communications (217).

In order to validate our results of higher nuclear [K⁺], we aimed to target a potential Na⁺/K⁺ ATPase present in the nuclear envelope (**Figure 32a**). For this purpose, we tried to establish a protocol allowing us to visualize a Na⁺/K⁺ ATPase dependent K⁺ uptake into the cytosol and further into the nucleus of cells (**Figure 32a**).

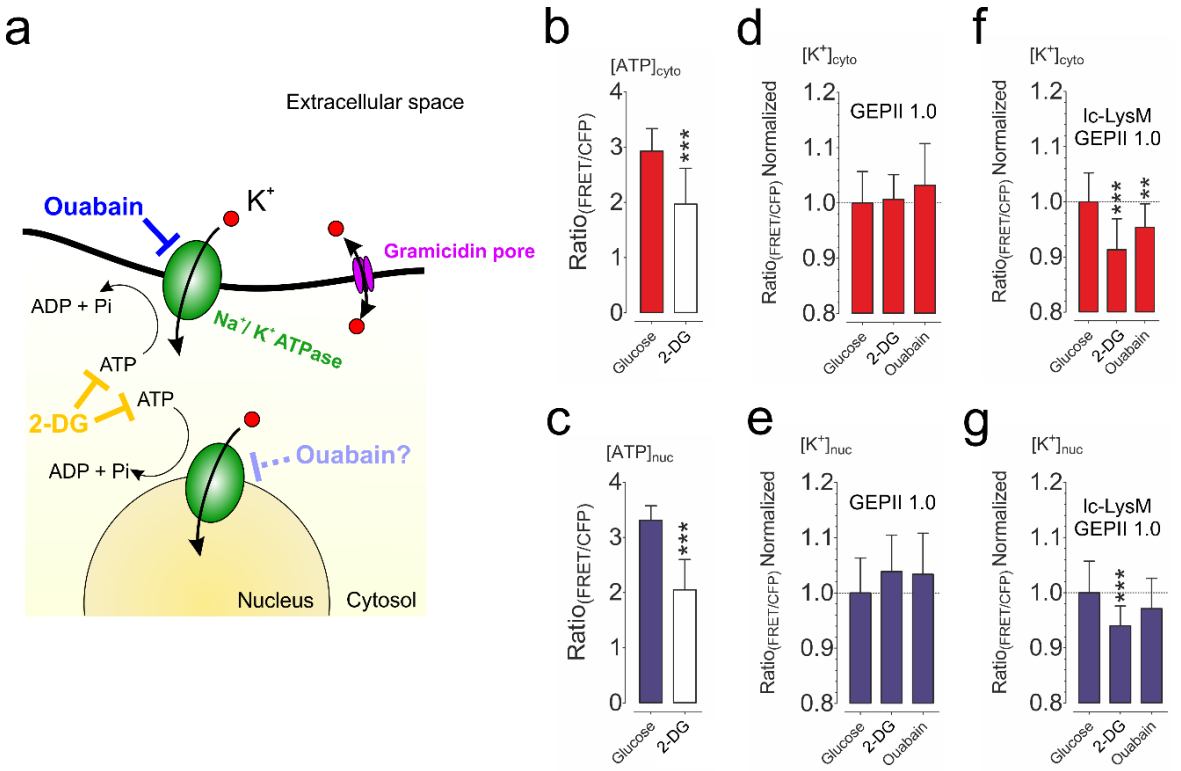

Figure 32: Targeting the active K⁺ transport in the cytosol and nucleus of HeLa cells. (**a**) Schematic representation of a cell with the extracellular space (white), the plasma membrane (thick black line), the cytosol (light yellow) and the nucleus (beige). Na⁺/K⁺ ATPase (green) is located at the plasma membrane and also within the nuclear envelope, and might be responsible for an active K⁺ (red circles) transport upon ATP hydrolysis at both localizations. Gramicidin pores (pink) permeabilize the plasma membrane gradient dependent for K⁺. ouabain (dark blue) administration on cells will block the Na⁺/K⁺ ATPase located within the plasma membrane, and eventually also subcellular located Na⁺/K⁺ ATPases. 2-DG (orange) as a glycolysis inhibitor will block ATP generation within the cell and thus abolish an ATP dependent K⁺ transport. (**b**) Basal ATP levels within the cytosol of control HeLa cells (red bar, Glucose) or cells treated with 2-DG (white bar, 2-DG) upon cell pre-treatment with either 10 mM glucose or 10 mM 2-DG for 30 minutes. Bars represent average ± SD, n=3 for both, ***p<0.0001 using unpaired t-test. (**c**) Basal ATP levels within the nucleus of control HeLa cells (blue bar, Glucose) or cells treated with 2-DG (white bar, 2-DG) upon cell pre-treatment with either 10 mM glucose or 10 mM 2-DG for 30 minutes. Bars represent average ± SD, n=3 for both, ***p<0.0001 using unpaired t-test. (**d,e**) Normalized FRET-ratio values of gramicidin pre-permeabilized HeLa cells expressing either (**d**) cytosolic or nuclear targeted (**e**) GEPII 1.0 upon administration of 140 mM K⁺. Cells were either kept for 30 minutes in the presence of 10 mM glucose (Glucose), 10 mM 2-DG (2-DG) or 1 mM ouabain (Ouabain). Bars represent average ± SD, n=3 for all conditions, statistical analysis was performed using one-way ANOVA test with Tukey's multiple comparison test. (**f,g**) Normalized FRET-ratio values of gramicidin pre-permeabilized HeLa cells expressing either (**f**) cytosolic or nuclear targeted (**g**) lc-LysM GEPII 1.0 upon administration of 140 mM K⁺. Cells were either pretreated for 30 minutes in the presence of 10 mM glucose (Glucose), 10 mM 2-DG (2-DG) or 1 mM ouabain (Ouabain). Bars represent average ± SD, n=5 for all conditions, **p<0.001, ***p<0.0001, one-way ANOVA test with Tukey's multiple comparison test.

Therefore, HeLa cells expressing GEPII 1.0, which is early saturated at high [K^+], and lc-LysM GEPII 1.0, allowing [K^+] measurements above 100 mM, both either targeted to the nucleus or the cytosol, were analyzed, respectively. Cells were permeabilized using gramicidin, kept in the presence of glucose (control), treated with 2-deoxy-glucose (2-DG) for a depletion of intracellular ATP levels (2-DG) (245), or treated cells with ouabain, a prominent inhibitor of Na^+/K^+ ATPase (246). As expected, cell treatment with 2-DG treatment drastically reduced intracellular ATP concentration ([ATP]) in the cytosol (**Figure 32b**) as well as in the nuclei of HeLa cells (**Figure 32c**). Upon administration of 140 mM K^+ to pre-permeabilized cells, the FRET-ratio signal of GEPII 1.0 did not report differences depending on the cell treatment in the cytosol (**Figure 32d**) and the nuclei (**Figure 32e**) of HeLa cells. In contrast, cells expressing lc-LysM GEPII 1.0 reported treatment dependent differences in $[K^+]_{nuc}$ (**Figure 32f**) and $[K^+]_{cyto}$ (**Figure 32g**), with significantly reduced $[K^+]_i$ values upon 2-DG treatment in both locals (**Figure 32f** and **32g**). Ouabain treatment, however, only affected $[K^+]_{cyto}$ (**Figure 32f**), while $[K^+]_{nuc}$ remained unchanged (**Figure 32g**). These experiments strongly point to the ability of cells and especially their nucleus to accumulate K^+ in an energy dependent manner, even if cells were permeabilized using gramicidin (**Figure 32a**).

4.7.3 Real-time visualization of cytosolic K^+ transients

To further exploit the GEPII technology, we expressed different GEPIIs in INS-1 cells. To trigger intracellular K^+ alterations in this cells, we depolarized the cells and monitored $[K^+]_{cyto}$ simultaneously with the cytosolic Ca^{2+} concentration ($[Ca^{2+}]_{cyto}$) using the far-red fluorescent, genetically encoded Ca^{2+} indicator CAR-GECO1 (**Figure 33a**) (217,225). As already observed earlier (247), cytosolic $[Ca^{2+}]$ ($[Ca^{2+}]_{cyto}$) drastically increased upon cell depolarization (**Figure 33a**). Shortly delayed upon cellular Ca^{2+} entry, lc-LysM GEPII 1.0 reported a transient reduction of $[K^+]_{cyto}$ within these cells (**Figure 33a** and **33b**) (217).

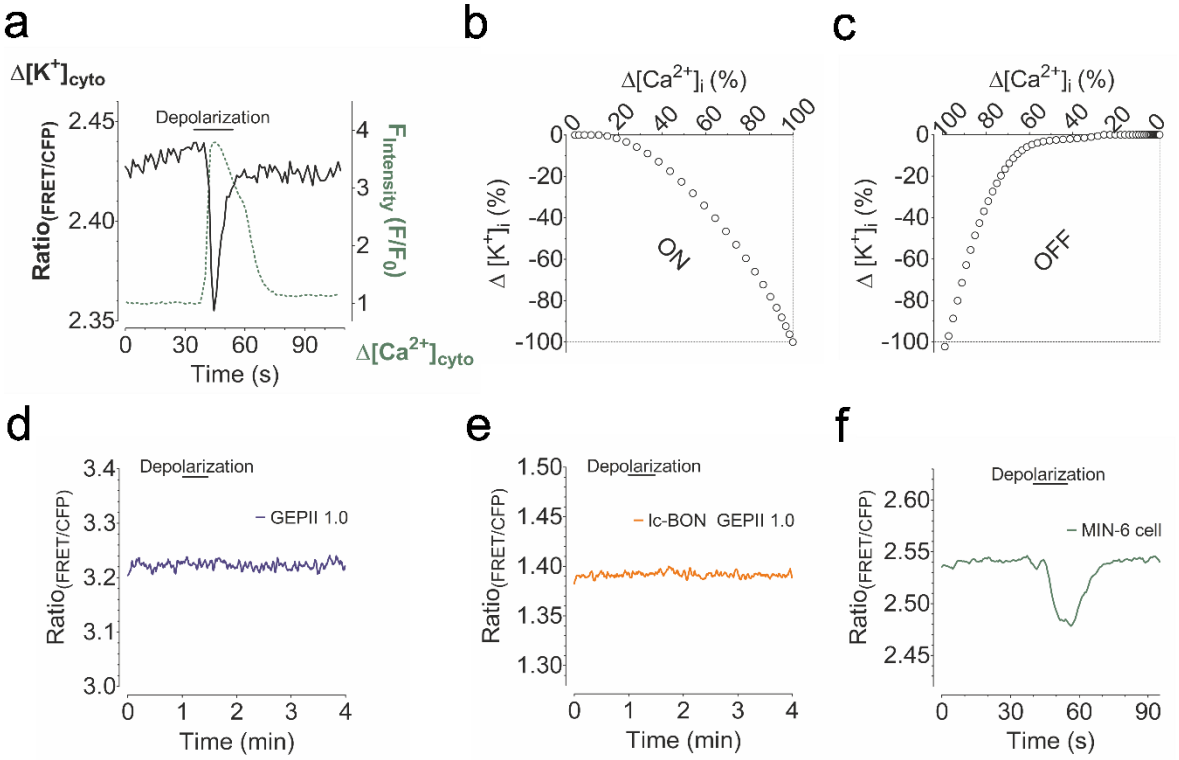

Figure 33: Real-time visualization of cytosolic K^+ transients upon depolarization of in INS-1 cells. (**a**) Representative single cell K^+ (black solid line) and Ca^{2+} (green dashed line) responses of an INS-1 cell expressing cytosolic lc-LysM GEPII 1.0 and CAR-GECO1, a single FP-based, far red fluorescent genetically encoded Ca^{2+} indicator. At the time point indicated, cell was depolarized by the application of 70 mM extracellular K^+ (n=9). On- (**b**) and off kinetics (**c**) of the Ca^{2+} and K^+ signals as shown in (**a**), represented as $\Delta[K^+]_i$ plotted over $\Delta[Ca^{2+}]_i$ in %. Representative single cell response of an INS-1 cell expressing either cytosolic GEPII 1.0 (**d,** n=6) or cytosolic lc-BON GEPII 1.0 (**e,** n=8). Cells were depolarized using 70 mM K^+ at the time points indicated in the panels. (**f**) Representative single cell response of a MIN-6 cell expressing cytosolic lc-LysM GEPII 1.0. Cell was depolarized using 70 mM K^+ at the time point indicated in the panel (n=8). Reproduced from Bischof et al., 2017 with permission of publisher Nature Communications (217).

Vice versa, analysis of the off-kinetics unveiled that $[K^+]_i$ returned to basal levels faster than $[Ca^{2+}]_i$ (**Figure 33c**). However, importantly the FRET-ratio signal of the high K^+ sensitive variant GEPII 1.0 (**Figure 33d**), and the K^+ insensitive variant lc-BON GEPII 1.0 (**Figure 33e**) remained unchanged upon cell depolarization. Additionally, similar results of a transient intracellular K^+ alteration were observed using MIN-6 cells (**Figure 33f**), another rodent pancreatic β-cell line (217).

To further characterize the transient cytosolic K^+ decrease in INS-1 cells, we either unspecifically blocked all K^+ channels using tetraethyl ammonium chloride (TEA) (**Figure 34a**, **34e** and **34f**), replaced extracellular Ca^{2+} with EGTA (**Figure 34b**, **34e** and **34f**), or blocked the L-type Ca^{2+} channels using nifedipine (**Figure 34e** and **34f**) (217). Additionally, we buffered intracellular Ca^{2+} elevations using BAPTA-AM (**Figure 34c – 34f**). All of these treatments significantly reduced the intracellular K^+ transient in response to cell depolarization (**Figure 34e**). Based on these observations we concluded that upon cell depolarization, extracellular Ca^{2+} enters the cell via voltage-gated Ca^{2+} channels which, in turn, activates K^+ channels, leading to a K^+ efflux from the cells (**Figure 34f**) (217).

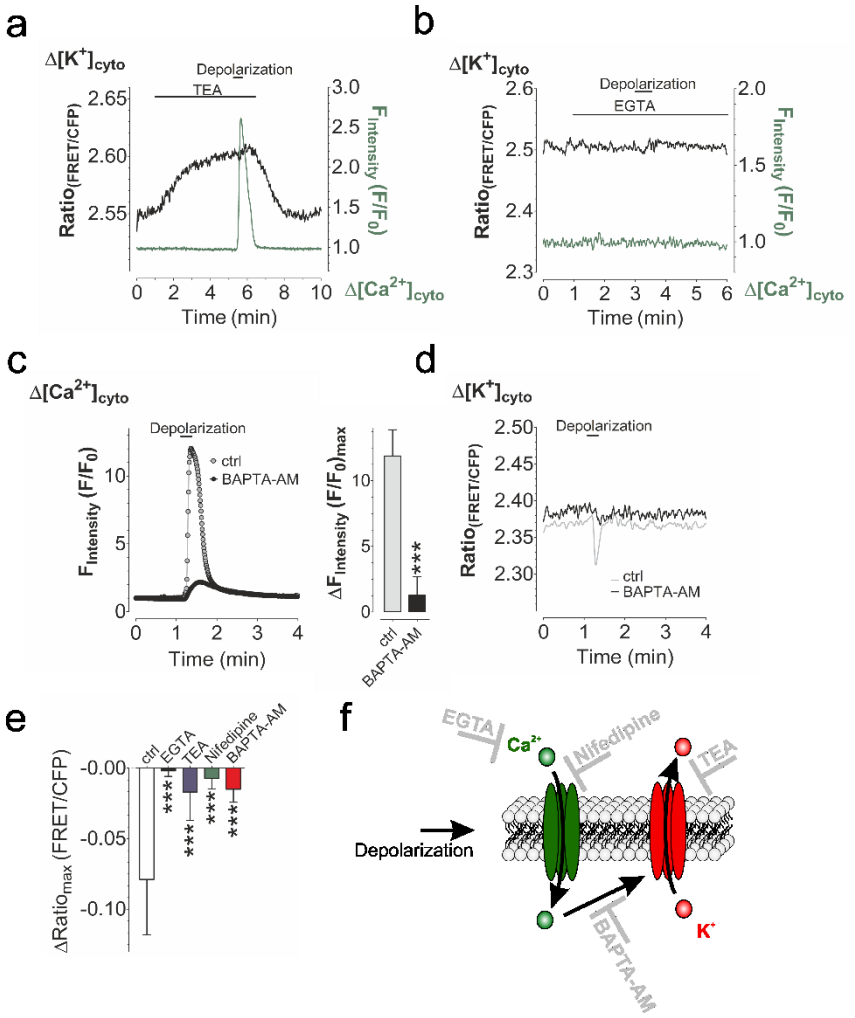

Figure 34: Characterization of the depolarization induced transient of $[K^+]_i$ in INS-1 cells. (**a**) Representative single cell response of an INS-1 cells expressing cytosolic Ic-LysM GEPII 1.0 (black solid line) and CAR-GECO1 (green solid line). Cell depolarization using 70 mM K^+ was performed in the presence of 15 mM tetraethyl ammonium chloride (TEA, n=3). Substances were administrated using a gravity based perfusion system. (**b**) Representative single cell response of an INS-1 cell expressing cytosolic Ic-LysM GEPII 1.0 (black solid line) and CAR-GECO1 (green solid line). Cell depolarization using 70 mM K^+ was performed in the absence of extracellular Ca^{2+} (EGTA, n=7). (**c**) Representative single cell responses of INS-1 cells expressing CAR-GECO1, either loaded with BAPTA-AM (left panel, BAPTA-AM, black circles, n=5) or treated with the same concentration of DMSO (left panel, ctrl, grey circles, n=3) were depolarized using 70 mM K^+ at the time point indicated in the panel. Right panel represents statistical analysis of the corresponding maximal Δfluorescence intensities of cells either loaded with BAPTA-AM (BAPTA-AM, black bar, n=5) or treated with DMSO (ctrl, grey bar, n=3). Data represents average ± SD, ***p<0.0001, unpaired t-test. (**d**) Representative single cell responses of INS-1 cells expressing cytosolic Ic-LysM GEPII 1.0 under the same conditions as shown in (**c**). n=3 for ctrl, n=6 for BAPTA-AM loaded cells. (**e**) Maximal ΔFRET-ratio signals upon cell depolarization using 70 mM K^+ of untreated control cells (ctrl, n=17), in the absence of extracellular Ca^{2+} (EGTA, black bar, n=7), in the presence of 15 mM TEA (TEA, blue bar, n=6), in the presence of 100 µM nifedipine (Nifedipine, green bar, n=6), or of cells loaded with BAPTA-AM (BAPTA-AM, red bar, n=6). Statistical analysis was performed using one-way ANOVA test with Tukey's multiple comparison test, ***p<0.0001. (**f**) Schemata demonstrating the proposed mechanism of action upon cell depolarization and the targets of used pharmacological inhibitors. Reproduced from Bischof et al., 2017 with permission of publisher Nature Communications (217).

4.7.4 Real-time visualization of subcellular K^+ transients

Besides the visualization of $[K^+]_{cyto}$ upon cell depolarization (**Figure 32** and **Figure 33**), we expressed subplasmalemmal-, nuclear- and mitochondrial-targeted Ic-LysM GEPII 1.0 variants in INS-1 cells (**Figure 35a**). While the K^+ transient upon cell depolarization at the inner side of the plasma membrane showed similar kinetics compared tothe cytosol (**Figure 35b**), $[K^+]_{nuc}$ and $[K^+]_{mito}$ were dynamically affected in a completely different manner (**Figure 35b**). $[K^+]_{nuc}$ showed a sustained reduction, while $[K^+]_{mito}$ gradually increased over time in response to cell depolarization (**Figure 35b**) .

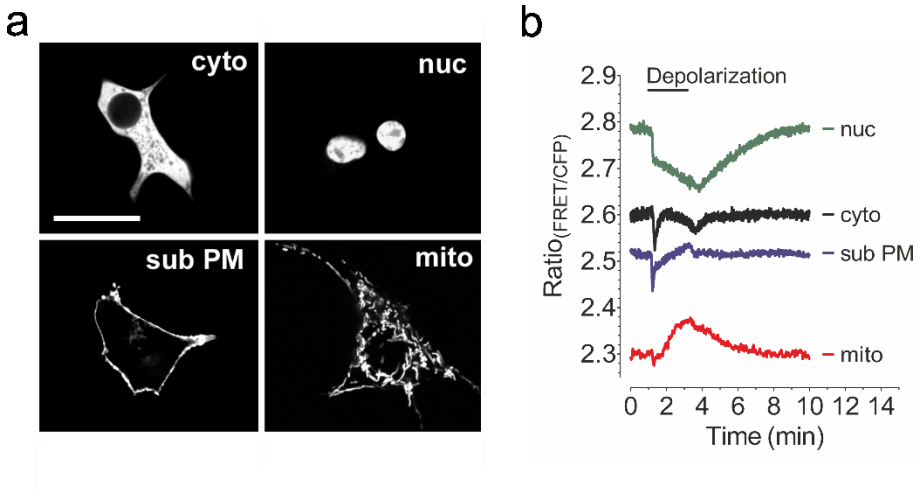

Figure 35: Real-time visualization of subcellular $[K^+]_i$ in INS-1 cells upon cell depolarization. (**a**) Representative array confocal laser scanning microscopy (ACLSM) images (**a**) and single cell responses upon cell depolarization using 70 mM K^+ (**b**) of INS-1 cells expressing either cytosolic- (cyto, (**a**), upper left panel and (**b**), black curve), nuclear- (nuc, (**a**), upper right panel and (**b**), green curve), sub-plasmalemmal- (sub PM, (**a**), lower left panel and (**b**), blue curve) or mitochondrial targeted (mito, (**a**) lower right panel, and (**b**), red curve) Ic-LysM GEPII 1.0, respectively. Scale bar in (**a**), upper left image represents 20 µm. Reproduced from Bischof et al., 2017 with permission of publisher Nature Communications (217).

5 Discussion

Recently, the development of K^+ sensitive fluorescent indicators suitable for the quantification of (sub-)cellular and extracellular [K^+] gained more and more interest. These probes alter their fluorescence in response to K^+ binding and are either based on crown-ethers (248–250) or represent aptamers (251). However, mostly these probes suffer from cytotoxicity, cannot be applied within living cells, are difficult to target to subcellular localizations or cannot be applied *in vivo*.

We addressed the urgent need for applicable protein-based K^+ sensitive probes using a recently characterized bacterial protein, Kbp (226), and developed novel genetically encoded, FRET-based, K^+ sensitive indicators. The design of our genetically encoded potassium ion indicators, the GEPIIs, is analogous to a huge variety of other FRET-based probes such as Ca^{2+} (206,209), glucose (213) or ATP sensors (210). All of these sensors are based on a conformational change of a substrate-specific protein, altering the fluorescence emission spectrum of the probe (214). The huge conformational rearrangement of Kbp, from an elongated towards a roundish conformation upon binding of K^+, was already demonstrated by Ashraf et al. (226). This property of Kbp makes it ideally suited for the design of the GEPIIs. Similar to the study by Ashraf et al., who determined a K_D of Kbp of 160 µM using isothermal titration calorimetry (ITC) (226), GEPII 1.0 containing the wild-type Kbp showed an EC_{50} of 417.1 µM (370 µM – 470 µM) *in vitro* (217). This slightly elevated EC_{50} of Kbp in GEPII 1.0 might be caused by the fusion of FPs to the N- and C-terminus, respectively, aggravating the conformational change of Kbp. Nonetheless, GEPII 1.0 remained specific for K^+ over other ions having a similar size or charge as K^+, which is in line with data by Ashraf et al. (226). Especially the FRET-ratio signal of GEPII 1.0 was not affected by the physiologically relevant Na^+, which is much higher concentrated in the extracellular space than K^+ (1).

Lately, an identical approach of developing genetically encoded K^+ indicators based on Kbp was published (252). The authors generated a CFP/YFP based K^+ sensitive probe, referred to as KIRIN1, by exchanging the donor FP, mseCFP of GEPIIs for mCerulean3, another CFP variant (252). Interestingly, the EC_{50} of KIRIN1 *in vitro* (1.66 ± 0.05 mM) (252) was significantly elevated in comparison to GEPII 1.0 (217).

Considering the high sensitivity of GEPII 1.0 for K^+, we hypothesized that it will not be suitable for the visualization of physiologic intracellular K^+ fluctuations, except K^+ alterations following cell death. The high sensitivity and selectivity of GEPII 1.0, however, seemed promising for the visualization and quantification of $[K^+]_{ex}$. Therefore, we used recombinant GEPII 1.0 as a sensitive method to determine $[K^+]$ within bodily fluids including human and murine plasma, serum, urine and bile samples. Our data demonstrated the suitability of GEPII 1.0 to accurately determine $[K^+]$ within biological samples as precise as the golden standard instruments for clinical diagnostics, the ISE (217). However, standard instruments in clinical diagnostics need quite large sample volumes of several mL, while for $[K^+]$ determinations with GEPIIs 5 µL of sample volume were sufficient (217). The parameter of sample volume is especially critical when working with small laboratory animals such as mice having a blood volume of around 1.5 mL (253). Therefore, GEPIIs can represent a high throughput and low cost alternative allowing repetitive determination of $[K^+]$ within samples of one given animal over time, without the need of its scarification.

Moreover, we utilized recombinant GEPII 1.0 for the online visualization of cell growth and cell death. Our approach demonstrated the suitability of measuring $[K^+]_{ex}$ to visualize cell growth or death of one given population of cells over time (217). Our data emphasized, that in a 96-well plate with a total of ~ 100.000 cells when confluent, already 2.500 dead cells which corresponds to 2.5%, release an amount of K^+ measurable with GEPII 1.0. Simultaneous investigation of cell morphology and $[K^+]_{ex}$ upon application of a necrotic stimulus unveiled a much faster release of K^+ from cells than morphological alterations were visible (217). The establishment of such online cell viability measurement on a conventional fluorescence microscope may allow the visualization of acute single cell death within a population of cells.

Vice versa, we tested the application of GEPII 1.0 for the visualization of cell growth using *E.coli* cultures. Our data demonstrate, that such an approach is feasible using GEPII 1.0, as extracellular $[K^+]$ declined from 10.2 mM to 9.4 mM within 12h of bacterial growth. However, after 12h *E.coli* cells were heated to 75 °C for 1h, which fully restored $[K^+]_{ex}$, indicating that K^+ was in fact incorporated into bacterial cells (217). Thus, using the read-out of $[K^+]_{ex}$ using recombinant GEPII 1.0 was suited to differentiate between vital and dead cells, while a prominent method of staining dead

cells, PI, did only poorly or failed to measure differences between vital cells and cells lysed using different approaches. Our data emphasize that measuring $[K^+]_{ex}$ with GEPII 1.0 in combination with measuring OD_{600} of cultures could represent a valuable approach to estimate the amount of dead and vital cells within cultures (217), without the need of staining agents such as PI, which can be toxic by themselves (254).

Recombinant GEPII 1.0 even proved applicable for *in vivo* imaging using 2-photon excitation. Thereby, the recombinant protein solution of GEPII 1.0, which was diffusing into the tissue, proved stable for at least 30 minutes and enabled dynamic $[K^+]_{ex}$ measurements in living animals (217). Such usage of recombinant GEPII 1.0, or in general, recombinant proteins, will represent fast and reliable alternatives to electrochemical electrodes, which are forced into the animal. In future, the usage of GEPIIs may allow intra-vital microscopy in the extracellular surrounding of excitable cells such as neurons and muscle cells, which will yield a better understanding of cellular trans-membrane K^+ fluctuations *in vivo.* The experimental setup of keeping the prepared tissue for imaging in a water-bath will additionally allow an immediate manipulation of the extracellular fluid to apply pharmacologically active compounds directly to the area of interest *in vivo*.

Importantly, GEPII 1.0 did not only prove applicable as a recombinant protein allowing measurements of extracellular K^+ fluctuations, but even proved functional upon the expression within mammalian cell lines. Calibration of the probe *in situ* unveiled a slightly elevated EC_{50} value of 0.8186 mM in comparison to the calibration *in vitro* (217). Importantly, our experiments performed *in situ* unveiled that physiologically relevant fluctuations of Na^+, which are mostly associated with changes in K^+ (244), do not affect K^+ sensing using GEPII 1.0. For the expression within single living cells we also generated a red-shifted variant containing Clover as a donor FP, and mRuby2 as FRET-acceptor. Upon the exchange of the FRET-pair used in GEPIIs we observed a slight elevation of the EC_{50} to 3.252 mM *in situ*. The exact mechanism how the exchange of FPs alters the sensitivity of a genetically encoded sensor remains elusive, has, however, already been observed earlier (209). Our calibrations of GEPII 1.0 and R-GEPII 1.0 performed *in situ* demonstrated the suitability of GEPIIs, containing the wild-type Kbp, to differentiate a $[K^+]$ range between 0 – 100 mM K^+, which would allow the intracellular visualization of K^+

alterations upon cell death. A similar approach of the development of a GFP/RFP, based K^+ sensor referred to as KIRIN1-GR, was published recently (252). The authors used Clover, a GFP variant as the donor FP and mRuby2, a RFP variant representing the acceptor FP, to yield a construct identical with R-GEPII 1.0, with K_Ds of 2.56 mM ± 0.01 mM *in vitro* for KIRIN1-GR versus 4.113 mM ± 0.73 mM for R-GEPII *in situ* (252). However, the different mode of characterization, *in vitro* vs. *in situ*, makes it difficult to compare the determined EC_{50} values.

Nonetheless, vital cells maintain a steep K^+ gradient across their plasma membrane (1), thus, we chose different approaches to desensitize GEPIIs for K^+ to enable the investigation of physiologic intracellular K^+ fluctuations. It has already been demonstrated recently, that genetically encoded probes can quite easily be adjusted in their sensitivity by the introduction of point mutations within the analyte specific binding domain (210,221). In the publication of Ashraf et.al. describing the structure and function of Kbp, they did not investigate which amino acids of Kbp are directly involved in K^+ binding (226). Thus, we assumed that negatively charged amino acids located within the BON and LysM domain of Kbp might be responsible for the affinity of Kbp to the positively charged K^+. Upon exchange of most acidic amino acids located either in the BON or LysM domain, respectively, we observed drastically reduced affinity of GEPIIs for K^+. The constructs referred to as lc-BON GEPII 1.0 and lc-LysM GEPII 1.0 have either totally lost their K^+ binding affinity (lc-BON GEPII 1.0) or the affinity for K^+ was reduced ~ 70 fold (lc-LysM GEPII 1.0) (217). Nonetheless, importantly, both variants remained unspecific for other ions having a similar charge or size as K^+. Further optimizations of the K^+ sensitivity for intracellular K^+ imaging close to an EC_{50} of 140 mM K^+ may be achieved by the specific combination of single point mutations within both, the BON and the LysM domain.

As Kbp consists of two domains, BON and LysM, we further hypothesized that the introduction of linkers of variable length between the two domains may reduce the K^+ sensitivity of GEPIIs due to aggravation of their interaction. All constructs tested, namely GEPII 2.7, GEPII 2.10 and GEPII 2.15, containing amino acid linkers of 7, 10 and 15 amino acids, respectively, showed reduced K^+ affinity (217). However, these constructs have not been tested for their K^+ selectivity, as even single point mutations in the actual K^+ binding pockets did not alter this aspect. Nonetheless, all

constructs still possessed hill slopes close to 1, indicating that one protein of Kbp was binding one K^+ ion (217).

Another approach, which has already proven highly suitable to refine the ligand affinity of genetically encoded probes, is to perform error prone PCRs, which would introduce random point mutations within the ligand binding domain (224,225). In case of GEPIIs, we decided to use rational design rather than stochastic modification and yielded several constructs having lower affinity for K^+. Nonetheless, error prone PCR approaches may yield improved GEPIIs with optimized K_Ds for intracellular K^+ measurements or improved dynamic range.

Having identified the K^+ sensor variant with the lowest affinity for K^+, lc-LysM GEPII 1.0, we went on for its characterization upon expression within mammalian cells. Interestingly, similar to GEPII 1.0, lc-LysM GEPII 1.0 showed a drastically increased EC_{50} *in situ* to 60.95 mM compared to experiments performed *in vitro* (217). We also generated a red-shifted variant of this probe, lc-LysM R-GEPII 1.0, which even showed lower affinity. One explanation for the higher K_Ds of GEPIIs upon expression within cells might be the proteinaceous environment. However, further experiments within single cells were performed using the CFP/YFP based probe due to the bigger dynamic range of this variant. As expected, lc-BON GEPII 1.0 did not respond upon titration of increasing amounts of diverse ions, indicating the sensor is also a suitable negative control for GEPIIs *in situ* (217).

Our first experiments performed with GEPIIs expressed in cells aimed to quantify $[K^+]_i$. Upon expression of GEPII 1.0 and lc-LysM GEPII 1.0 targeted to different subcellular localizations, we observed organelle specific differences of the FRET-ratio signal of different cellular compartments. Highest FRET-ratio values were recorded from the nuclear- targeted, lowest FRET-ratio values from the mitochondria- targeted GEPIIs (217). These differences were absent upon expression of lc-BON GEPII 1.0, excluding artefacts caused by the targeting. Additionally, all differences of GEPII 1.0 and lc-LysM GEPII 1.0 were equalized by membrane permeabilization (217). Interestingly, the differences of nuclear- and cytosolic FRET-ratio signals were also evident upon expression of untargeted lc-LysM GEPII 1.0, localizing in the cytosol and nucleus of cells. Quantification of the FRET-ratio values received upon expression of targeted lc-LysM GEPII 1.0 resulted

in cytosolic [K^+] ~ 100 mM, nuclear [K^+] ~ 200 mM and mitochondrial [K^+] ~ 50 mM for different cell lines (217). In each cell line, the highest [K^+] was measured within the nucleus of the cells. Although seeming controversial due to the presence of nuclear pores permeable for proteins, already studies performed in the 1970s (46) and 1980s (47) measured a higher $[K^+]_{nuc}$. In line with these observations is the presence of a Na^+/K^+ ATPases located within the nuclear envelope, which has been demonstrated recently (43). There, the ATPase may generate a K^+ gradient towards the nuclear membrane. Although apoptosis is inhibited by elevated [K^+] andthe higher $[K^+]_{nuc}$ eventually may prevent DNA fragmentation (181) and apoptosis initiation (180), experimental evidences for the physiological consequences of higher $[K^+]_{nuc}$ still remain elusive. However, the relative distribution of intracellular [K^+] was cell type specific, and may represent hallmarks of cancerous alterations. All of our experiments performed to validate the results of higher $[K^+]_{nuc}$ confirmed the presence of an ATP consuming transport mechanism within the nuclear envelope. While the cytosolic and nuclear FRET-ratio signal of GEPII 1.0, which does not distinguish between [K^+] of 100 mM to 140 mM, remained unaffected upon treatment with 2-DG and ouabain, lc-LysM GEPII 1.0 reported organelle and treatment specific differences. Within the cytosol, the FRET-ratio signal of lc-LysM GEPII 1.0 was affected by both, 2-DG and ouabain treatment, while the nuclear FRET-ratio signal was only affected by the intracellular ATP depletion using 2-DG. This experiments pointed to i) an ATP dependent K^+ accumulation within the nucleus of HeLa cells, ii) being not abolished by ouabain treatment, which might not be cell membrane permeable. However, further experiments to understand the physiological importance of high $[K^+]_{nuc}$ are inevitable.

To demonstrate the applicability of GEPIIs for the real-time visualization of intracellular K^+ transients, we expressed lc-LysM GEPII 1.0 in different compartments of INS-1 cells (217). It has already been demonstrated recently, that the depolarization of INS-1 cells results in an increase of the intracellular [Ca^{2+}] (247). We hypothesized, that this increase in intracellular [Ca^{2+}] may open Kv or KCa channels expressed within this cell line, as well as another pancreatic β-cell line such as MIN-6. Indeed, our experiments showed a transient intracellular [K^+] reduction upon cell depolarization in both cell lines. Expression of GEPIIs in combination with genetically encoded Ca^{2+} indicators allowed the correlation of

intracellular Ca^{2+} and K^+ signals for the first time. Importantly, the high sensitive K^+ sensor GEPII 1.0 and lc-BON GEPII 1.0 did not show the effect of a transient cytosolic K^+ decrease (217).

We further aimed to characterize the transient cytosolic K^+ signal within INS-1 cells using pharmacological modulators. All of our treatments tested, including the removal of extracellular Ca^{2+}, unspecifically blocking all K^+ channels using TEA, blocking L-type Ca^{2+} channels using nifedipine or buffering the increase in $[Ca^{2+}]_i$ drastically reduced the K^+ transient (217). These results led to the conclusion that INS-1 cells express membrane potential dependent L- or T- type Ca^{2+} channels leading to a Ca^{2+} influx upon cell depolarization, which, in turn, activated KCa channels leading to the K^+ efflux from cells (217). Besides the visualization of cytosolic K^+ transients upon depolarization, we aimed to investigate subcellular K^+ fluctuations. Our experiments confirmed the assumption of concentration and electrical gradients driving K^+ fluxes into energized mitochondria, pointing to an effect of intracellular Ca^{2+} elevations on mitochondrial K^+ homeostasis. Besides the influence of Ca^{2+} elevations on mitochondrial K^+, our experiments pointed to an impact on the nuclear K^+ equilibrium (217).

In future, GEPIIs will open new avenues of extra- and intracellular K^+ imaging *in vitro*, *in situ* and *in vivo*, representing essential tools in (patho-) physiology and cell biology research. By the usage of GEPIIs, scientists could investigate the pharmacological effects of a variety of K^+ channel modulators on global and (sub-) cellular K^+ dynamics.

6 References

1. Palmer BF. Regulation of Potassium Homeostasis. Clinical Journal of the American Society of Nephrology. 2015 Jun 5;10(6):1050–60.
2. Armstrong CM. The Na/K pump, Cl ion, and osmotic stabilization of cells. Proc Natl Acad Sci USA. 2003 May 13;100(10):6257–62.
3. Kovesdy CP, Appel LJ, Grams ME, Gutekunst L, McCullough PA, Palmer BF, et al. Potassium Homeostasis in Health and Disease: A Scientific Workshop Cosponsored by the National Kidney Foundation and the American Society of Hypertension. American Journal of Kidney Diseases. 2017 Dec;70(6):844–58.
4. Udensi U, Tchounwou P. Potassium homeostasis, oxidative stress, and human disease. International Journal of Clinical and Experimental Physiology. 2017;4(3):111.
5. McDonough AA, Youn JH. Potassium Homeostasis: The Knowns, the Unknowns, and the Health Benefits. Physiology. 2017 Mar;32(2):100–11.
6. Lang F. Mechanisms and significance of cell volume regulation. J Am Coll Nutr. 2007 Oct;26(5 Suppl):613S-623S.
7. Kocsis JD, Malenka RC, Waxman SG. Effects of extracellular potassium concentration on the excitability of the parallel fibres of the rat cerebellum. J Physiol (Lond). 1983 Jan;334:225–44.
8. Grohovaz F, Fesce R, Haimann C. Dual effect of potassium on transmitter exocytosis. Cell Biol Int Rep. 1989 Dec;13(12):1085–95.
9. Larkin JM, Brown MS, Goldstein JL, Anderson RG. Depletion of intracellular potassium arrests coated pit formation and receptor-mediated endocytosis in fibroblasts. Cell. 1983 May;33(1):273–85.
10. Page MJ, Di Cera E. Role of Na^+ and K^+ in Enzyme Function. Physiological Reviews. 2006 Oct;86(4):1049–92.
11. Oria-Hernández J, Cabrera N, Pérez-Montfort R, Ramírez-Silva L. Pyruvate kinase revisited: the activating effect of K^+. J Biol Chem. 2005 Nov 11;280(45):37924–9.
12. Zhang Y, Dougherty M, Downs DM, Ealick SE. Crystal structure of an aminoimidazole riboside kinase from Salmonella enterica: implications for the evolution of the ribokinase superfamily. Structure. 2004 Oct;12(10):1809–21.
13. Kato M, Chuang JL, Tso S-C, Wynn RM, Chuang DT. Crystal structure of pyruvate dehydrogenase kinase 3 bound to lipoyl domain 2 of human pyruvate dehydrogenase complex. EMBO J. 2005 May 18;24(10):1763–74.
14. Bezine M, Debbabi M, Nury T, Ben-Khalifa R, Samadi M, Cherkaoui-Malki M, et al. Evidence of K^+ homeostasis disruption in cellular dysfunction triggered by 7-ketocholesterol, 24S-hydroxycholesterol, and tetracosanoic acid (C24:0) in 158N murine oligodendrocytes. Chem Phys Lipids. 2017;207(Pt B):135–50.
15. Eil R, Vodnala SK, Clever D, Klebanoff CA, Sukumar M, Pan JH, et al. Ionic immune suppression within the tumour microenvironment limits T cell effector function. Nature. 2016 Sep;537(7621):539–43.
16. Laskowski M, Augustynek B, Kulawiak B, Koprowski P, Bednarczyk P, Jarmuszkiewicz W, et al. What do we not know about mitochondrial potassium channels? Biochimica et Biophysica Acta (BBA) - Bioenergetics. 2016 Aug;1857(8):1247–57.
17. Palmer BF, Clegg DJ. Physiology and pathophysiology of potassium homeostasis. Adv Physiol Educ. 2016 Dec;40(4):480–90.
18. Tian C, Zhu R, Zhu L, Qiu T, Cao Z, Kang T. Potassium channels: structures, diseases, and modulators. Chem Biol Drug Des. 2014 Jan;83(1):1–26.
19. Castillo JP, Rui H, Basilio D, Das A, Roux B, Latorre R, et al. Mechanism of potassium ion uptake by the Na^+/K^+-ATPase. Nature Communications. 2015 Dec [cited 2019 Apr 5];6(1). Available from: http://www.nature.com/articles/ncomms8622
20. Garlid KD, Paucek P. Mitochondrial potassium transport: the K(+) cycle. Biochim Biophys Acta. 2003 Sep 30;1606(1–3):23–41.

21. Skou JC, Esmann M. The Na,K-ATPase. J Bioenerg Biomembr. 1992 Jun;24(3):249–61.
22. Kopec W, Loubet B, Poulsen H, Khandelia H. Molecular mechanism of Na(+),K(+)-ATPase malfunction in mutations characteristic of adrenal hypertension. Biochemistry. 2014 Feb 4;53(4):746–54.
23. Geering K. Functional roles of Na,K-ATPase subunits. Curr Opin Nephrol Hypertens. 2008 Sep;17(5):526–32.
24. Liu DS, Astumian RD, Tsong TY. Activation of Na^+ and K^+ pumping modes of (Na,K)-ATPase by an oscillating electric field. J Biol Chem. 1990 May 5;265(13):7260–7.
25. Ogawa H, Shinoda T, Cornelius F, Toyoshima C. Crystal structure of the sodium-potassium pump (Na^+,K^+-ATPase) with bound potassium and ouabain. Proc Natl Acad Sci USA. 2009 Aug 18;106(33):13742–7.
26. Post RL, Jolly PC. The linkage of sodium, potassium, and ammonium active transport across the human erythrocyte membrane. Biochim Biophys Acta. 1957 Jul;25(1):118–28.
27. Garrahan PJ, Glynn IM. The stoicheiometry of the sodium pump. J Physiol (Lond). 1967 Sep;192(1):217–35.
28. Erecińska M, Silver IA. Ions and energy in mammalian brain. Prog Neurobiol. 1994 May;43(1):37–71.
29. Xie Z, Askari A. Na(+)/K(+)-ATPase as a signal transducer. Eur J Biochem. 2002 May;269(10):2434–9.
30. Dempski RE, Lustig J, Friedrich T, Bamberg E. Structural arrangement and conformational dynamics of the gamma subunit of the Na^+/K^+-ATPase. Biochemistry. 2008 Jan 8;47(1):257–66.
31. Dempski RE, Friedrich T, Bamberg E. The beta subunit of the Na^+/K^+-ATPase follows the conformational state of the holoenzyme. J Gen Physiol. 2005 May;125(5):505–20.
32. Cortes VF, Veiga-Lopes FE, Barrabin H, Alves-Ferreira M, Fontes CFL. The gamma subunit of Na^+, K^+-ATPase: role on ATPase activity and regulatory phosphorylation by PKA. Int J Biochem Cell Biol. 2006;38(11):1901–13.
33. Devarajan P, Scaramuzzino DA, Morrow JS. Ankyrin binds to two distinct cytoplasmic domains of Na,K-ATPase alpha subunit. Proc Natl Acad Sci USA. 1994 Apr 12;91(8):2965–9.
34. Cunha SR, Mohler PJ. Ankyrin protein networks in membrane formation and stabilization. J Cell Mol Med. 2009 Dec;13(11–12):4364–76.
35. Yuan Z, Cai T, Tian J, Ivanov AV, Giovannucci DR, Xie Z. Na/K-ATPase Tethers Phospholipase C and IP3 Receptor into a Calcium-regulatory Complex. Molecular Biology of the Cell. 2005 Sep;16(9):4034–45.
36. Kim MJ, Kim E, Ryu SH, Suh PG. The mechanism of phospholipase C-gamma1 regulation. Exp Mol Med. 2000 Sep 30;32(3):101–9.
37. Aizman O, Uhlen P, Lal M, Brismar H, Aperia A. Ouabain, a steroid hormone that signals with slow calcium oscillations. Proceedings of the National Academy of Sciences. 2001 Nov 6;98(23):13420–4.
38. Foskett JK, White C, Cheung K-H, Mak D-OD. Inositol trisphosphate receptor Ca^{2+} release channels. Physiol Rev. 2007 Apr;87(2):593–658.
39. Yudowski GA, Efendiev R, Pedemonte CH, Katz AI, Berggren P-O, Bertorello AM. Phosphoinositide-3 kinase binds to a proline-rich motif in the Na^+,K^+-ATPase alpha subunit and regulates its trafficking. Proceedings of the National Academy of Sciences. 2000 Jun 6;97(12):6556–61.
40. Davis WJ, Lehmann PZ, Li W. Nuclear PI3K signaling in cell growth and tumorigenesis. Frontiers in Cell and Developmental Biology. 2015 Apr 13 [cited 2019 Apr 5];3. Available from: http://journal.frontiersin.org/article/10.3389/fcell.2015.00024/abstract
41. Lee K, Jung J, Kim M, Guidotti G. Interaction of the alpha subunit of Na,K-ATPase with cofilin. Biochem J. 2001 Jan 15;353(Pt 2):377–85.
42. Rodal AA, Tetreault JW, Lappalainen P, Drubin DG, Amberg DC. Aip1p interacts with cofilin to disassemble actin filaments. J Cell Biol. 1999 Jun 14;145(6):1251–64.
43. Garner MH. Na,K-ATPase in the nuclear envelope regulates Na^+: K^+ gradients in hepatocyte nuclei. J Membr Biol. 2002 May 15;187(2):97–115.

44. Keminer O, Peters R. Permeability of Single Nuclear Pores. Biophysical Journal. 1999 Jul;77(1):217–28.
45. Li C, Goryaynov A, Yang W. The selective permeability barrier in the nuclear pore complex. Nucleus. 2016 Sep 2;7(5):430–46.
46. Dick DA. The distribution of sodium, potassium and chloride in the nucleus and cytoplasm of Bufo bufo oocytes measured by electron microprobe analysis. J Physiol (Lond). 1978 Nov;284:37–53.
47. Paine PL, Pearson TW, Tluczek LJ, Horowitz SB. Nuclear sodium and potassium. Nature. 1981 May 21;291(5812):258–9.
48. Checchetto V, Teardo E, Carraretto L, Leanza L, Szabo I. Physiology of intracellular potassium channels: A unifying role as mediators of counterion fluxes? Biochim Biophys Acta. 2016 Aug;1857(8):1258–66.
49. González C, Baez-Nieto D, Valencia I, Oyarzún I, Rojas P, Naranjo D, et al. K(+) channels: function-structural overview. Compr Physiol. 2012 Jul;2(3):2087–149.
50. Jan LY, Jan YN. Voltage-gated potassium channels and the diversity of electrical signalling: Voltage-gated potassium channels. The Journal of Physiology. 2012 Jun 1;590(11):2591–9.
51. Hibino H, Inanobe A, Furutani K, Murakami S, Findlay I, Kurachi Y. Inwardly rectifying potassium channels: their structure, function, and physiological roles. Physiol Rev. 2010 Jan;90(1):291–366.
52. Piechotta PL, Rapedius M, Stansfeld PJ, Bollepalli MK, Ehrlich G, Erhlich G, et al. The pore structure and gating mechanism of K2P channels. EMBO J. 2011 Aug 5;30(17):3607–19.
53. Guéguinou M, Chantôme A, Fromont G, Bougnoux P, Vandier C, Potier-Cartereau M. KCa and Ca^{2+} channels: The complex thought. Biochimica et Biophysica Acta (BBA) - Molecular Cell Research. 2014 Oct;1843(10):2322–33.
54. Salkoff L, Butler A, Ferreira G, Santi C, Wei A. High-conductance potassium channels of the SLO family. Nat Rev Neurosci. 2006 Dec;7(12):921–31.
55. Ion Channels in Health and Disease. Elsevier; 2016 [cited 2019 Apr 5]. Available from: https://linkinghub.elsevier.com/retrieve/pii/C2014001711X
56. Luján R. Organisation of potassium channels on the neuronal surface. J Chem Neuroanat. 2010 Sep;40(1):1–20.
57. Horn R. How ion channels sense membrane potential. Proceedings of the National Academy of Sciences. 2005 Apr 5;102(14):4929–30.
58. Wulff H, Castle NA, Pardo LA. Voltage-gated potassium channels as therapeutic targets. Nature Reviews Drug Discovery. 2009 Dec;8(12):982–1001.
59. Grizel AV, Glukhov GS, Sokolova OS. Mechanisms of activation of voltage-gated potassium channels. Acta Naturae. 2014 Oct;6(4):10–26.
60. Szabò I, Zoratti M, Gulbins E. Contribution of voltage-gated potassium channels to the regulation of apoptosis. FEBS Letters. 2010 May 17;584(10):2049–56.
61. Song MS, Choi SY, Ryu PD, Lee SY. Voltage-Gated K^+ Channel, Kv3.3 Is Involved in Hemin-Induced K562 Differentiation. Pignataro G, editor. PLOS ONE. 2016 Feb 5;11(2):e0148633.
62. Serrano-Novillo C, Capera J, Colomer-Molera M, Condom E, Ferreres J, Felipe A. Implication of Voltage-Gated Potassium Channels in Neoplastic Cell Proliferation. Cancers. 2019 Mar 1;11(3):287.
63. Dubó S, Gallegos D, Cabrera L, Sobrevia L, Zúñiga L, González M. Cardiovascular Action of Insulin in Health and Disease: Endothelial L-Arginine Transport and Cardiac Voltage-Dependent Potassium Channels. Frontiers in Physiology. 2016 Mar 15 [cited 2019 Apr 5];7. Available from: http://journal.frontiersin.org/Article/10.3389/fphys.2016.00074/abstract
64. Li J, Blankenship ML, Baccei ML. Inward-Rectifying Potassium (Kir) Channels Regulate Pacemaker Activity in Spinal Nociceptive Circuits during Early Life. Journal of Neuroscience. 2013 Feb 20;33(8):3352–62.
65. Kawano T, Chen L, Watanabe SY, Yamauchi J, Kaziro Y, Nakajima Y, et al. Importance of the G protein gamma subunit in activating G protein-coupled inward rectifier K(+) channels. FEBS Lett. 1999 Dec 17;463(3):355–9.

66. Cui Y, Giblin JP, Clapp LH, Tinker A. A mechanism for ATP-sensitive potassium channel diversity: Functional coassembly of two pore-forming subunits. Proceedings of the National Academy of Sciences. 2001 Jan 16;98(2):729–34.
67. Butt AM, Kalsi A. Inwardly rectifying potassium channels (Kir) in central nervous system glia: a special role for Kir4.1 in glial functions. Journal of Cellular and Molecular Medicine. 2006 Jan;10(1):33–44.
68. Kofuji P, Newman EA. Potassium buffering in the central nervous system. Neuroscience. 2004 Jan;129(4):1043–54.
69. Cho H. Regulation of Adenosine-activated GIRK Channels by Gq-coupled Receptors in Mouse Atrial Myocytes. The Korean Journal of Physiology and Pharmacology. 2010;14(3):145.
70. Rifkin RA, Moss SJ, Slesinger PA. G Protein-Gated Potassium Channels: A Link to Drug Addiction. Trends in Pharmacological Sciences. 2017 Apr;38(4):378–92.
71. Liang B, Nissen JD, Laursen M, Wang X, Skibsbye L, Hearing MC, et al. G-protein-coupled inward rectifier potassium current contributes to ventricular repolarization. Cardiovascular Research. 2014 Jan 1;101(1):175–84.
72. Salazar NC, Chen J, Rockman HA. Cardiac GPCRs: GPCR signaling in healthy and failing hearts. Biochimica et Biophysica Acta (BBA) - Biomembranes. 2007 Apr;1768(4):1006–18.
73. Anderson A, Kulkarni K, Marron Fernandez de Velasco E, Carlblom N, Xia Z, Nakano A, et al. Expression and relevance of the G protein-gated K^+ channel in the mouse ventricle. Scientific Reports. 2018 Dec [cited 2019 Apr 5];8(1). Available from: http://www.nature.com/articles/s41598-018-19719-x
74. Olson TM, Terzic A. Human KATP channelopathies: diseases of metabolic homeostasis. Pflügers Archiv - European Journal of Physiology. 2010 Jul;460(2):295–306.
75. Kane G, Liu X, Yamada S, Olson T, Terzic A. Cardiac K channels in health and disease. Journal of Molecular and Cellular Cardiology. 2005 Jun;38(6):937–43.
76. Tammaro P, Ashcroft FM. Keeping the heart going: a new role for K_{ATP} channels. The Journal of Physiology. 2006 Dec 15;577(3):767–767.
77. Craig TJ, Ashcroft FM, Proks P. How ATP Inhibits the Open K_{ATP} Channel. The Journal of General Physiology. 2008 Jul;132(1):131–44.
78. Ashcroft FM, Rorsman P. K(ATP) channels and islet hormone secretion: new insights and controversies. Nat Rev Endocrinol. 2013 Nov;9(11):660–9.
79. Hamilton KL, Devor DC. Basolateral membrane K^+ channels in renal epithelial cells. American Journal of Physiology-Renal Physiology. 2012 May;302(9):F1069–81.
80. Zúñiga L, Zúñiga R. Understanding the Cap Structure in K2P Channels. Frontiers in Physiology. 2016 Jun 14 [cited 2019 Apr 5];7. Available from: http://journal.frontiersin.org/Article/10.3389/fphys.2016.00228/abstract
81. Lesage F, Barhanin J. Molecular Physiology of pH-Sensitive Background K_{2P} Channels. Physiology. 2011 Dec;26(6):424–37.
82. Schmidt C, Wiedmann F, Kallenberger SM, Ratte A, Schulte JS, Scholz B, et al. Stretch-activated two-pore-domain (K2P) potassium channels in the heart: Focus on atrial fibrillation and heart failure. Prog Biophys Mol Biol. 2017;130(Pt B):233–43.
83. Schneider ER, Anderson EO, Gracheva EO, Bagriantsev SN. Temperature sensitivity of two-pore (K2P) potassium channels. Curr Top Membr. 2014;74:113–33.
84. Mathie A. Neuronal two-pore-domain potassium channels and their regulation by G protein-coupled receptors. J Physiol (Lond). 2007 Jan 15;578(Pt 2):377–85.
85. Steinberg EA, Wafford KA, Brickley SG, Franks NP, Wisden W. The role of K2P channels in anaesthesia and sleep. Pflügers Archiv - European Journal of Physiology. 2015 May;467(5):907–16.
86. Williams S, Bateman A, O'Kelly I. Altered expression of two-pore domain potassium (K2P) channels in cancer. PLoS ONE. 2013;8(10):e74589.
87. Sepúlveda FV, Pablo Cid L, Teulon J, Niemeyer MI. Molecular Aspects of Structure, Gating, and Physiology of pH-Sensitive Background K_{2P} and Kir K^+-Transport Channels. Physiological Reviews. 2015 Jan;95(1):179–217.

88. Hughes S, Foster RG, Peirson SN, Hankins MW. Expression and localisation of two-pore domain (K2P) background leak potassium ion channels in the mouse retina. Scientific Reports. 2017 Dec [cited 2019 Apr 5];7(1). Available from: http://www.nature.com/articles/srep46085
89. Cadaveira-Mosquera A, Pérez M, Reboreda A, Rivas-Ramírez P, Fernández-Fernández D, Lamas JA. Expression of K2P channels in sensory and motor neurons of the autonomic nervous system. J Mol Neurosci. 2012 Sep;48(1):86–96.
90. Franks NP, Honoré E. The TREK K2P channels and their role in general anaesthesia and neuroprotection. Trends Pharmacol Sci. 2004 Nov;25(11):601–8.
91. Duprat F, Lauritzen I, Patel A, Honoré E. The TASK background K2P channels: chemo- and nutrient sensors. Trends Neurosci. 2007 Nov;30(11):573–80.
92. Shah VN, Chagot B, Chazin WJ. Calcium-Dependent Regulation of Ion Channels. Calcium Bind Proteins. 2006 Dec;1(4):203–12.
93. Köhler M, Hirschberg B, Bond CT, Kinzie JM, Marrion NV, Maylie J, et al. Small-conductance, calcium-activated potassium channels from mammalian brain. Science. 1996 Sep 20;273(5282):1709–14.
94. Carrasquel-Ursulaez W, Lorenzo Y, Echeverria F, Latorre R. Large Conductance Potassium Channels in the Nervous System. In: Bhattacharjee A, editor. The Oxford Handbook of Neuronal Ion Channels. Oxford University Press; 2018 [cited 2019 Apr 5]. Available from: http://oxfordhandbooks.com/view/10.1093/oxfordhb/9780190669164.001.0001/oxfordhb-9780190669164-e-11
95. Vetri F, Saha Roy Choudhury M, Sundivakkam P, Pelligrino DA. BKCa channels as physiological regulators: a focused review. Journal of Receptor, Ligand and Channel Research. 2014 Mar;3.
96. Lee US, Cui J. BK channel activation: structural and functional insights. Trends Neurosci. 2010 Sep;33(9):415–23.
97. Yuan A, Santi CM, Wei A, Wang ZW, Pollak K, Nonet M, et al. The sodium-activated potassium channel is encoded by a member of the Slo gene family. Neuron. 2003 Mar 6;37(5):765–73.
98. Paulais M, Lachheb S, Teulon J. A Na^+ - and Cl^- -activated K^+ Channel in the Thick Ascending Limb of Mouse Kidney. The Journal of General Physiology. 2006 Feb;127(2):205–15.
99. Contreras GF, Castillo K, Enrique N, Carrasquel-Ursulaez W, Castillo JP, Milesi V, et al. A BK (Slo1) channel journey from molecule to physiology. Channels. 2013 Nov 2;7(6):442–58.
100. Bhattacharjee A, Gan L, Kaczmarek LK. Localization of the Slack potassium channel in the rat central nervous system. J Comp Neurol. 2002 Dec 16;454(3):241–54.
101. Hu Z, Ma A, Tian H, Xi Y, Fan L, Wang T. Effects of age on expression of BKca channel in vascular smooth muscle cells from mesenteric arteries of spontaneously hypertensive rats. J Physiol Biochem. 2013 Dec;69(4):945–55.
102. Maqoud F, Cetrone M, Mele A, Tricarico D. Molecular structure and function of big calcium-activated potassium channels in skeletal muscle: pharmacological perspectives. Physiological Genomics. 2017 Jun;49(6):306–17.
103. Hoshi T, Pantazis A, Olcese R. Transduction of Voltage and Ca^{2+} Signals by Slo1 BK Channels. Physiology. 2013 May;28(3):172–89.
104. Price BR, Norris CM, Sompol P, Wilcock DM. An emerging role of astrocytes in vascular contributions to cognitive impairment and dementia. Journal of Neurochemistry. 2018 Mar;144(5):644–50.
105. Hayashi Y, Morinaga S, Zhang J, Satoh Y, Meredith AL, Nakata T, et al. BK channels in microglia are required for morphine-induced hyperalgesia. Nature Communications. 2016 Dec [cited 2019 Apr 5];7(1). Available from: http://www.nature.com/articles/ncomms11697
106. Lehnhardt A, Kemper MJ. Pathogenesis, diagnosis and management of hyperkalemia. Pediatr Nephrol. 2011 Mar;26(3):377–84.
107. Kardalas E, Paschou SA, Anagnostis P, Muscogiuri G, Siasos G, Vryonidou A. Hypokalemia: a clinical update. Endocr Connect. 2018 Apr;7(4):R135–46.

108. Cheng C-J, Kuo E, Huang C-L. Extracellular potassium homeostasis: insights from hypokalemic periodic paralysis. Semin Nephrol. 2013 May;33(3):237–47.
109. Welch AA, Fransen H, Jenab M, Boutron-Ruault MC, Tumino R, Agnoli C, et al. Variation in intakes of calcium, phosphorus, magnesium, iron and potassium in 10 countries in the European Prospective Investigation into Cancer and Nutrition study. Eur J Clin Nutr. 2009 Nov;63 Suppl 4:S101-121.
110. Cornelius RJ, Wang B, Wang-France J, Sansom SC. Maintaining K^+ balance on the low-Na^+, high-K^+ diet. Am J Physiol Renal Physiol. 2016 01;310(7):F581–95.
111. van Ypersele de Strihou C. Potassium homeostasis in renal failure. Kidney International. 1977 Jun;11(6):491–504.
112. Chmielewski C. Renal anatomy and overview of nephron function. Nephrol Nurs J. 2003 Apr;30(2):185–90; quiz 191–2.
113. Preuss HG. Basics of renal anatomy and physiology. Clin Lab Med. 1993 Mar;13(1):1–11.
114. Thévenod F, Wolff NA. Iron transport in the kidney: implications for physiology and cadmium nephrotoxicity. Metallomics. 2016;8(1):17–42.
115. Zhuo JL, Li XC. Proximal Nephron. In: Terjung R, editor. Comprehensive Physiology. Hoboken, NJ, USA: John Wiley & Sons, Inc.; 2013 [cited 2019 Apr 5]. Available from: http://doi.wiley.com/10.1002/cphy.c110061
116. Hebert SC, Desir G, Giebisch G, Wang W. Molecular diversity and regulation of renal potassium channels. Physiol Rev. 2005 Jan;85(1):319–71.
117. Mount DB. Thick ascending limb of the loop of Henle. Clin J Am Soc Nephrol. 2014 Nov 7;9(11):1974–86.
118. Hou J. Paracellular transport in the collecting duct. Curr Opin Nephrol Hypertens. 2016;25(5):424–8.
119. Castañeda-Bueno M, Arroyo JP, Gamba G. Independent Regulation of Na^+ and K^+ Balance by the Kidney. Medical Principles and Practice. 2012;21(2):101–14.
120. Pearce D, Soundararajan R, Trimpert C, Kashlan OB, Deen PMT, Kohan DE. Collecting Duct Principal Cell Transport Processes and Their Regulation. Clinical Journal of the American Society of Nephrology. 2015 Jan 7;10(1):135–46.
121. Hou J. Regulation of paracellular transport in the distal nephron: Current Opinion in Nephrology and Hypertension. 2012 Sep;21(5):547–51.
122. Giebisch G. Renal potassium transport: mechanisms and regulation. American Journal of Physiology-Renal Physiology. 1998 May;274(5):F817–33.
123. Ho K. A Critically Swift Response: Insulin-Stimulated Potassium and Glucose Transport in Skeletal Muscle. Clinical Journal of the American Society of Nephrology. 2011 Jul 1;6(7):1513–6.
124. Moratinos J, Reverte M. Effects of catecholamines on plasma potassium: the role of alpha- and beta-adrenoceptors. Fundam Clin Pharmacol. 1993;7(3–4):143–53.
125. McNicholas BA, Pham MH, Carli K, Chen CH, Colobong-Smith N, Anderson AE, et al. Treatment of Hyperkalemia With a Low-Dose Insulin Protocol Is Effective and Results in Reduced Hypoglycemia. Kidney International Reports. 2018 Mar;3(2):328–36.
126. Van Slyke DD, Wu H, McLean FC. Factors controlling the electrolyte and water distribution in the blood. Experimental Biology and Medicine. 1923 Jan 1;20(4):218–9.
127. Jacobs MH, Stewart DR. Osmotic properties of the erythrocyte; ionic and osmotic equilibria with a complex external solution. J Cell Comp Physiol. 1947 Aug;30(1):79–103.
128. Kedem O, Essig A. Isotope flows and flux ratios in biological membranes. J Gen Physiol. 1965 Jul;48(6):1047–70.
129. Tosteson DC, Hoffman JF. Regulation of cell volume by active cation transport in high and low potassium sheep red cells. J Gen Physiol. 1960 Sep;44:169–94.
130. Sachs JR, Welt LG. The Concentration Dependence of Active Potassium Transport in the Human Red Blood Cell*. Journal of Clinical Investigation. 1967 Jan 1;46(1):65–76.
131. Tivey DR, Simmons NL, Aiton JF. Role of passive potassium fluxes in cell volume regulation in cultured HeLa cells. The Journal of Membrane Biology. 1985 Jun;87(2):93–105.

132. Boucrot E, Kirchhausen T. Mammalian Cells Change Volume during Mitosis. Blagosklonny M, editor. PLoS ONE. 2008 Jan 23;3(1):e1477.
133. Zlotek-Zlotkiewicz E, Monnier S, Cappello G, Le Berre M, Piel M. Optical volume and mass measurements show that mammalian cells swell during mitosis. The Journal of Cell Biology. 2015 Nov 23;211(4):765–74.
134. Fidorra J, Mielke T, Booz J, Feinendegen LE. Cellular and nuclear volume of human cells during the cell cycle. Radiat Environ Biophys. 1981;19(3):205–14.
135. Urrego D, Tomczak AP, Zahed F, Stuhmer W, Pardo LA. Potassium channels in cell cycle and cell proliferation. Philosophical Transactions of the Royal Society B: Biological Sciences. 2014 Feb 3;369(1638):20130094–20130094.
136. Roux B. The Membrane Potential and its Representation by a Constant Electric Field in Computer Simulations. Biophysical Journal. 2008 Nov;95(9):4205–16.
137. Ma Y, Poole K, Goyette J, Gaus K. Introducing Membrane Charge and Membrane Potential to T Cell Signaling. Frontiers in Immunology. 2017 Nov 9 [cited 2019 Apr 5];8. Available from: http://journal.frontiersin.org/article/10.3389/fimmu.2017.01513/full
138. Sheu SS, Blaustein MP. Effects of calcium on membrane potential and sodium influx in barnacle muscle fibers. Am J Physiol. 1983 Mar;244(3):C297-302.
139. Dulhunty AF. The dependence of membrane potential on extracellular chloride concentration in mammalian skeletal muscle fibres. J Physiol (Lond). 1978 Mar;276:67–82.
140. Bara M, Ibrahim B, Leveteau J, Guiet-Bara A. Implication of external Mg^{2+} ions in the depolarization of smooth muscle cell membrane of the human chorionic placental vessels: an hypothesis. Magnes Res. 1997 Mar;10(1):3–10.
141. Miao K, Wondergem R, Hossler FE, Joyner WL. Contributions of K^+, Na^+, and Cl^- to the membrane potential of intact hamster vascular endothelial cells. J Cell Physiol. 1993 Sep;156(3):550–9.
142. Wilbrandt W. THE EFFECT OF ORGANIC IONS ON THE MEMBRANE POTENTIAL OF NERVES. J Gen Physiol. 1937 Mar 20;20(4):519–41.
143. Hober R. Über den Einfluss der Salze auf den Ruhestrom des Froschmuskels. Pflüg Arch ges Physiol. 1905;599–635.
144. Vaughan Williams EM. The effect of changes in extracellular potassium concentration on the intracellular potentials of isolated rabbit atria. J Physiol (Lond). 1959 Jun 11;146(3):411–28.
145. Poulsen JH, Williams JA. Effect of extracellular K^+ concentration on resting potential, caerulein-induced depolarization and amylase release from mouse pancreatic acinar cells. Pflugers Arch. 1977 Aug 29;370(2):173–7.
146. Stiehler, R.D., Flexner, L.B. A mechanism of secretion in the choroid plexus. The conversion of oxidation reduction energy into work. Journal of Biological Chemistry. (1):603–17.
147. Mitchell P. Chemiosmotic coupling in oxidative and photosynthetic phosphorylation. 1966. Biochim Biophys Acta. 2011 Dec;1807(12):1507–38.
148. Zorova LD, Popkov VA, Plotnikov EY, Silachev DN, Pevzner IB, Jankauskas SS, et al. Mitochondrial membrane potential. Analytical Biochemistry. 2018 Jul;552:50–9.
149. Ehrenstein G, Lecar H. The Mechanism of Signal Transmission in Nerve Axons. Annual Review of Biophysics and Bioengineering. 1972 Jun;1(1):347–66.
150. Ceccarelli B, Fesce R, Grohovaz F, Haimann C. The effect of potassium on exocytosis of transmitter at the frog neuromuscular junction. J Physiol (Lond). 1988 Jul;401:163–83.
151. Singer-Lahat D, Sheinin A, Chikvashvili D, Tsuk S, Greitzer D, Friedrich R, et al. K^+ channel facilitation of exocytosis by dynamic interaction with syntaxin. J Neurosci. 2007 Feb 14;27(7):1651–8.
152. Madshus IH, Sandvig K, Olsnes S, van Deurs B. Effect of reduced endocytosis induced by hypotonic shock and potassium depletion on the infection of Hep 2 cells by picornaviruses. J Cell Physiol. 1987 Apr;131(1):14–22.
153. Pilchova I, Klacanova K, Tatarkova Z, Kaplan P, Racay P. The Involvement of Mg^{2+} in Regulation of Cellular and Mitochondrial Functions. Oxidative Medicine and Cellular Longevity. 2017;2017:1–8.

154. Bagur R, Hajnóczky G. Intracellular Ca 2+ Sensing: Its Role in Calcium Homeostasis and Signaling. Molecular Cell. 2017 Jun;66(6):780–8.
155. Kachmar JF, Boyer PD. Kinetic analysis of enzyme reactions. II. The potassium activation and calcium inhibition of pyruvic phosphoferase. J Biol Chem. 1953 Feb;200(2):669–82.
156. Ævarsson A, Chuang JL, Max Wynn R, Turley S, Chuang DT, Hol WG. Crystal structure of human branched-chain α-ketoacid dehydrogenase and the molecular basis of multienzyme complex deficiency in maple syrup urine disease. Structure. 2000 Mar;8(3):277–91.
157. Hohenester E, Keller JW, Jansonius JN. An Alkali Metal Ion Size-Dependent Switch in the Active Site Structure of Dialkylglycine Decarboxylase. Biochemistry. 1994 Nov;33(46):13561–70.
158. Wheatley RW, Juers DH, Lev BB, Huber RE, Noskov SY. Elucidating factors important for monovalent cation selectivity in enzymes: E. coli β-galactosidase as a model. Physical Chemistry Chemical Physics. 2015;17(16):10899–909.
159. Gohara DW, Di Cera E. Molecular Mechanisms of Enzyme Activation by Monovalent Cations. Journal of Biological Chemistry. 2016 Sep 30;291(40):20840–8.
160. Shibata N, Masuda J, Tobimatsu T, Toraya T, Suto K, Morimoto Y, et al. A new mode of B12 binding and the direct participation of a potassium ion in enzyme catalysis: X-ray structure of diol dehydratase. Structure. 1999 Aug;7(8):997–1008.
161. Liao D-I, Dotson G, Turner I, Reiss L, Emptage M. Crystal structure of substrate free form of glycerol dehydratase. Journal of Inorganic Biochemistry. 2003 Jan;93(1–2):84–91.
162. Andersson CE, Mowbray SL. Activation of ribokinase by monovalent cations. Journal of Molecular Biology. 2002 Jan;315(3):409–19.
163. Yamada T, Komoto J, Takata Y, Ogawa H, Pitot HC, Takusagawa F. Crystal Structure of Serine Dehydratase from Rat Liver † , ‡. Biochemistry. 2003 Nov;42(44):12854–65.
164. Medler TR, Cotechini T, Coussens LM. Immune response to cancer therapy: mounting an effective antitumor response and mechanisms of resistance. Trends Cancer. 2015 Sep 1;1(1):66–75.
165. Smith-Garvin JE, Koretzky GA, Jordan MS. T Cell Activation. Annual Review of Immunology. 2009 Apr;27(1):591–619.
166. Miceli MC, Parnes JR. The roles of CD4 and CD8 in T cell activation. Semin Immunol. 1991 May;3(3):133–41.
167. Gurusamy D, Clever D, Eil R, Restifo NP. Novel “Elements” of Immune Suppression within the Tumor Microenvironment. Cancer Immunol Res. 2017;5(6):426–33.
168. Elmore S. Apoptosis: A Review of Programmed Cell Death. Toxicologic Pathology. 2007 Jun;35(4):495–516.
169. Glucksmann A. Cell deaths in normal vertebrate ontogeny. Biol Rev Camb Philos Soc. 1951 Feb;26(1):59–86.
170. Golstein P, Kroemer G. Cell death by necrosis: towards a molecular definition. Trends in Biochemical Sciences. 2007 Jan;32(1):37–43.
171. Kerr JF, Wyllie AH, Currie AR. Apoptosis: a basic biological phenomenon with wide-ranging implications in tissue kinetics. Br J Cancer. 1972 Aug;26(4):239–57.
172. Adamczyk M, Kostka G, Palut D. [The role of apoptosis in cell physiology and pathology]. Rocz Panstw Zakl Hig. 1998;49(4):415–32.
173. Wang XQ. Apoptotic insults impair Na^+, K^+-ATPase activity as a mechanism of neuronal death mediated by concurrent ATP deficiency and oxidant stress. Journal of Cell Science. 2003 May 15;116(10):2099–110.
174. Bortner CD, Hughes FM, Cidlowski JA. A Primary Role for K^+ and Na^+ Efflux in the Activation of Apoptosis. Journal of Biological Chemistry. 1997 Dec 19;272(51):32436–42.
175. McCarthy JV, Cotter TG. Cell shrinkage and apoptosis: a role for potassium and sodium ion efflux. Cell Death Differ. 1997 Dec;4(8):756–70.
176. Gleichmann M, Beinroth S, Reed JC, Krajewski S, Schulz JB, Wüllner U, et al. Potassium deprivation-induced apoptosis of cerebellar granule neurons: cytochrome c release in the absence of altered expression of Bcl-2 family proteins. Cell Physiol Biochem. 1998;8(4):194–201.

177. Volbracht C, Leist M, Nicotera P. ATP controls neuronal apoptosis triggered by microtubule breakdown or potassium deprivation. Mol Med. 1999 Jul;5(7):477–89.
178. Harvey NL, Kumar S. The role of caspases in apoptosis. Adv Biochem Eng Biotechnol. 1998;62:107–28.
179. Samejima K, Earnshaw WC. Trashing the genome: the role of nucleases during apoptosis. Nat Rev Mol Cell Biol. 2005 Sep;6(9):677–88.
180. Cain K, Langlais C, Sun X-M, Brown DG, Cohen GM. Physiological Concentrations of K^+ Inhibit Cytochrome *c* -dependent Formation of the Apoptosome. Journal of Biological Chemistry. 2001 Nov 9;276(45):41985–90.
181. Hughes FM, Cidlowski JA. Potassium is a critical regulator of apoptotic enzymes in vitro and in vivo. Adv Enzyme Regul. 1999;39:157–71.
182. Karki P, Seong C, Kim J-E, Hur K, Shin SY, Lee JS, et al. Intracellular K(+) inhibits apoptosis by suppressing the Apaf-1 apoptosome formation and subsequent downstream pathways but not cytochrome c release. Cell Death Differ. 2007 Dec;14(12):2068–75.
183. Yu SP, Choi DW. Ions, cell volume, and apoptosis. Proc Natl Acad Sci USA. 2000 Aug 15;97(17):9360–2.
184. Jansson B. Potassium, sodium, and cancer: a review. J Environ Pathol Toxicol Oncol. 1996;15(2–4):65–73.
185. Stacey NH, Klaassen CD. Interaction of metal ions with cadmium-induced cellular toxicity. Journal of Toxicology and Environmental Health. 1981 Jan;7(1):149–58.
186. Colt EWD, Wang J, Stallone F, Van Itallie TB, Pierson RN. A possible low intracellular potassium in obesity. The American Journal of Clinical Nutrition. 1981 Mar 1;34(3):367–72.
187. Stephens PJ. The effects of ethanol on intracellular potassium and the membrane potential of an identified crab motor axon. Comparative Biochemistry and Physiology Part C: Comparative Pharmacology. 1992 Feb;101(2):289–92.
188. Li Y, Schellhorn HE. New Developments and Novel Therapeutic Perspectives for Vitamin C. The Journal of Nutrition. 2007 Nov 1;137(10):2171–84.
189. Dilsiz N, Olcucu A, Cay M, Naziroglu M, Cobanoglu D. Protective effects of selenium, vitamin C and vitamin E against oxidative stress of cigarette smoke in rats. Cell Biochem Funct. 1999 Mar;17(1):1–7.
190. Lockette WE, Webb RC, Bohr DF. Prostaglandins and potassium relaxation in vascular smooth muscle of the rat. The role of Na-K ATPase. Circ Res. 1980 May;46(5):714–20.
191. Ossey K, McIntyre RW. Stress and hypokalemia. Anesthesiology. 1987 Mar;66(3):443–4.
192. Elisaf M, Liberopoulos E, Bairaktari E, Siamopoulos K. Hypokalaemia in alcoholic patients. Drug Alcohol Rev. 2002 Mar;21(1):73–6.
193. Seitz HK, Becker P. Alcohol metabolism and cancer risk. Alcohol Res Health. 2007;30(1):38–41, 44–7.
194. Chiriac V-F, Baban A, Dumitrascu DL. PSYCHOLOGICAL STRESS AND BREAST CANCER INCIDENCE: A SYSTEMATIC REVIEW. Medicine and Pharmacy Reports. 2018 Jan 30;91(1):18–26.
195. Huang X, Jan LY. Targeting potassium channels in cancer. The Journal of Cell Biology. 2014 Jul 21;206(2):151–62.
196. Velarde-Miranda C, Gomez-Sanchez EP, Gomez-Sanchez CE. Regulation of aldosterone biosynthesis by the Kir3.4 (KCNJ5) potassium channel. Clinical and Experimental Pharmacology and Physiology. 2013 Dec;40(12):895–901.
197. Stringer BK, Cooper AG, Shepard SB. Overexpression of the G-protein inwardly rectifying potassium channel 1 (GIRK1) in primary breast carcinomas correlates with axillary lymph node metastasis. Cancer Res. 2001 Jan 15;61(2):582–8.
198. Luminescence in Hydromedusae. Proceedings of the Royal Society of London Series B - Biological Sciences. 1955 Nov 29;144(916):399–411.
199. Shimomura O, Johnson FH, Saiga Y. Extraction, Purification and Properties of Aequorin, a Bioluminescent Protein from the Luminous Hydromedusan,Aequorea. Journal of Cellular and Comparative Physiology. 1962 Jun;59(3):223–39.

200. Yang F, Moss LG, Phillips GN. The molecular structure of green fluorescent protein. Nat Biotechnol. 1996 Oct;14(10):1246–51.
201. Craggs TD. Green fluorescent protein: structure, folding and chromophore maturation. Chem Soc Rev. 2009 Oct;38(10):2865–75.
202. Chalfie M, Tu Y, Euskirchen G, Ward W, Prasher D. Green fluorescent protein as a marker for gene expression. Science. 1994 Feb 11;263(5148):802–5.
203. Feilmeier BJ, Iseminger G, Schroeder D, Webber H, Phillips GJ. Green fluorescent protein functions as a reporter for protein localization in Escherichia coli. J Bacteriol. 2000 Jul;182(14):4068–76.
204. Matz MV, Fradkov AF, Labas YA, Savitsky AP, Zaraisky AG, Markelov ML, et al. Fluorescent proteins from nonbioluminescent Anthozoa species. Nat Biotechnol. 1999 Oct;17(10):969–73.
205. Shaner NC, Steinbach PA, Tsien RY. A guide to choosing fluorescent proteins. Nature Methods. 2005 Dec;2(12):905–9.
206. Miyawaki A, Llopis J, Heim R, McCaffery JM, Adams JA, Ikura M, et al. Fluorescent indicators for Ca^{2+} based on green fluorescent proteins and calmodulin. Nature. 1997 Aug 28;388(6645):882–7.
207. Walsh MP. Calmodulin and its roles in skeletal muscle function. Can Anaesth Soc J. 1983 Jul;30(4):390–8.
208. Ikura M, Clore GM, Gronenborn AM, Zhu G, Klee CB, Bax A. Solution structure of a calmodulin-target peptide complex by multidimensional NMR. Science. 1992 May 1;256(5057):632–8.
209. Waldeck-Weiermair M, Bischof H, Blass S, Deak A, Klec C, Graier T, et al. Generation of Red-Shifted Cameleons for Imaging Ca^{2+} Dynamics of the Endoplasmic Reticulum. Sensors. 2015 Jun 4;15(6):13052–68.
210. Imamura H, Huynh Nhat KP, Togawa H, Saito K, Iino R, Kato-Yamada Y, et al. Visualization of ATP levels inside single living cells with fluorescence resonance energy transfer-based genetically encoded indicators. Proceedings of the National Academy of Sciences. 2009 Sep 15;106(37):15651–6.
211. San Martín A, Ceballo S, Baeza-Lehnert F, Lerchundi R, Valdebenito R, Contreras-Baeza Y, et al. Imaging Mitochondrial Flux in Single Cells with a FRET Sensor for Pyruvate. Koch K-W, editor. PLoS ONE. 2014 Jan 21;9(1):e85780.
212. Lindenburg LH, Vinkenborg JL, Oortwijn J, Aper SJA, Merkx M. MagFRET: The First Genetically Encoded Fluorescent Mg^{2+} Sensor. Soares CM, editor. PLoS ONE. 2013 Dec 2;8(12):e82009.
213. Takanaga H, Chaudhuri B, Frommer WB. GLUT1 and GLUT9 as major contributors to glucose influx in HepG2 cells identified by a high sensitivity intramolecular FRET glucose sensor. Biochimica et Biophysica Acta (BBA) - Biomembranes. 2008 Apr;1778(4):1091–9.
214. Lindenburg L, Merkx M. Engineering genetically encoded FRET sensors. Sensors (Basel). 2014 Jul 2;14(7):11691–713.
215. Berg J, Hung YP, Yellen G. A genetically encoded fluorescent reporter of ATP:ADP ratio. Nature Methods. 2009 Feb;6(2):161–6.
216. Raimondo J. A genetically-encoded chloride and pH sensor for dissociating ion dynamics in the nervous system. Frontiers in Cellular Neuroscience. 2013 [cited 2019 Apr 5];7. Available from: http://journal.frontiersin.org/article/10.3389/fncel.2013.00202/abstract
217. Bischof H, Rehberg M, Stryeck S, Artinger K, Eroglu E, Waldeck-Weiermair M, et al. Novel genetically encoded fluorescent probes enable real-time detection of potassium in vitro and in vivo. Nat Commun. 2017 10;8(1):1422.
218. Oldach L, Zhang J. Genetically Encoded Fluorescent Biosensors for Live-Cell Visualization of Protein Phosphorylation. Chemistry & Biology. 2014 Feb;21(2):186–97.
219. Margineanu A, Chan JJ, Kelly DJ, Warren SC, Flatters D, Kumar S, et al. Screening for protein-protein interactions using Förster resonance energy transfer (FRET) and fluorescence lifetime imaging microscopy (FLIM). Scientific Reports. 2016 Sep [cited 2019 Apr 5];6(1). Available from: http://www.nature.com/articles/srep28186

220. Burgstaller S, Bischof H, Gensch T, Stryeck S, Gottschalk B, Ramadani-Muja J, et al. pH-Lemon, a Fluorescent Protein-Based pH Reporter for Acidic Compartments. ACS Sensors. 2019 Mar 30 [cited 2019 Apr 5]; Available from: http://pubs.acs.org/doi/10.1021/acssensors.8b01599
221. Yaginuma H, Kawai S, Tabata KV, Tomiyama K, Kakizuka A, Komatsuzaki T, et al. Diversity in ATP concentrations in a single bacterial cell population revealed by quantitative single-cell imaging. Scientific Reports. 2015 May [cited 2019 Feb 25];4(1). Available from: http://www.nature.com/articles/srep06522
222. Eroglu E, Gottschalk B, Charoensin S, Blass S, Bischof H, Rost R, et al. Development of novel FP-based probes for live-cell imaging of nitric oxide dynamics. Nature Communications. 2016 Dec [cited 2019 Feb 25];7(1). Available from: http://www.nature.com/articles/ncomms10623
223. Nagai T, Sawano A, Park ES, Miyawaki A. Circularly permuted green fluorescent proteins engineered to sense Ca^{2+}. Proceedings of the National Academy of Sciences. 2001 Mar 13;98(6):3197–202.
224. Zhao Y, Araki S, Wu J, Teramoto T, Chang Y-F, Nakano M, et al. An expanded palette of genetically encoded Ca^{2+} indicators. Science. 2011 Sep 30;333(6051):1888–91.
225. Wu J, Liu L, Matsuda T, Zhao Y, Rebane A, Drobizhev M, et al. Improved orange and red Ca^{2}± indicators and photophysical considerations for optogenetic applications. ACS Chem Neurosci. 2013 Jun 19;4(6):963–72.
226. Ashraf KU, Josts I, Mosbahi K, Kelly SM, Byron O, Smith BO, et al. The Potassium Binding Protein Kbp Is a Cytoplasmic Potassium Sensor. Structure. 2016 May;24(5):741–9.
227. Yeats C, Bateman A. The BON domain: a putative membrane-binding domain. Trends in Biochemical Sciences. 2003 Jul;28(7):352–5.
228. Teriete P, Yao Y, Kolodzik A, Yu J, Song H, Niederweis M, et al. *Mycobacterium tuberculosis* Rv0899 Adopts a Mixed α/β-Structure and Does Not Form a Transmembrane β-Barrel. Biochemistry. 2010 Apr 6;49(13):2768–77.
229. Yang Y, Auguin D, Delbecq S, Dumas E, Molle G, Molle V, et al. Structure of the Mycobacterium tuberculosis OmpATb protein: A model of an oligomeric channel in the mycobacterial cell wall. Proteins: Structure, Function, and Bioinformatics. 2011 Feb;79(2):645–61.
230. Buist G, Steen A, Kok J, Kuipers OP. LysM, a widely distributed protein motif for binding to (peptido)glycans. Molecular Microbiology. 2008 May;68(4):838–47.
231. Mesnage S, Dellarole M, Baxter NJ, Rouget J-B, Dimitrov JD, Wang N, et al. Molecular basis for bacterial peptidoglycan recognition by LysM domains. Nature Communications. 2014 Dec [cited 2019 Apr 5];5(1). Available from: http://www.nature.com/articles/ncomms5269
232. Andre G, Leenhouts K, Hols P, Dufrene YF. Detection and Localization of Single LysM-Peptidoglycan Interactions. Journal of Bacteriology. 2008 Nov 1;190(21):7079–86.
233. Weber A, Jung K. Profiling Early Osmostress-Dependent Gene Expression in Escherichia coli Using DNA Macroarrays. Journal of Bacteriology. 2002 Oct 1;184(19):5502–7.
234. Storvik KAM, Foster PL. RpoS, the Stress Response Sigma Factor, Plays a Dual Role in the Regulation of Escherichia coli's Error-Prone DNA Polymerase IV. Journal of Bacteriology. 2010 Jul 15;192(14):3639–44.
235. Sedighi M, Moghoofei M, Kouhsari E, Pournajaf A, Emadi B, Tohidfar M, et al. In silico analysis and molecular modeling of RNA polymerase, sigma S (RpoS) protein in Pseudomonas aeruginosa PAO1. Rep Biochem Mol Biol. 2015 Oct;4(1):32–42.
236. Baez S. An open cremaster muscle preparation for the study of blood vessels by in vivo microscopy. Microvascular Research. 1973 May;5(3):384–94.
237. Rehberg M, Leite CF, Mildner K, Horstkotte J, Zeuschner D, Krombach F. Surface Chemistry of Quantum Dots Determines Their Behavior in Postischemic Tissue. ACS Nano. 2012 Feb 28;6(2):1370–9.
238. Rizzo MA, Springer GH, Granada B, Piston DW. An improved cyan fluorescent protein variant useful for FRET. Nature Biotechnology. 2004 Apr;22(4):445–9.

239. Nagai T, Yamada S, Tominaga T, Ichikawa M, Miyawaki A. Expanded dynamic range of fluorescent indicators for Ca^{2+} by circularly permuted yellow fluorescent proteins. Proceedings of the National Academy of Sciences. 2004 Jul 20;101(29):10554–9.

240. Carter NW. Intracellular pH. Kidney International. 1972 May;1(5):341–6.

241. Damaghi M, Wojtkowiak JW, Gillies RJ. pH sensing and regulation in cancer. Front Physiol. 2013 Dec 17;4:370.

242. Epstein W. The roles and regulation of potassium in bacteria. Prog Nucleic Acid Res Mol Biol. 2003;75:293–320.

243. Giammarioli AM, Gambardella L, Barbati C, Pietraforte D, Tinari A, Alberton M, et al. Differential effects of the glycolysis inhibitor 2-deoxy-D-glucose on the activity of pro-apoptotic agents in metastatic melanoma cells, and induction of a cytoprotective autophagic response. International Journal of Cancer. 2012 Aug 15;131(4):E337–47.

244. Fleidervish IA, Lasser-Ross N, Gutnick MJ, Ross WN. Na^+ imaging reveals little difference in action potential–evoked Na^+ influx between axon and soma. Nature Neuroscience. 2010 Jul;13(7):852–60.

245. Depaoli MR, Karsten F, Madreiter-Sokolowski CT, Klec C, Gottschalk B, Bischof H, et al. Real-Time Imaging of Mitochondrial ATP Dynamics Reveals the Metabolic Setting of Single Cells. Cell Reports. 2018 Oct;25(2):501-512.e3.

246. Nguyen A-NT, Wallace DP, Blanco G. Ouabain Binds with High Affinity to the Na,K-ATPase in Human Polycystic Kidney Cells and Induces Extracellular Signal–Regulated Kinase Activation and Cell Proliferation. Journal of the American Society of Nephrology. 2007 Jan;18(1):46–57.

247. Alam MR, Groschner LN, Parichatikanond W, Kuo L, Bondarenko AI, Rost R, et al. Mitochondrial Ca^{2+} uptake 1 (MICU1) and mitochondrial Ca^{2+} uniporter (MCU) contribute to metabolism-secretion coupling in clonal pancreatic β-cells. J Biol Chem. 2012 Oct 5;287(41):34445–54.

248. Jezek P, Mahdi F, Garlid KD. Reconstitution of the beef heart and rat liver mitochondrial K^+/H^+ (Na^+/H^+) antiporter. Quantitation of K^+ transport with the novel fluorescent probe, PBFI. J Biol Chem. 1990 Jun 25;265(18):10522–6.

249. Rana PS, Gibbons BA, Vereninov AA, Yurinskaya VE, Clements RJ, Model TA, et al. Calibration and characterization of intracellular Asante Potassium Green probes, APG-2 and APG-4. Analytical Biochemistry. 2019 Feb;567:8–13.

250. Kong X, Su F, Zhang L, Yaron J, Lee F, Shi Z, et al. A Highly Selective Mitochondria-Targeting Fluorescent K^+ Sensor. Angewandte Chemie International Edition. 2015 Oct 5;54(41):12053–7.

251. Ding Y, Li X, Guo Y, Duan W, Ling J, Zha L, et al. Estimation of postmortem interval by vitreous potassium evaluation with a novel fluorescence aptasensor. Scientific Reports. 2017 Dec [cited 2019 Feb 26];7(1). Available from: http://www.nature.com/articles/s41598-017-02027-1

252. Shen Y, Wu S-Y, Rancic V, Aggarwal A, Qian Y, Miyashita S-I, et al. Genetically encoded fluorescent indicators for imaging intracellular potassium ion concentration. Communications Biology. 2019 Dec [cited 2019 Feb 26];2(1). Available from: http://www.nature.com/articles/s42003-018-0269-2

253. Riches AC, Sharp JG, Thomas DB, Smith SV. Blood volume determination in the mouse. J Physiol (Lond). 1973 Jan;228(2):279–84.

254. Boyd V, Cholewa OM, Papas KK. Limitations in the Use of Fluorescein Diacetate/Propidium Iodide (FDA/PI) and Cell Permeable Nucleic Acid Stains for Viability Measurements of Isolated Islets of Langerhans. Curr Trends Biotechnol Pharm. 2008 Mar;2(2):66–84.

7 Appendix

Appendix Table 1: Sensitivity and specificity parameters of GEPII 1.0 variants *in vitro (i.v.)* and *in situ (i.s.).* Reproduced from Bischof et al., 2017 with permission of publisher Nature Communications (217).

GEPII variant	Limit of detection $[K^+]$ (mM) *i.v.*	EC_{50} $[K^+]$ (mM) *i.v./ i.s.*	Hill Slope (K^+) *i.v./ i.s.*	EC_{50} $[Na^+]$ (mM) *i.v.*	EC_{50} $[Rb^+]$ (mM) *i.v.*	EC_{50} $[Cs^+]$ (mM) *i.v.*	EC_{50} $[NH_4^+]$ (mM) *i.v.*	EC_{50} $[Ca^{2+}]$ (mM) *i.v.*
GEPII 1.0	≤ 0.01	0.42/ 0.82	0.83/1.15	-	1.38	5.06	1.94	-
lc-LysM GEPII 1.0	≤ 1.0	30.47/ 60.95	1.17/1.22	-	42.58	-	-	-
lc-BON GEPII 1.0	-	-	-	-	-	-	-	-

Appendix Table 2 Sensitivity parameters of R-GEPIIs in situ (i.s.)

GEPII variant	Limit of detection $[K^+]$ (mM) *i.s.*	EC_{50} $[K^+]$ (mM) *i.s.*	Hill Slope (K^+) *i.s.*
R-GEPII 1.0	≤ 0.1	3.25	1.25
lc-LysM R-GEPII 1.0	≤ 3.0	75.12	0.8027

Appendix Table 3: Sensitivity parameters of GEPII 2.7, GEPII 2.10 and GEPII 2.15 *in vitro (i.v.).* Reproduced from Bischof et al., 2017 with permission of publisher Nature Communications (217).

GEPII variant	Linker length	Linker Amino Acid sequence	Limit of detection $[K^+]$ (mM) *i.v.*	EC_{50} $[K^+]$ (mM) *i.v.*	Hill Slope (K^+) *i.v.*
GEPII 2.7	7	GGGGSGG	≤ 0.1	3.24	1.25
GEPII 2.10	10	GGGGSGGGGS	≤ 0.1	4.39	1.27
GEPII 2.15	15	GGGGSGGGGSGGGGS	≤ 0.1	8.59	1.16